



University of
Stavanger

FACULTY OF SCIENCE AND TECHNOLOGY

MASTER'S THESIS

Study programme/specialisation:
Marine and Offshore Technology

Spring/ Autumn semester, 2020

Open / Confidential

Author: Nikita Nekrasov

Programme coordinator: Muk Chen Ong

Supervisor(s): Ove Tobias Gudmestad (UiS),
Anatoly Borisovich Zolotukhin (Gubkin University)

Title of master's thesis:
IMPROVING THE OPERATING METHODS OF THE PILTUN-ASTOKHSKOYE OIL
AND GAS CONDENSATE FIELD, TAKING INTO ACCOUNT THE
MANUFACTURABILITY OF THE EQUIPMENT AND ENVIRONMENTAL SAFETY
REQUIREMENTS.

Credits: 30 ECTS

Keywords: Sakhalin offshore, offshore
development, flowmeter, ESP, ice loads, Sea
of Okhotsk, the Piltun-Astokhskoye field.

Number of pages: ...108.....
+ supplemental material/other:

Stavanger, 10.06.2020
date/year

Abstract

This thesis is devoted to the oil and gas condensate field in the north of Sakhalin Island - Piltun-Astokhskoye. The development and operation in the Arctic is a very time-consuming and financially expensive process. In order to optimize production, it is necessary to upgrade equipment, always assess the precautions for workers, and regularly study the formation and its properties.

The main objective of this thesis is to improve the operating methods of the Piltun-Astokhskoye field with the modernization of the equipment, considering modern innovative solutions. Moreover, find a way to implement a program for import substitution of equipment.

Both downhole and surface equipment can be improved. In order to save money and develop domestic technologies, the concept of a differential pressure flow meter was proposed, and evidence of its superiority was presented. To implement the import substitution program (more use of Russian goods and services), within the framework of this thesis, it is proposed to replace the ESP with a domestic one, which is more economical and cheaper to use. As for the platform, the Russian methodology for calculating the horizontal ice load on the platform support was proposed and the geometry of the support was proposed to reduce the load.

The main concern during hydrocarbon production in the Arctic is the preservation of the ecological integrity of the region. Therefore, a risk analysis model was proposed, as well as measures and rules aimed at reducing these risks.

Content

ABSTRACT	2
ACKNOWLEDGEMENTS	10
INTRODUCTION.....	11
CHAPTER 1. CLIMATIC CONDITIONS OF THE SEA OF OKHOTSK OFF THE COAST OF SAKHALIN ISLAND	12
1.1. Wind conditions	12
1.2. Air temperature and water temperature	14
1.3. Seismic situation in the Sea of Okhotsk.....	15
CHAPTER 2. ICE CONDITIONS IN THE SEA OF OKHOTSK, ICE PROPERTIES AND METHODS OF ITS DESTRUCTION.....	17
2.1. General information	17
2.1. Ice drift	18
2.2. Ice properties	19
2.3. Methods of ice destruction and ice abrasion.....	21
CHAPTER 3. FLOW METERS AND ESP THEORY	23
3.1. Main types of flow meters.....	24
3.1.1 Variable differential pressure meter.....	24
3.1.2 Tachometric flow meters.....	26
3.1.3 Ultrasonic Flow Meters.....	28
3.2 ESP (Figure 3.6).....	29
CHAPTER 4. INFORMATION ABOUT THE PILTUN-ASTOKHSKOYE FIELD, ITS ARRANGEMENT AND EQUIPMENT	33
4.1. General information	33
4.2.1 Reservoir XXIs.....	37
4.2.2 Reservoir XXI'	38
4.2.3 Reservoirs I-IV	39
4.2.4 Reservoirs V-VI	39
4.2.5 Reservoirs VII-VIII.....	39

4.2.6 Reservoir IX	39
4.3. The development Project.....	40
4.4. Hardware Information	43
4.4.1 Platform "PA-A" (Molikpaq).....	43
4.4.2 Platform "PA-B"	47
CHAPTER 5. ANALYSIS OF EQUIPMENT APPLICABILITY AND PROPOSED IMPROVEMENTS	49
5.1. Flow meter.....	49
5.1.1 Introduction to Computer Simulation	50
5.1.2 OpenFOAM.....	51
5.1.3 Discharge coefficient.....	52
5.1.4 Basic laws applicable to the diaphragm	53
5.1.5 Computer simulation of fluid outflow through a sharp-edged diaphragm	54
5.1.6 Computer simulation of fluid flow through a diaphragm with beveled edges ..	57
5.1.7 Processing the received values. Differential pressure and coefficients of flow, distribution of pressures and speeds.....	60
5.2. ESP	64
5.2.1 General information	64
5.2.2 Manual selection of ESP	67
5.2.3 Technical comparison of used and proposed pumps	75
5.3 Calculation of ice load on the "platform substructures ("PA-B"), analysis of existing methods.....	75
5.3.2 Calculation of horizontal ice load according to SP 38.13330.2012.....	80
CHAPTER 6. FEASIBILITY STUDY AND ENVIRONMENTAL SAFETY MEASURES IN THE PILTUN AREA	83
6.1. Feasibility study on the choice of flow meter and ESP replacement.....	83
6.2. Environmental precautions in the Piltun area	85

CONCLUSION	89
REFERENCES	90
APPENDIX 1	93

List of abbreviations

CFD – Computational fluid dynamics

ESP – Electrical submersible pump

LNG – Liquid natural gas

OOP – Object-Oriented Programming

PA – Piltun-Astokhskoye field

RPM – Reservoir pressure maintenance system

SEM – Submersible electric motor

TOE – Tonne of oil equivalent

List of figures

Figure 1.1 Wind speed vectors (m/s) at an altitude of 10 meters 5.04.20 [3]	13
Figure 1.2 Wind speed vectors (m/s) at an altitude of 10 meters 10.04.20 [3]	13
Figure 1.3 The average wind speed depending on the month and weather station [4]	14
Figure 1.4 Water temperature 04/22/2020 [3]	14
Figure 1.5 The distribution map of depth and strength of earthquakes [6]	16
Figure 2.1 Current state of ice cover in the Sea of Okhotsk (0 - no ice, 10 - continuous ice) [3]	17
Figure 2.2 Ice drift pattern in the Sea of Okhotsk with light and moderate winds [8], where green is cloudy, and red is cloudy and low-pressure zone	19
Figure 2.3 Simulated ice salinity [11]	20
Figure 2.4 Ice breakdown for different types of surfaces [12]	21
Figure 2.5 Damage to the metal cladding on the supports "PA-B" [13]	22
Figure 3.1 Converters of flow meters of variable differential pressure	24
Figure 3.2 Centrifugal Flow Meters	25
Figure 3.3 Pressure Transmitters	26
Figure 3.4 Pressure Transmitter Converters	26
Figure 3.5 a) - volumetric meter with a turbine located axially to the flow; b) - tangentially to the flow	27
Figure 3.6 Schematic diagram of the ESP [29]	30
Figure 4.1 Actual and projected hydrocarbon production at the Piltun-Astokhskoye field [22]	35
Figure 4.2 Well trajectories characteristic of the Piltun site [20]	40
Figure 4.3 Presentation of the interphase contacts position of the Piltun site before the start of production drilling	41
Figure 4.4 Equipment of the Molikpaq platform [23]	44
Figure 4.5 Model of the Molikpaq platform before modernization [24]	45
Figure 4.6 Photo of the Molikpaq platform after modernization [24]	46
Figure 4.7 Ice load measurement instrumentation on the Molikpaq [25]	47
Figure 4.8 Photo of the Piltun-Astokhskaya-B platform [23]	47
Figure 5.1 Drawing for sharp-edged orifice	50
Figure 5.2 Orifice with back bevelled edges	53
Figure 5.3 Mesh for the case of sharp-edged orifice simulations	55
Figure 5.4 The dependence between C_d and different number of cells in the meshes	56
Figure 5.5 Numerical and experimental data in comparison with own results	57
Figure 5.6 Drawing of the orifice with bevelled edges	58
Figure 5.7 Mesh of the orifice with bevelled edges	58
Figure 5.8 Internal body of the bevelled orifice mesh	59
Figure 5.9 The dependence between C_d and different number of cells in the meshes	59

Figure 5.10 Present study of C_d in bevelled orifice type	61
Figure 5.11 Experimental data in comparison with own results	62
Figure 5.12 Pressure distribution through orifice with $t^*=1/4D$ (Pressure [m ² /s ²])	62
Figure 5.13 Velocity distribution through orifice with $t^*=1/4D$ and $Re=36(U$ [m/s])	62
Figure 5.14 Velocity distribution through orifice with $t^*=1/4D$ and $Re=100$ (U [m/s])	63
Figure 5.15 Statistics of the first failures of the company "RUSVETPETRO" [30]	67
Figure 5.16 Characteristics of the ESP-600-1350 [32]	72
Figure 5.17 The inclined barrier that destroys the ice mass [12]	76
Figure 5.18 The substructure with an angle of inclination of 30° from the horizontal	77
Figure 5.19 The substructure with an angle of inclination from the horizontal of 45°	78
Figure 5.20 The substructure with an angle of inclination from the horizontal of 60°	78
Figure 5.21 Scheme of application of loads from the ice mass to the substructure with a conical surface [34]	81
Figure 6.1 Bow-tie diagram for environmental protection	88

List of tables

Table 1.1. Temperature and rainfall in Nogliki [5]	15
Table 5.1 Performance characteristics of the ultrasonic flowmeter "300-082-FT-003"	49
Table 5.2 Convergence study for meshes of the sharp-edged orifice	56
Table 5.3 Convergence study for meshes of the sharp-edged orifice	60
Table 5.4 Different characteristics of the orifice with back bevelled edges	60
Table 5.5 Different characteristics of the sharp-edged orifice	60
Table 5.6 Initial data for manual selection of ESP [31]	68
Table 5.7 Submersible Pump Analysis	75
Table 5.8 Initial and calculated values for three conical structures	79
Table 5.9 Initial and calculated values for three conical structures	80
Table 6.1 Analysis of the economic feasibility of replacing the used flow meter	83
Table 6.2 Analysis of the economic feasibility of replacing the used ESP	83
Table 6.3 Competitiveness map	84

ACKNOWLEDGEMENTS

I would like to express my gratitude to my family for raising me and giving me the opportunity to study at one of the most prestigious universities in the country.

I would also like to thank the founders of the program – Professor Anatoly B. Zolotukhin and Professor Ove Tobias Gudmestad; thanks to them I am completing a joint international program with the University of Stavanger. I visited Norway, and I tried myself as a scientist.

Thanks to all the supervisors who helped me, supported me on the path to becoming an engineer. I am also grateful to all the teachers who taught me, especially at the University of Stavanger.

Introduction

Currently, the development of offshore fields is actively gaining momentum. That is because onshore oil and gas reserves are becoming less and less. In addition to the above, a direct consequence of scientific and technological progress is to increase efficiency and reduce the cost of production.

Three times more oil and gas are concentrated in the subsoil of the shelf than onshore. However, the development of offshore fields requires special skills, abilities of the company's employees, as well as its capitalization, because development requires not a small investment.

At the time of development of the Piltun-Astokhskoye field, Sakhalin Energy Investment Ltd. met all state criteria for obtaining a development license. Most of the technical and technological solutions adopted by the company were the most relevant and corresponded to a high level as part of the technical progress at the beginning of 2000, however, over the past decade a large number of innovative solutions have been developed that can improve the development of the Piltun site.

Chapter 1. Climatic conditions of the Sea of Okhotsk off the coast of Sakhalin Island

1.1. Wind conditions

The Sea of Okhotsk is a rather severe region with respect to climate, occupying one of the first places in the world in the number of days with stormy winds that arise due to cyclones passing over the water column. In the winter season, strong winds are a constant occurrence. From late October to early March, strong winds have a very high intensity due to the monsoon flow, which is due to the interaction of the Aleutian depression and the Asian anticyclone.

In summer, the onset of monsoon flows occurs due to the interaction of the Asian summer depression and anticyclone in the Sea of Okhotsk. The direction of the wind off the coast of Sakhalin is most often from north to south, and the more south, the higher the average wind speeds. For example, towards the south, the average wind speed increases from 8.3 m/s to 10-15 m/s.

April is the month of the transition from the winter monsoon to the summer occurs; during this period, instability of the winds is observed. In spring, the number of storm winds is 15-20%. The probability of the appearance of wind with a speed > 20 m / s is almost zero [2].

In Figures 1.1 and 1.2 we show how the direction and speed of the winds change in April. Changes in wind speed and direction are quite significant.

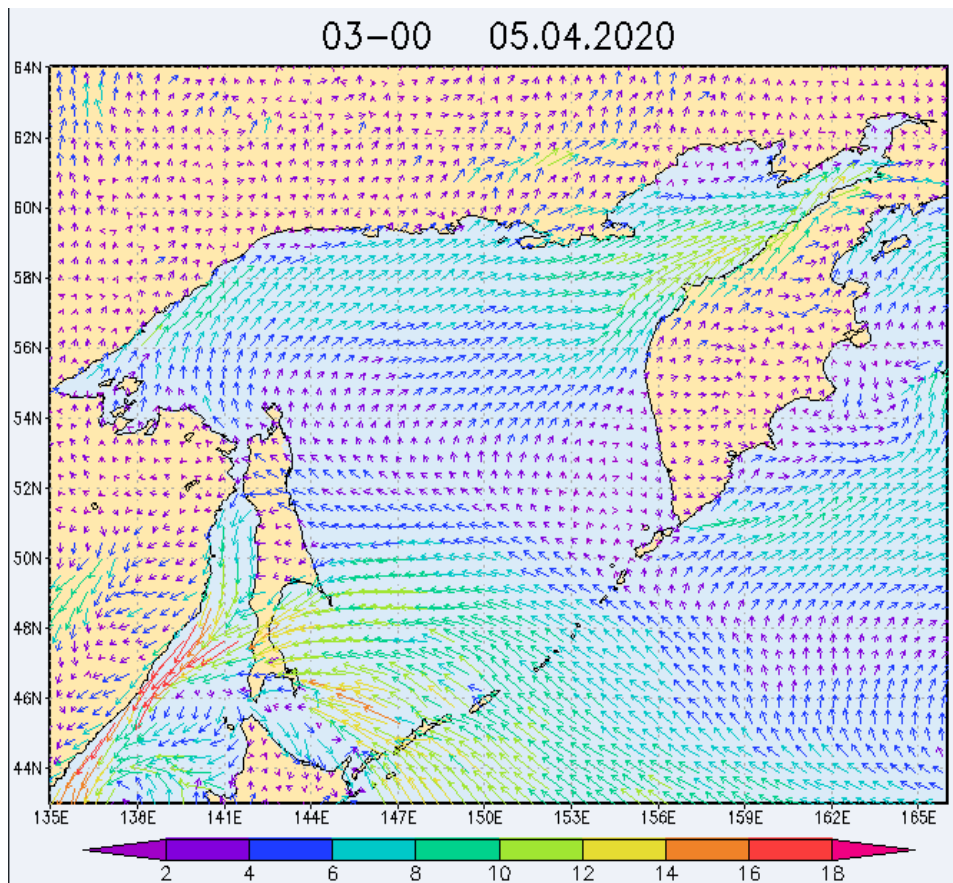


Figure 1.1 Wind speed vectors (m/s) at an altitude of 10 meters 5.04.20 [3]

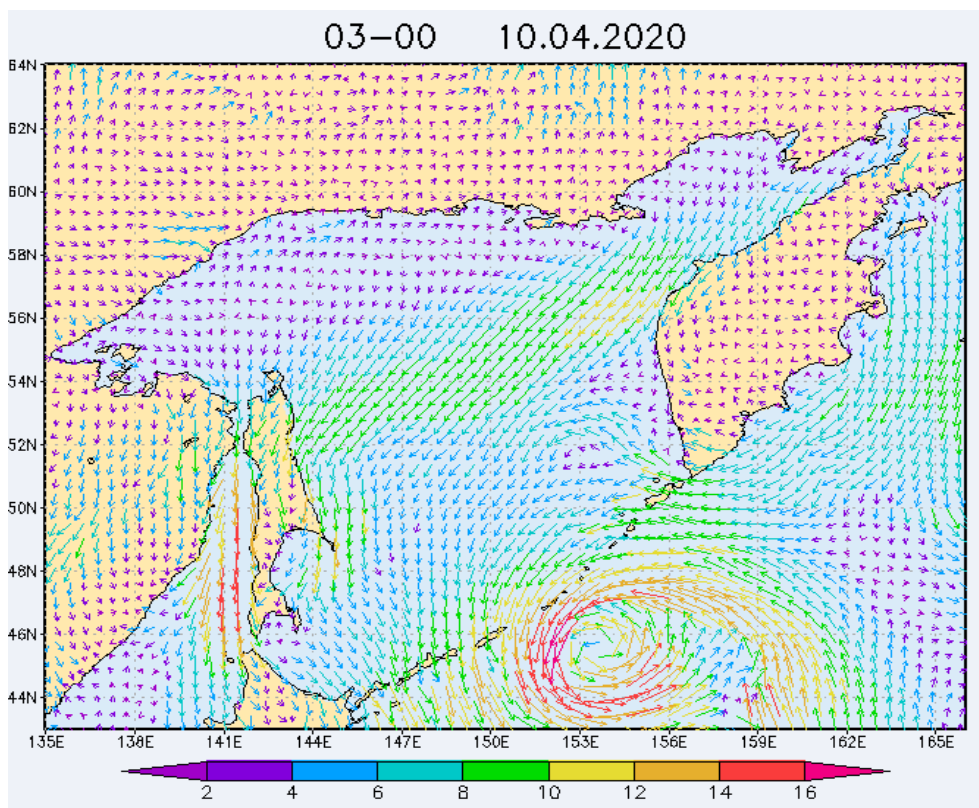


Figure 1.2 Wind speed vectors (m/s) at an altitude of 10 meters 10.04.20 [3]

The average wind speed at sea is almost two times higher in winter than the average wind speed in summer, as shown in Figure 1.3.

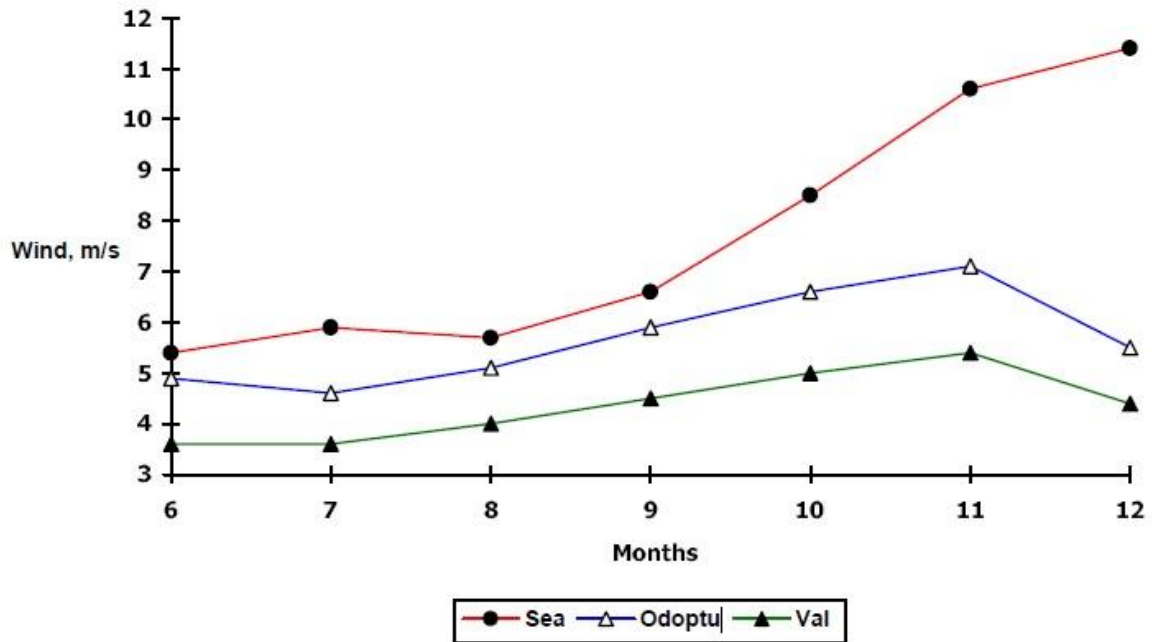


Figure 1.3 The average wind speed depending on the month and weather station [4]

1.2. Air temperature and water temperature

For more than six months, half of the sea surface is covered with ice. The surface water temperature during the winter season is around 0 ° C. The water temperature reaches 11-15 ° C off the northern coast of Sakhalin Island in summer [2].

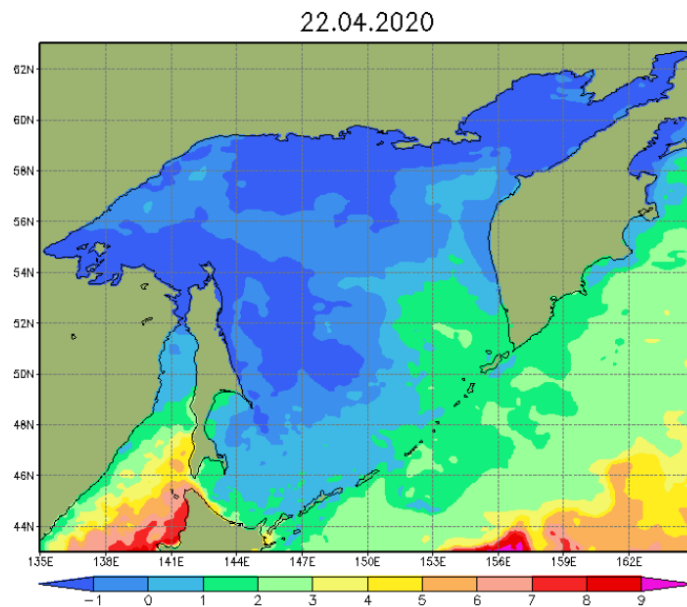


Figure 1.4 Water temperature 04/22/2020 [3]

Based on Figure 1.4, at the moment, the water temperature around the Piltun-Astokhskoye field is -1 ° C.

The PA-A platform is located near the city of Nogliki, so it was decided to consider the average temperature in this city over the past twenty years. In the table. 1.1. the temperatures and precipitation rates in Nogliki from the beginning of 2000, depending on the month, are presented.

Table 1.1. Temperature and rainfall in Nogliki [5]

Climate													
Number of months	1	2	3	4	5	6	7	8	9	10	11	12	Year
The absolute maximum °C	2,2	3,5	11,9	18,2	29,9	32,8	33	33,9	28,4	22,2	11,4	89	33,9
The average maximum °C	-12	-10,9	-4,5	1,8	8,1	15,6	17,8	19,9	16,8	8,1	-2,6	-10,7	3,3
The average temperature °C	-16,4	-16,1	-9,1	-1,9	3,7	10,1	13	14,9	11,5	3,8	-6,4	-14,9	-0,6
The average minimum °C	-21,3	-21,8	-14,9	-6,1	-0,2	5	8,9	10,7	6,6	-0,5	-10,9	-19,9	-5,4
The absolute minimum °C	-40	-42,2	-37,8	-26,1	-11	-10	0	-1	-4	-20	-33,9	-41,1	-42,2
The precipitation rates, mm	38	23	28	38	69	81	66	109	74	58	46	48	678

As can be seen from table. 1.1., the absolute and average minimums are recorded most often in February. The most significant rainfall occurs in the spring and summer seasons.

1.3. Seismic situation in the Sea of Okhotsk

Seismic activity in the Sea of Okhotsk is quite high. That is due to the contact of three lithospheric plates. On the borders of the Eurasian, Pacific and North American

earthquakes most often occur. Over the past 60 years, more than 30,000 earthquakes of various magnitudes have been recorded [6]. Along the eastern coast of Sakhalin, the Sea of Okhotsk extends, limited by deep faults. In this part of the Sea of Okhotsk, earthquakes occur mainly in the earth's crust. The most seismically active site is the ridge of the Kuril Islands. As follows from Figure 1.5, the average magnitude of earthquakes at the Piltun-Astokhskoye field is 4 Mb, while along the tectonic fault 5 Mb. The depths of the earthquake foci vary from 1 to 700 kilometres. In the area of the city of Nogliki, the average focal depth rarely reaches 100 kilometres, while in the south of the Sea of Okhotsk the average depth is 500 km.

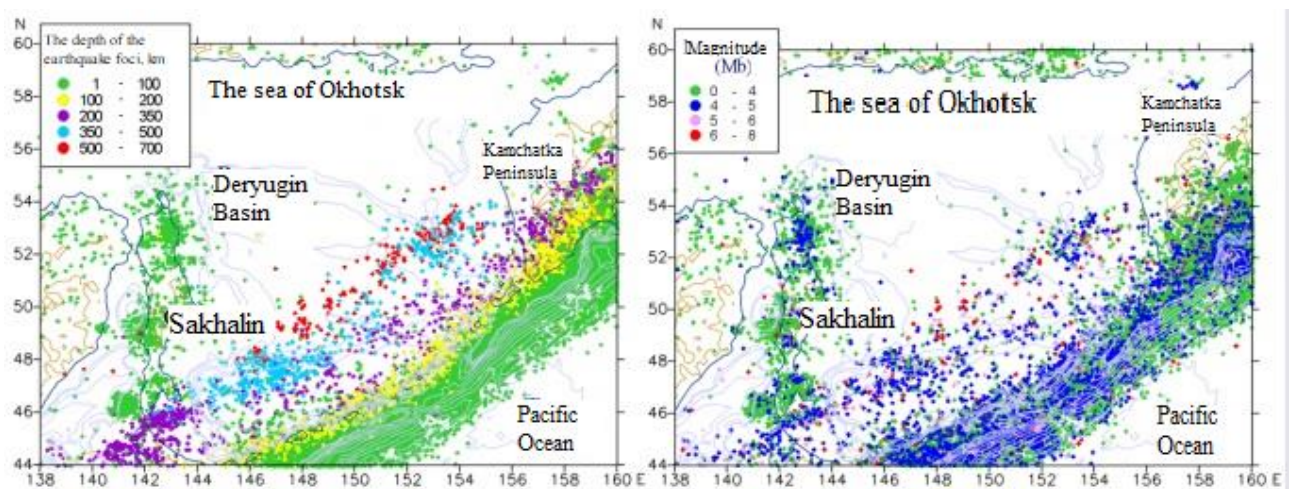


Figure 1.5 The distribution map of depth and strength of earthquakes [6]

About ten tangible earthquakes occur directly on Sakhalin annually, and only once every five years does a powerful earthquake occur [7], which can even destroy an entire city. One such example of an earthquake occurred in the city of Neftegorsk. This city was completely destroyed in May 1995. The depth of the outbreak was 9 kilometers, and the magnitude was 7.6 on the Richter scale. The epicenter of this earthquake was not far from the Deryugin basin, near which the Piltun-Astokhskoye field is located. Based on the previous, it is necessary to take special care of the seismic situation in this region.

Chapter 2. Ice conditions in the Sea of Okhotsk, ice properties and methods of its destruction

2.1. General information

Long winters with severe frosts are a catalyst for icing of the sea surface as a result of its cooling. This process is accompanied by abundant ice formation along the coast of Sakhalin Island. In the Sea of Okhotsk, there is both stationery and drifting. The average duration of the ice period is almost 210 days, and the record period is 290 days. Ice formation usually begins in late October. The most significant ice drift is usually observed in February and March. The maximum ice thickness during the ice season is 1.9 meters. The maximum ice thickness recorded over the past hundred years is 2.3 meters. Ice loads are the second most essential loads on the Sakhalin shelf. The first is the load arising as a result of seismic activity, in particular, in the zone where we find the oil and gas fields [4]. At the moment, almost all the ice has melted, however, as can be seen in Figure 2.1, there is still a lot of ice in the Sea of Okhotsk.

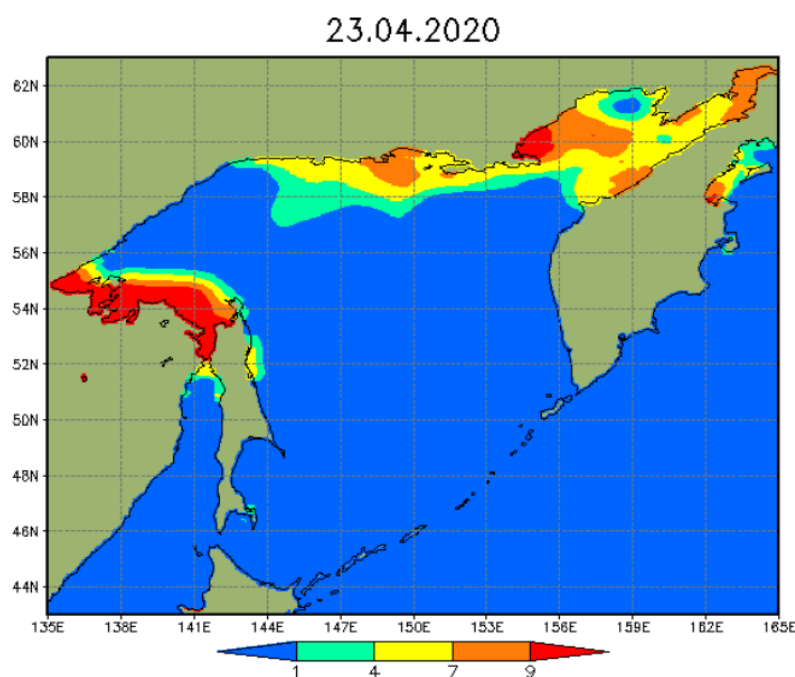


Figure 2.1 Current state of ice cover in the Sea of Okhotsk (0 - no ice, 10 - continuous ice) [3]

That is due to the harsh climate in the north of Sakhalin, at the same time, according to the Russian Hydrometeorological Center, there was almost no ice directly at the field according to data as of April 23, 2020.

2.1. Ice drift

Floating ice are in motion, moving long distances under the influence of wind and currents. The total transfer of ice under the influence of these factors is called ice drift. The study of ice drift was carried out by many researchers; however, a Norwegian polar explorer F. Nansen made a serious scientific attempt to determine the causes of ice drift and to establish the connection between ice movement and wind. Analyzing the drift of “Fram” (1893-1896) in the Arctic Ocean, he established the following empirical relationships:

1. the direction of ice movement in the open sea deviates from the wind direction to the right by 28°.
2. the ice drift velocity is 1/50 of the wind speed, i.e., the wind coefficient (the ratio of ice drift velocity to wind speed) is 0.02.

The ice drift velocity is directly proportional to the gradient of atmospheric pressure or inversely proportional to the distance between isobars:

$$v = \frac{0.01}{2\bar{\omega}\rho\sin(\varphi)} * \frac{\partial p}{\partial n} \quad 2.1$$

Where v – ice drift velocity, $\bar{\omega}$ - earth's angular velocity, ρ – air density, $\frac{\partial p}{\partial n}$ horizontal gradient of atmospheric pressure.

In figure 2.2 is an intricate image obtained from three visible and one thermal IR channels of a MODIS spectroradiometer; data were taken from the Aqua satellite in March 2012. The illustration in natural colors, which can distinguish ice cover and cloudiness, is combined with an infrared channel in pseudo-colors, which reflects the temperature field on the surface of the water, not covered by ice. In the form of arrows are the vectors of the general ice drift in the period from March 25–29 [8]. This is a

general drift pattern in light to moderate winds. The main conclusion is that ice moves from the north of the island to the south, respectively, the PA-A and PA-B platforms must be strengthened from the north.

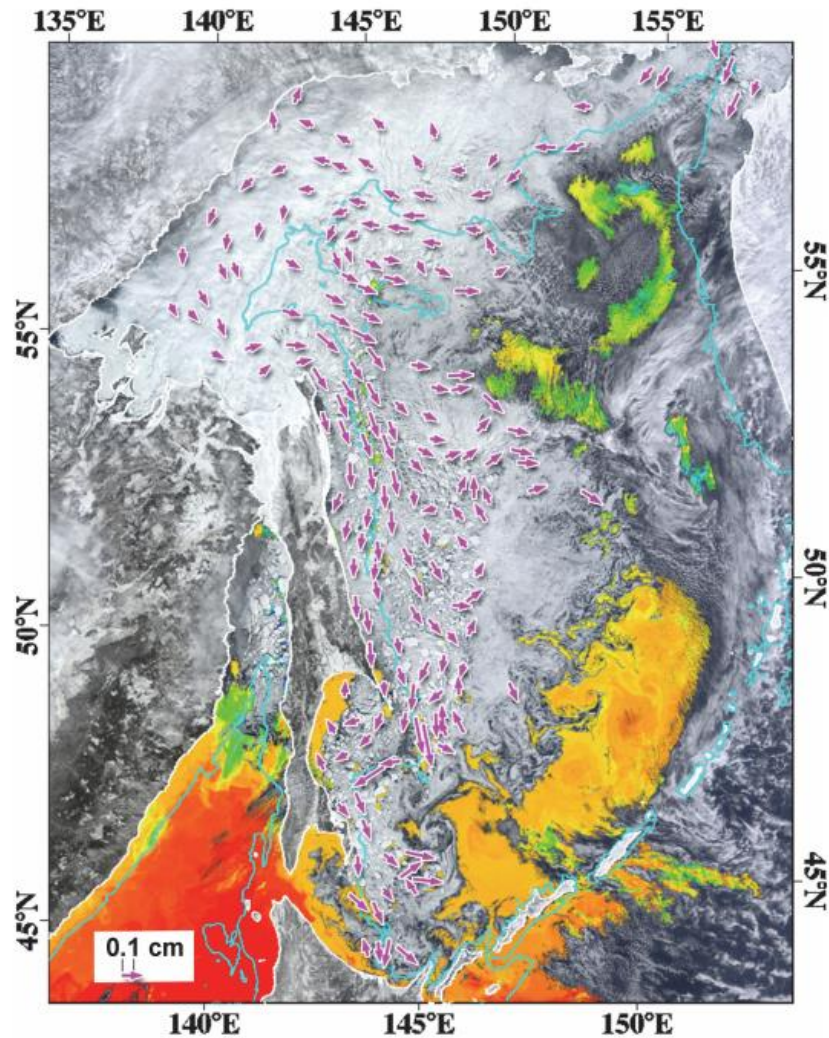


Figure 2.2 Ice drift pattern in the Sea of Okhotsk with light and moderate winds [8], where green is cloudy, and red is cloudy and low-pressure zone

2.2. Ice properties

Ice is a mineral with the chemical formula H_2O , it is water in a crystalline state. The chemical composition of ice is H - 11.2%, O - 88.8%. Sometimes it contains gaseous and solid solids. In nature, ice is represented mainly by one of several crystalline modifications, H_2O stable in the temperature range from 0 to 80 ° C, with a melting point of 0 ° C when there is no salt added. Ten crystalline modifications of ice and amorphous ice are known. Amorphous ice (non-crystalline or "vitreous" ice) is

an amorphous solid form of water. Common ice is a crystalline material wherein the molecules are regularly arranged in a hexagonal lattice, whereas amorphous ice has a lack of long-range order in its molecular arrangement. The most studied is the ice of the 1st modification - the only modification found in nature. Ice is found in nature in the form of ice itself (mainland, floating, underground, etc.), as well as in the form of snow, hoarfrost, etc.

There are always cavities with brine and cavities filled with air or gases in ice [9]. The ratio of the volume of bubbles with gas or air to the total volume of the ice sample, expressed as a percentage, is called the porosity of the ice. The porosity of sea ice can vary from 5 to 13%. The porosity of ice affects its density (the greater the porosity, the lower the density of ice). The densest are the middle parts of ice ridges and hummocks, repeatedly subjected to compression.

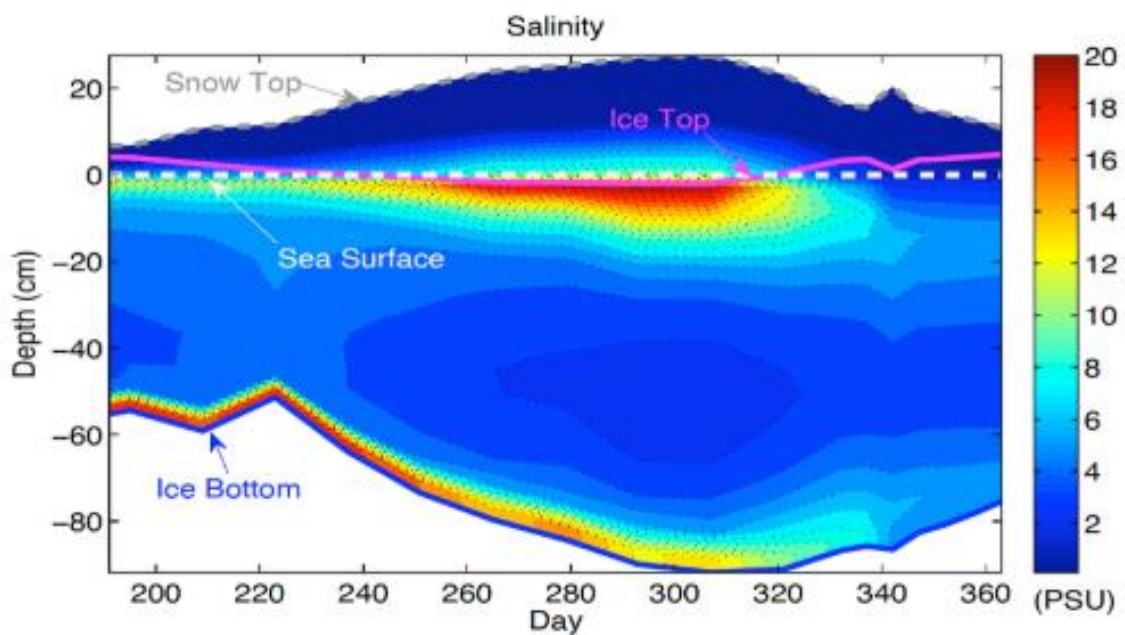


Figure 2.3 Simulated ice salinity [11]

Derugin (1974) [10] wrote that the second most important property of sea ice is the salinity. The salinity of the ice is several times less than the salinity of the water that formed the ice. With large porosity of the ice, its density is significantly reduced. Porosity has a greater effect on density compared to salinity. As seen from Figure 2.3, the most saline area is located on the top of ice. The ice salinity in this place reaches

20 PSU (Practical Salinity Units, where 1 PSU = 1 g/kg), while in the center of the ice, the salinity is almost zero.

2.3. Methods of ice destruction and ice abrasion

According to ISO 19906: 2019 (E) [12], the effect of ice on a surface depends on its thickness, mass and mechanical properties, speed of drift, and temperature. There are several ways to break the ice, such as shear, crushing, bending, and creep. Depending on the properties of the structure that destroys ice, various types of ice destruction can occur. Figure 2.4 shows vertical and inclined surfaces. An inclined structure crushes ice due to bending moment. In the case of a vertical surface, the ice breaks due to crushing.

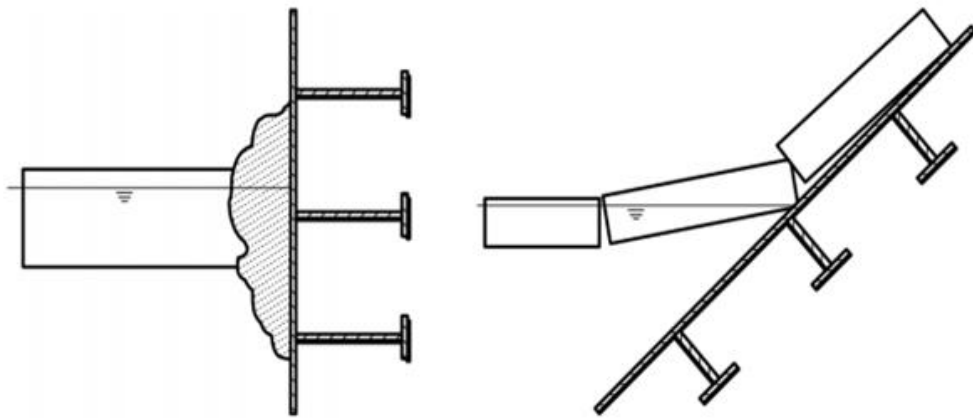


Figure 2.4 Ice breakdown for different types of surfaces [12]

Ice affecting the concrete or metal surface of the structure causes abrasion of the material. By abrasion is meant the removal of particles of the material of the structure from the contact surface during sliding and friction of ice. In this case, four types of abrasion are possible: abrasive, adhesive, fatigue, and corrosion [13]. Due to the high contact pressure, vertical and horizontal movements of ice, the surface in contact with ice is always "cleaned", which creates favorable conditions for the gradual destruction of the material.

The leading design solutions that take into account the abrasive effect of ice:

- in the case of a metal surface: tolerance for abrasion of the material (increase in metal thickness in the zone of contact with ice); application of high-strength, abrasion-resistant coatings.
- in the case of concrete: the use of high-strength, wear-resistant concrete, as well as taking into account tolerances for abrasion and the application of an additional layer of concrete in the area of direct ice exposure.

Two different types of platforms are used at the Piltun-Astokhskoye field - PA-A and PA-B. "PA-A" (Molikpaq) is a gravity-caisson type platform with a metal caisson filled with sand. PA-B is a gravity-type platform with four concrete supports.

Another method of protecting concrete surfaces is the use of protective steel belts. However, steel ice protection belts cannot always withstand ice shocks in conditions of high dynamics of ice cover drift. Figure 2.5 shows examples of the destruction of steel protective belts on one of the platforms with a reinforced concrete base in the Sea of Okhotsk. The cause of the damage can be both external influence and insufficient thickness of the metal belt along with an improper system for attaching the housing to reinforced concrete support.



Figure 2.5 Damage to the metal cladding on the supports "PA-B" [13]

Chapter 3. Flow meters and ESP theory

The use of flowmeters is an integral part of the technological process in the modern industrial world. Demand for flow meters is increasing over the years due to close attention to saving energy and water resources. Flowmeters are used to control and optimize process conditions in the oil and gas industry. Automation of production and achieving maximum efficiency are impossible without these devices. A flow meter is required to record the flow of oil, water, gas and other substances transported through pipelines. Flow meters make it possible to record substance leaks from the pipe, which can significantly increase production efficiency. They exclude the loss of valuable raw materials. Besides, the use of flowmeters helps to control the flow rate of each well separately, as well as the flow rate of the injected fluid to maintain reservoir pressure. In other words, the presence of a flow meter in the field helps to optimize the entire process of production and transportation of hydrocarbons.

Currently, several requirements apply to flow meters:

- High accuracy
- Low dependence of measurement accuracy on fluid density
- High reliability
- Wide range of measurements

The wide variety and complexity of the requirements have led to the creation of a massive number of types of flow meters. There are three main groups for measuring flow [14]:

1. Devices that measure flow using hydrodynamic methods;
2. Accessories with the continuous mechanical movement of the body;
3. Devices based on various physical phenomena.

Of the measuring devices based on hydrodynamic methods, flow meters of variable differential pressure, vortex and level gauges are best known. Tachometric and power

flow meters belong to the second group. The most popular flow meters belonging to the third group are acoustic (ultrasonic).

3.1. Main types of flow meters

3.1.1 Variable differential pressure meter

The measuring complex, the principle of which is based on the dependence of the differential pressure flow rate created by the flow transducer installed in the pipeline, is called a variable differential pressure flow meter.

Such flowmeters have varieties, depending on the type of flow transducer [15]:

1. With constricting devices;
2. With hydraulic resistance;
3. Centrifugal;
4. With pressure devices;
5. With pressure amplifiers;

1. Flowmeters with tapering devices are based on measuring the pressure drop resulting from the conversion of part of the potential energy into kinetic in the tapering device. The main varieties of tapering devices are presented in Figure 3.1; they are apertures. Subsequently, the diaphragm a) will be considered.

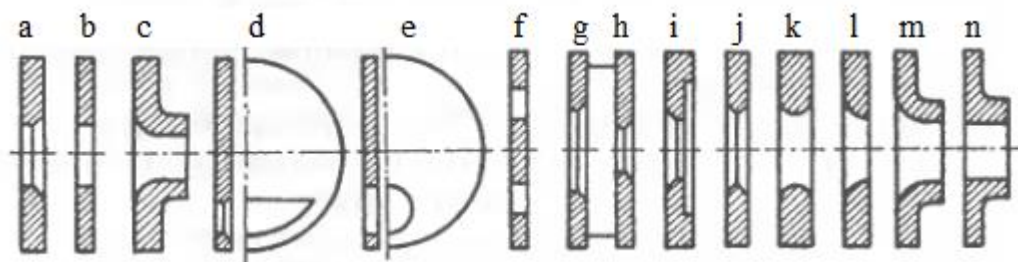


Figure 3.1 Converters of flow meters of variable differential pressure, where a) and b); standard nozzles, c); segmented diaphragm, d); eccentric diaphragm, e) and f); annular diaphragms, g) - n); tapering devices for small Reynolds numbers [15]

In this master's thesis, the main goal is to improve equipment on the platforms of the Piltun-Astokhskoye field. Therefore, a flowmeter with a diaphragm is considered, for which appropriate modelling will be carried out. The principle of operation of such a flow meter is based on the Bernoulli equation, which establishes a relationship between the pressure of a liquid and its speed. With the decreasing flow rate, pressure increases, and vice versa. The speed directly depends on the Reynolds number.

2. Flowmeters with hydraulic resistance are based on measuring the pressure drop created by this resistance. They seek to create a flow regime which is laminar so that the pressure drop is proportional to the flow rate. They are rarely used, mainly for measuring low flow rates. A capillary tube or a packet of such tubes can serve as a converter.

3. Centrifugal flow meters are based on recording the differential pressure created in the tubes due to centrifugal force. This can be achieved by using a bend or pipe section in the form of a loop as shown in Figure 3.2, where o) is the knee, and p) is the pipe loop [15].

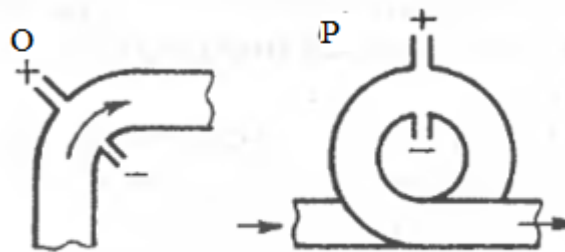


Figure 3.2 Centrifugal Flow Meters

4. Flow meters with pressure device. Such flowmeters record the pressure drop depending on the flow rate using a pressure device. A classic example is a pitot tube for determining pressure, and a tube for determination of static pressure as shown in Figure 3.3, where Q) are separate sampling tubes, and R) is the combined pitot tube [15].

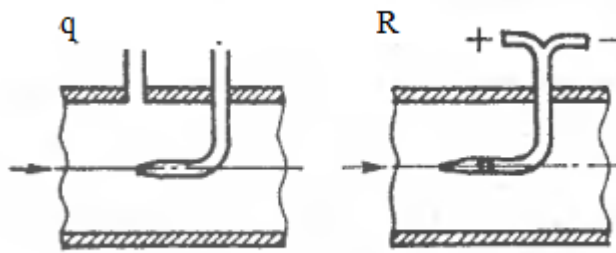


Figure 3.3 Pressure Transmitters

5. Combined flow meters with a pressure amplifier. In such flowmeters, both a constricting device and a pressure device are located. The pressure drop occurs due to a local transition of kinetic energy to potential, as well as a partial transition of potential to kinetic. Figure 3.4 shows a combination of a diaphragm and a pitot tube [15].

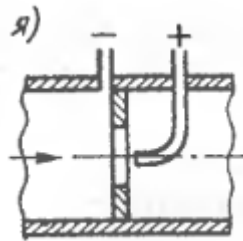


Figure 3.4 Pressure Transmitter Converters

This type of differential pressure meter also includes a venturi. It is used when the pressure drops when using the Pitot tube is minimal.

Differential pressure flow meters have several advantages. Such flowmeters can be used for any single-phase liquid in a wide range of pressure and temperature with relative ease and ease of manufacture. Relatively simple calibration and good accuracy with an error of 1-2 percent is obtained [14]. One of the main disadvantages is the difficulty of using such flowmeters with low flow rates and the presence of flow pulsations, as well as a stream with a large amount of impurities.

3.1.2 Tachometric flow meters

The most popular tachometer flowmeter is a volumetric meter with a turbine, which can be located axially to the flow or tangentially, as shown in Figure 3.5 [16].

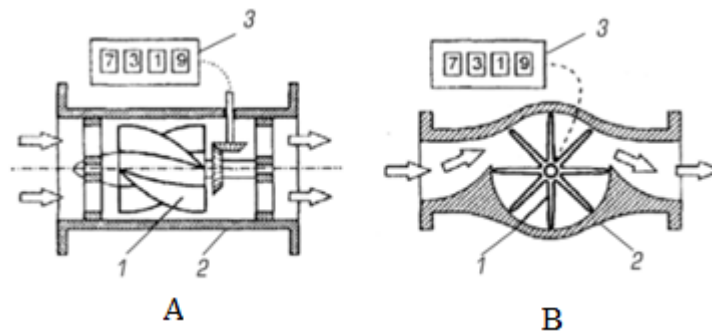


Figure 3.5 a) - volumetric meter with a turbine located axially to the flow; b) - tangentially to the flow, where 1 - turbine, 2 - casing, 3 – counter

Tachometric flowmeters are used to measure liquid or gas. The principle of operation of such flow meters is based on the dependence of the speed of the converter element installed in the pipeline or a special chamber, on the flow of gas or liquid.

The principle of operation of turbine mechanical flow meters-counters is based on measuring the speed of rotation by a flow (gas or liquid) of a measuring turbine. For the smooth operation of the counters, the absence of turbulence in the flow entering the turbine is necessary. In order to avoid turbulence at the inlet to the guiding apparatus and the turbine blades, a jet straightener is usually used, which is a metal plate mounted at the inlet to the guiding apparatus.

The advantages of tachometric flow meters include high accuracy in the absence of turbulence in the flow, the possibility of accurate measurements at low flow rates, as well as their low cost.

The disadvantages of such flowmeters directly depend on their principle of operation. For example, if we are talking about a turbine, then the turbine itself and the bearing wear out. This leads to a decrease in measurement accuracy. Such flowmeters are very sensitive to mechanical impurities and the presence of gas bubbles in the stream.

Also, to this group of flowmeters can be attributed power flow meters - Coriolis. In them, under the influence of force, Coriolis acceleration arises, depending on the flow rate. These flowmeters are relatively compact for use on the platform, but they will not be taken into account in this work because of their high cost and the complexity of the

measurements. Besides, these flowmeters separate the flow; subsequently, when the flow is mixed, new turbulences and phase transitions occur, as well as additional hydraulic losses.

3.1.3 Ultrasonic Flow Meters

Ultrasonic flow meters use sound wave vibrations to determine the speed of a fluid flowing in a pipe. In the absence of flow, the frequencies of the ultrasonic wave transmitted to the tube and its reflections from the liquid are the same. In flow conditions, the frequency of reflected oscillations is different due to the Doppler effect. When the fluid moves faster, the frequency shift increases linearly. The transmitter processes the signals from the transmitted oscillations and their reflections to determine the flow rate.

Ultrasonic flow meters send and receive oscillations between transducers in both the upstream and downstream directions in the pipe. In the absence of flow, it takes the same time to move up and down between the sensors. Under flow conditions, the upward wave will move slower, and its movement will take longer than the (faster) downward wave. When the fluid moves more quickly, the difference between upstream and downstream times increases. The transmitter processes the upstream and downstream times to determine the flow rate [17].

This technology can be very accurate and is used to measure oil and gas consumption. It has a wide range of pressures and temperatures usage, and can be used with a clamp on the outside of the pipe without penetration, very reliable. Disadvantages may include high cost, sensitivity to process vibrations, problems with pipe diameter changes due to buildup, and that clamping devices have lower accuracy.

There are no hydrodynamic losses in ultrasonic flow meters, so they can even be used with sanitary, aggressive and abrasive fluids. Some ultrasonic flow meters are used as overhead transducers that can be installed outside the pipe and do not have wetted parts. Temporary flow measurements can be performed using portable ultrasonic flow meters with clamp sensors. In addition, overhead transmitters can be used to measure flow

without taking into account structural materials, corrosion and abrasion. No matter how attractive the use of overhead transmitters, additional ultrasonic interfaces are introduced that can affect the reliability and performance of these flow meters. In particular, if applied improperly, the attenuation of the ultrasonic signal can occur at the interfaces between the clamp sensors and the external walls of the pipe, as well as between the internal walls of the pipe and the liquid.

3.2 ESP (Figure 3.6)

ESP is an electric centrifugal pump unit designed for oil production. These facilities are applied in more than 70% of oil in Russia, which is why this type of mechanized oil production is the most popular.

ESP can work in an environment characterized by its aggressiveness to the mechanisms present in it. The pump installation consists of a submersible pump unit (electric motor with hydraulic protection + pump), cable line, tubing string, wellhead equipment and ground equipment (transformer and control station).

The borehole pump assembly is lowered onto the tubing string. Electricity is supplied to the submersible electric motor through a round cable that runs from the surface along with the tubing to the pump unit and then passes into a flat cable. This type of cable is used to reduce the total diameter of the borehole's electric pump unit, which provides free, lowering and lifting of the pump without damage.

The limitation of the diameters of the borehole electric pump units leads to the need to increase the length of the units with electric motors up to 350 kW. Diameters of aggregates are in the range of 69-241 mm, the lengths of the installations are more than 25 m.

The installation of an electric centrifugal pump is designed to select formation fluid:

1. With a maximum solids content of 0.01%;
2. With a maximum water cut of 99%;
3. With a maximum volumetric content of free gas at the pump intake of 25-30%;

4. With a maximum hydrogen sulfide content of 0.01 grams per 1 liter.

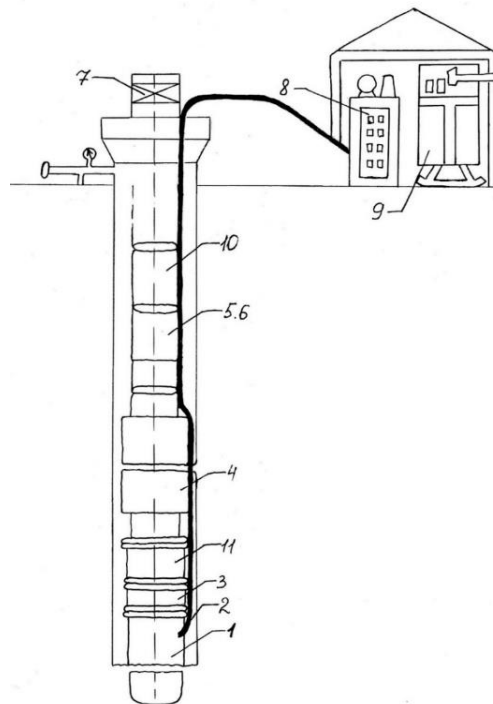


Figure 3.6 Schematic diagram of the ESP [29]

Figure 3.6 shows a diagram of a pumping unit, which contains several components and assemblies: 1 - engine; 2 - cable; 3 - hydro protection; 4 - ESP pump 5.6 - check and drain valves; 7 - wellhead equipment; 8 - autotransformer; 9 - control station; 10 - tubing; 11 - suction module.

The connection of the nodes of the pump unit is as follows: sections of the pump, hydraulic protection and electric motor - flange. The shafts of the electric motor, tread and pump are connected by splined couplings.

A threaded fishing head is provided at the top of the pump for connection to a tubing string. The design of the head allows fishing operations of the pump unit when it is turned away from the tubing or in case of the destruction of the sub in the threaded part of the fishing head. The pump unit with tubing and cable is suspended on the wellhead equipment, which provides sealing of the cable and tubing, as well as the removal of liquid and gas.

ESP can be classified by design:

1. Normal execution;
2. Wearproof execution;
3. Corrosion-resistant performance.

By size:

- Size 2A, an outer diameter of the pump casing pipe 69 mm;
- Size 3, an outer diameter of the pump casing 81 mm;
- Size 4, an outer diameter of the pump casing 86 mm;
- Size 5, an outer diameter of the pump casing 92 mm;
- Size 5A, an outer diameter of the pump casing 103 mm;
- Size 6, an outer diameter of the pump casing pipe 114 mm;
- Size 6A, an outer diameter of the pump casing pipe 123 mm;
- Size 6B, an outer diameter of the pump casing 130 mm;
- Size 7A, an outer diameter of the pump casing pipe 136 mm;
- Size 8, an outer diameter of the pump casing 172 mm;
- Size 9, an outer diameter of the pump casing pipe 185 mm.

There are also classifications of dimensions of foreign manufacturers:

- Type A 338th series, pump housing diameter (86 mm);
- Type D 400th series, pump housing diameter 4 "(102 mm);
- Type G 513 series, pump housing diameter 5¹/₈ "(130 mm);
- Type E 538th series, pump housing diameter 5¹/₃ "(137 mm);
- Type H 562 series, pump housing diameter 5⁵/₈ "(143 mm);
- Type J 675 series, pump housing diameter 6³/₄ "(171 mm);

- Type M 862 series, pump housing diameter 8⁵/₈ "(219 mm);
- Type N 950 series, pump housing diameter 9¹/₂ "(241 mm).

By the number of supports, we are distinguishing single-bearing and two-bearing impeller design.

Assembly: "batch", "compression" and with a floating impeller.

The corrosion-resistant centrifugal pump is designed to operate when the content of hydrogen sulfide in the pumped formation fluid is up to 0.5 g/l. The wear-resistant design allows pumping liquid with the content of mechanical impurities up to 0.5 g/l [29]. Each installation has its own marking, for example, ESP5A-500-800, in which the following designations are adopted: the number (or number and letter) after the ESP indicates the smallest permissible inner diameter of the casing into which it can be lowered. The number "4" corresponds to diameter 112 mm, the number "5" corresponds to 122 mm, "5A" - 130 mm, "6" - 144 mm and "6A" - 148 mm; the second number of the code indicates the nominal pump flow (in m³ / day) and the third is the approximate pressure in (m). Flow and head values are for water.

Chapter 4. Information about the Piltun-Astokhskoye field, its arrangement and equipment

4.1. General information

The development of the Piltun-Astokhskoye field began as part of the Sakhalin 2 project on June 22, 1994. An agreement was signed between the Sakhalin Oblast administration, the Russian government, and Sakhalin Energy ltd. This company was represented by a consortium of five companies: McDermott, Marathon, Mitsui, Mitsubishi and Shell [21].

Currently, the company's shareholders are:

- "Gazprom" - 50% plus one share;
- "Royal Dutch Shell" - 27.5% minus one share;
- "Mitsui & Co., Ltd" - 12.5%;
- "Mitsubishi Corp." - 10%.

In 1997, the first stage of development of the Piltun-Astokhsky site began. As part of this phase, the PA-A platform (Molikpaq) was modernized, delivered and installed. Production started in the summer of 1999. Operations were halted during the winter period due to difficulties with offloading. It was also necessary to equip the platform with equipment for waterflooding. Also, in the framework of this stage, studies of the productive formations were carried out, as well as data on operational characteristics were collected to optimize further stages of field development.

The next development stage included the commissioning of the Piltun-Astokhsky PA-B platform, as well as the inclusion of the Astokhsky section into year-round operation, the construction of the station for the preparation of products for transportation, the commissioning of gas and oil pipelines for transporting hydrocarbons to the south of the island, and the plant for liquefying natural gas (now referred to as LNG) and export terminals. Nowadays, the second phase of development is underway.

If we consider the stages in more detail, then the first stage can be divided into four projects:

- Project 1
- Project 1a
- Project 1b
- Project 1c

Project 1 included the development of a field in natural mode with subsequent re-injection of gas. During this project, 13 production and one gas injection wells were drilled. At that time, oil production was not year-round, but seasonal. The extracted oil was delivered to land by tankers, and the associated gas was pumped back into the reservoir.

Project 1a has been implemented since 2004. According to 2007, during this period of time, five wells were drilled, four water-injection (PA-116, -120, -122 and -126), one for production (PA-118), which since April 2004 has been used for the burial of drilling waste. Injection of seawater to maintain reservoir pressure was year-round, due to which reservoir pressure was restored to its initial value.

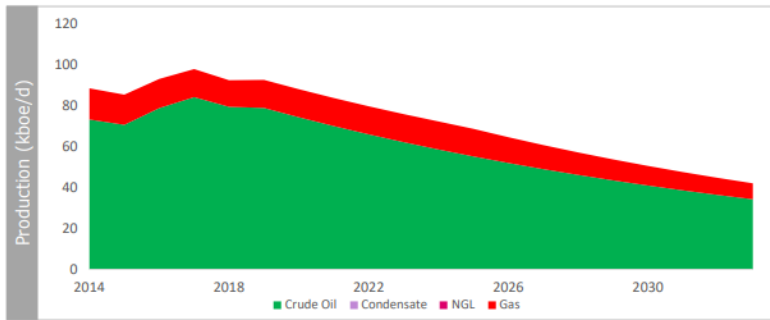
Project 1b was implemented in 2008 and related to the commissioning of the Trans-Sakhalin oil pipeline, as well as the transition of the PA-A platform (Molikpaq) to year-round oil extraction from the productive formations of the Piltun-Astokhskoye field.

Project 1c is being implemented to this day; the main goals of this project are to seal the grid of wells, switch to mechanized production and develop reserves of formations XXIII and XXV.

As shown in Figure. 4.1, oil is the main mineral produced in the framework of the Piltun-Astokhskoye field. The peak of production occurred in 2018 and amounted to 13720 TOE in one day. It should be noted that the percentage of associated gas with the development is practically unchanged.

Production

Piltun Astokhskiye (Sakhalin-2)



Key Production Metrics		
Production Start Year		1999
Estimated Last Production Year		2066
Share Produced by the end of 2018	%	44
Peak Production	kboe/d	98
Cumulative production by the end of 2018	Mmboe	446.808
Remaining Resources/Peak production ratio	Years	16.0

kboe/d	2014	2015	2016	2017	2018	2019	2020	2021	2022	2023	2024	2025	2026	2027	2028	2029	2030	2031	2032	2033
Crude Oil	73	71	79	84	79	79	74	70	66	62	59	55	52	49	46	43	41	39	36	34
Condensate	-	-	-	-	-	-	-	-	-	-	-	-	-	-	-	-	-	-	-	-
NGL	-	-	-	-	-	-	-	-	-	-	-	-	-	-	-	-	-	-	-	-
Gas	15	15	14	14	13	14	14	14	14	14	14	13	13	12	11	10	10	9	8	8
Total	88	85	93	98	92	93	88	84	80	76	72	69	65	61	57	54	51	48	45	42

Figure 4.1 Actual and projected hydrocarbon production at the Piltun-Astokhskiye field [22]

4.2. Geological structure and stratigraphy

The North Sakhalin sedimentary basin is composed of a thick sequence of Cenozoic deposits. The basement immersion depth in the lowered blocks is 5-12 km, on the framing and internal uplifts its surface is located at depths of 1.5-3 km. The foundation was laid by Triassic – Early Cretaceous volcanic – siliceous, and in some cases, Late Cretaceous volcanic deposits [18].

The horizons in the lower part of the stratigraphic section (Lower Nutov-Cretaceous deposits) can be distinguished on seismic material by analogy with other wells and fields, in particular, well 1 in Darginskaya Square. Below is a list of stratigraphic units of the section indicating the thickness and age of the deposits:

- Quaternary deposits (thickness - up to 30 m);
- Nutovskiy horizon (Upper Miocene-Pliocene, thickness - 2800 m);
- Okobykaysky horizon (Middle Miocene, thickness - 190 m);
- Darginsky horizon (Middle-Lower Miocene, thickness - 800 m);
- Uininsky horizon (Lower Miocene, thickness - 120 m);

- Daekhuryinsky horizon (Oligocene, thickness - 650 m);
- Machigarsky horizon (Oligocene, thickness - 50 m);
- Cretaceous deposits.

The Paleogene is represented by the Machigar and Daekhuri structural-stratigraphic complexes formed in the early rift stage of the development of sedimentary basins. The total thickness is 700 m. By faults, this complex is divided into several horsts and grabens. Paleocene-Eocene deposits are developed only in the south, in the Lunsky synclinal zone. Oligocene deposits on the northeastern shelf of Sakhalin are ubiquitous and are represented mainly by silty-clayey-siliceous rocks of relatively deepwater facies of the open sea. The Neogene section on the northeast shelf of Sakhalin begins with Early Middle Miocene sediments up to 3 km thick, represented here by the rocks of the Uininsky-Dagin complex, formed in the late rift stage of the basin development. The thickness of this complex at the Piltun-Astokh Square is 920 m [19].

The complex is characterized by intense disjunctive disturbance, which forms folded-block forms - horst-anticlines and graben-synclines. In the Early Miocene, at low sea level, the front of the Paleoamura delta advances into the southern part of the northeastern shelf of Sakhalin. The Uininsky-Dagin oil and gas complex is composed of clay and sand and clay-sand deposits of different facies with a general predominance of sand-silt rocks. Up the section, these sediments are replaced by the Okobykai – Lower Nut complex. It was formed in the early stages of the post-rift phase of the basin development. The sediment thickness of this structural-stratigraphic complex in the region under consideration reaches 1.5 km or more. The prevalence of folded dislocations is characteristic, and the structural forms of the complex are grouped into a series of meganticlines and megasynclines of submeridional and north-north-western strike. The Middle-Late Miocene Okobyk-Low Nut oil and gas deposits are characterized by significant changes in lithofacial composition. From bottom to top and from east to west, the structure of the complex varies from marine clayey-siliceous sediments to shallow-water, lagoon and delta clay-sandy. In the Middle Miocene, as a

result of transgression, the delta front moved west. In the late Miocene, the Avandelta of Paleoamur was located in the northern part of the modern northeastern shelf of Sakhalin. The Chayvinskoye deposit and the deposits of the Odoptinsky anticlinal zone are associated with avandelta deposits [19].

The main productive strata in the Astokh site are confined to the sandstones of the Lower Nutov subhorizon of the Upper Miocene. Sandstones are weakly cemented, from coarse to fine-grained. Hydrocarbon deposits are located in 6 strata of the Astokh site. Productive formations are XIX1, XXIs, XXI1', (the XXI1' layer is divided into upper, middle and lower layers), XXIII, XXIV and XXV layers. The deposits in the XIX1, XXIs, XXI1' reservoirs are oil, the reservoir in the XXIII reservoir is oil and gas condensate, and the reservoir in the XXV reservoir is gas condensate. The total thickness of individual productive formations varies from 1.9 to 95 m. The thickness of the silty-clay sections varies from 2.1 to 123.0 m [19].

The Verkhnenutovsky complex is characterized by a relatively small thickness (up to 700 m) and weak intensity of plicative dislocations. Disjunctive dislocations are almost absent. The sediments of the complex are predominantly marine and shallow-water sandy-clayey rocks with little gravel and pebble material. Up the section, there is an increase in the share of loose rocks - sandstones, clays, sand and gravel deposits and, as a result, a decrease in the strength of the rocks. At the contacts of different lithology layers, weakly cemented areas and interlayers are observed in places. Studies conducted by the DMYHE in 1992 showed that in the deposits of the Upper Pliocene there are separate lenses of gas-saturated sediments lying shallow from the bottom surface [19].

4.2.1 Reservoir XXIs

Sandstones of the XXIs formation are powerful, massive, clayey, and weakly cemented. These sandstones, as a rule, have undergone bioturbation and are sometimes interspersed with individual interlayers of poorly sorted, medium- and coarse-grained pebble sandstones. The porosity, according to well logging, is 20–29%. Sandiness varies from 0.40 to 1.00. The thickness of the XXIs layer within the Astokh site

decreases from west to east, while the maximum thickness of 32.2 m is noted in the well. No. 1, and the minimum, equal to 11.4 m in the well. Number 3.

Within the interval of occurrence of the XXIs layer, two sand lithofacies are accumulated under high-energy conditions. One of them lies at the bottom of the XXIs layer, and the other lies in the roof of this layer. Core and log data indicate that the upper lithofacies of XXIs are sandstone with low clay content and high permeability. She received an informal name - "Lithofacia1". Lithofacia 1 has a thickness of 0 to 17 m and is characterized by low values of acoustic impedance. The porosity of the rocks of this lithofacies often exceeds 25%, and the permeability exceeds 1000 mD. The average values of the reservoir parameters for lithofacies 1, obtained according to well logging data, are:

- Porosity (average) 26.0%
- Water saturation (average) 14.7%

Below the lithofacies interval 1, clayey sandstone with lower permeability is located. This lithofacia received an informal name - "Lithofacia 2". This lithofacia has a slightly lower porosity (23-26%), compared with lithofacia 1, and significantly lower permeability (100 - 500 mD). The average values of the reservoir parameters for lithofacies 1, obtained according to well logging data, are [19]:

- Porosity (average) 24.1%
- Water saturation (average) 14.9%

4.2.2 Reservoir XXI'

Reservoir XXI' is a dominant interval (up to 65 m thick) composed of thin-layered, fine- and fine-grained sandstones, interbedded with layered siltstones, and individual interlayers of clays. The thickness of individual sand lenses is usually 0.5 - 3.0 m, the porosity, as a rule, reaches 25%, and the permeability does not exceed 1000 mD. The nature of seismic reflections from the surface of sand bodies and the assessment of the heterogeneity and discontinuity of sandstones between drilled wells indicate that the

formation has a complex lenticular structure. Based on a joint analysis of GIS materials with seismic data, reservoir XXI1 'is divided into upper, middle and lower layers.

4.2.3 Reservoirs I-IV

This interval is represented by thin intercalation of clays and sandstones with a total thickness of 136 to 172 m. The thicknesses of sandy layers vary on average from 1 to 7 m. The composition of sandstones is quartz-feldspar. Sandstones - well-sorted, fine-grained, well-cemented. Cement in individual interlayers is predominantly carbonate. Grain rounded medium to good. Pyrite inclusions occur. The porosity determined according to the GIS data varies within 15-20%. Clays are grey, dark grey, plastic, and in some places, siltstone. The mineral composition is illite, illite-smectite. Kaolinite and chlorite are also found in significant quantities [19].

4.2.4 Reservoirs V-VI

The thickness of the interval varies from 29 m in the well. PA-122 up to 53 m in the well. PA-118. This interval is represented by clayey strata. Clays are grey, dark grey, plastic, and in some places, siltstone. The mineral composition is illite, illite-smectite. Kaolinite and chlorite are also found in significant quantities [19].

4.2.5 Reservoirs VII-VIII

According to borehole data, the thickness varies from 95m. in well PA-003 up to 118m. in well PA-122BS3. The stratum is represented by an alternation of clay and sand aleurolitic packs with a thickness of 2 to 10 m. The thickness of individual sand packs sometimes reaches 20 m. The stratum is represented by fine-grained sandstones, well sorted. Grain rounded is medium to good. Sandstones are solid, well cemented, carbonate cement (up to 5%). The mineralogical composition of sandstones is quartz-feldspar. Clays are grey, soft, plastic, sandy. By mineralogical composition - they are similar to clays of the interval of formations I-IV [19].

4.2.6 Reservoir IX

The thickness of the reservoir varies from 27 m in the well. PA-122BS2 up to 37 m in a well. PA-116. Lithologically, the formation is subdivided into two packs: the upper

sand and the lower - clay. The thickness of the sand layer reaches 15 m, clay - up to 30 m. Sandstones are very well sorted, fine-grained. Grain rounded is medium to good. The composition of sandstones is quartz-feldspar. Clay and carbonate cement are presented (up to 6%). Clays are light grey, grey, hard. The mineral composition is similar to clays of formations I-VIII. Pyrite inclusions occur [19].

4.3. The development Project

The field development project is based on the results of exploratory drilling, and three-dimensional seismic and is a combination of a number of directional production wells operating in the mode of joint operation of several reservoirs and several horizontal wells drilled into separate reservoirs. Reservoir pressure maintenance is carried out through “intelligent” injection wells with selective control of injection from the surface at each interval. To penetration the main oil reservoirs in the middle of the oil rim, wells must be drilled with a large angle of inclination. As a result of this, as well as in connection with the platform’s location far from the whale feeding grounds, the well trajectories are very complex and resemble a “fishing hook” in projection, as shown in Figure 4.2 [20].

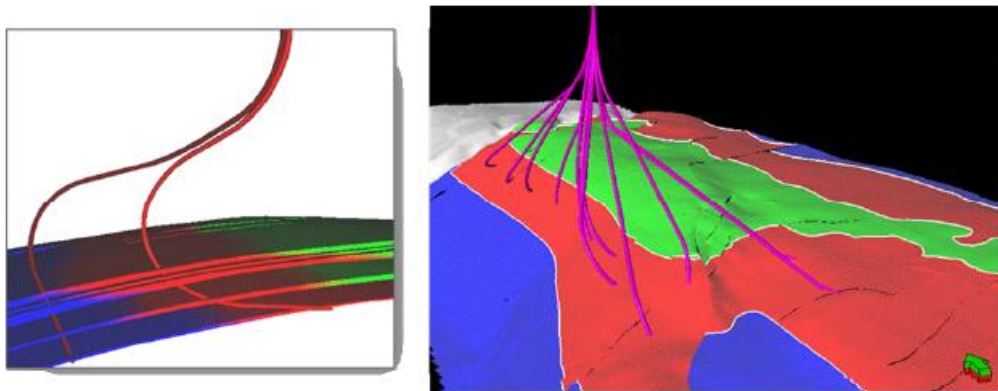


Figure 4.2 Well trajectories characteristic of the Piltun site [20]

The difficulties associated with conducting well trajectories in such a way that they exposed formations in the central part of the oil rims, were supplemented by a significant degree of uncertainty in the positions of gas-oil and water-oil contacts, which were not discovered by any of the exploration wells at the Piltun site. The results of geophysical studies and testing obtained from exploratory wells, together with the

results of three-dimensional seismic, were used to assess the position of interphase contacts and the degree of their uncertainty. As a result, enough data was collected on the geological structure and position of the contacts to justify the start of work on the site (see Figure 4.3), but not enough for optimal development of the site.

Continuation of work without specifying the position of the contacts could lead to a high risk of placing several complex wells in places where the wells could not drain oil rims. A more traditional approach included drilling more exploratory wells at an early stage in the development of the site, which would be a more expensive option, and in addition, additional drilling “windows”, the number of which on the offshore platforms, would be used to drill exploratory wells. The start of production drilling would be delayed, and thereby, future revenues would be reduced.

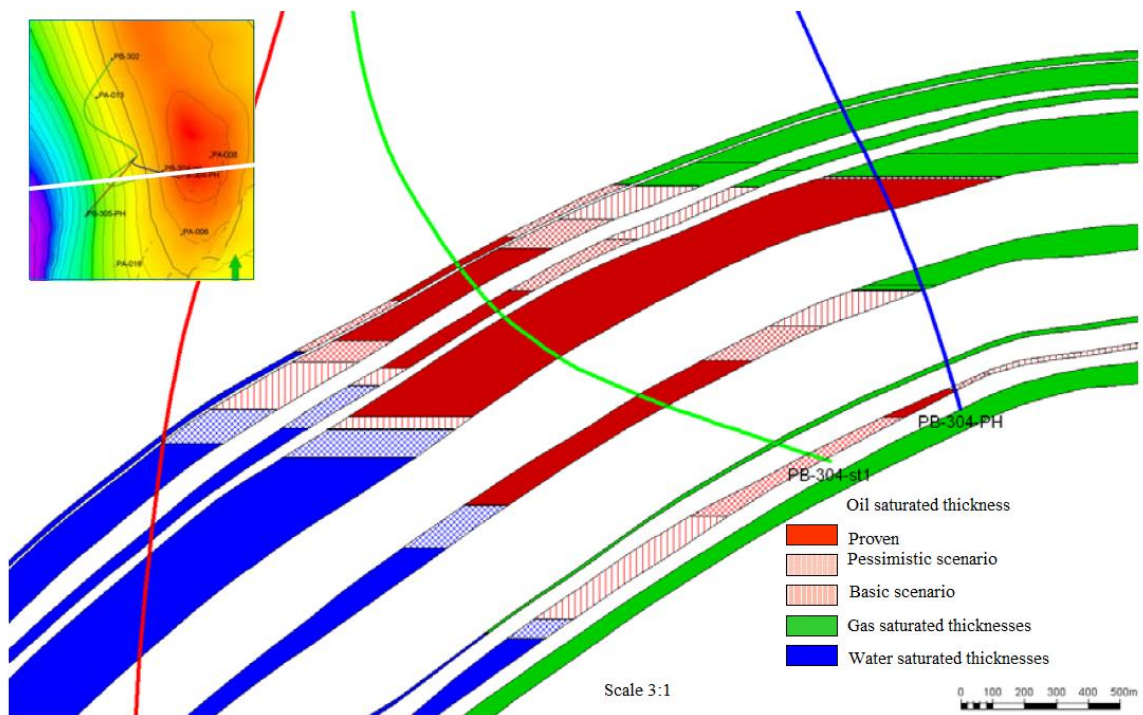


Figure 4.3 Presentation of the interphase contacts position of the Piltun site before the start of production drilling [20]

In the case of the Piltun region, another option was chosen, which, with a slight increase in capital costs for drilling the first production wells, also involved the drilling of pilot shafts to collect relevant information about the occurrence of productive formations. Their reservoir properties and the position of interphase contacts, which was achieved

as a result of geophysical research during drilling, measurement of reservoir pressures and sampling in gas-, oil-, and water-saturated thicknesses of each formation [20].

When drilling the first production wells, two pilot shafts were drilled from them, as a result of which additional data on gas and water-saturated thicknesses were collected. These data were used in combination with data obtained in oil-saturated thicknesses of producing wells. The essential data obtained at the initial stage of development of the site include reservoir pressures and the results of the analysis of deep samples taken in the first wells with pilot shafts, which were then used to plot the dependence of reservoir pressure on depth to calculate the position of interphase contacts. In each case, reservoir pressures and fluid samples were obtained using a pressure and depth sampling device. In connection with large angles of inclination of the wells, the device was lowered on pipes. Besides, when assessing the complexity of future operations and taking into account the fact that any delays or failures during their implementation will have an extremely negative economic effect. Additional measures were put into the program when planning to increase the efficiency of future operations. Sakhalin Energy actively uses information and technical infrastructure in its work, which allows real-time processing of data obtained during drilling. The same approach was used in studies with a modular-dynamic reservoir tester, which provided round-the-clock support for platform personnel with specialists from the Sakhalin Energy office and experts from the Shell center for sampling and analysis of fluids. This support was critical for effective data collection (i.e., ensuring the stability of pressure measurements, conducting measurements not subject to the effect of overpressure in the bottom-hole zone due to slow pressure equalization after penetration of the mud filtrate and subsequent measurements at a distance of at least 1-1,5 m in absolute depths from the previous measurement).

The choice of pressure measuring points that met all the criteria was tough due to the considerable variability of reservoir properties in each test interval and often the insufficient quality of the reservoir for proper metering. The first pressure measuring points (in gas-saturated thicknesses) were preliminarily selected based on the results of

standard geophysical studies during drilling when areas with excellent reservoir properties with the best values of hydraulic conductivity were determined, and from which reliable measurements of the reservoir pressure could be made. Good points for measurements were selected at depths with relatively low gamma-ray logs in combination with low-density logs (i.e., intervals with high porosity) and high values of logging resistance (i.e., high saturation). Despite the fact that enough points were determined for the successful implementation of the work program, there were also points where it was impossible to record the pressure value. During the following pressure measurements (in oil-saturated thicknesses), pressure measurement points were preliminarily selected based on the results of permeability estimates obtained by the method of nuclear magnetic resonance (NMR) recorded during drilling. This approach allowed to obtain a noticeable improvement in the quality of work.

4.4. Hardware Information

4.4.1 Platform "PA-A" (Molikpaq)

Gravity based platforms are considered the most stable and reliable structures for installation in the seas at a depth of 20-150 meters. A wide choice of bases allows to install them on the bottom of the sea without additional mounting in the form of piles. These types of platforms remain stable in any weather, even during a storm. In the lower part, they are equipped with ballast tanks, with which the platform can be transported by sea from the construction site to the drilling point and install it at the bottom of the sea, filling the ballast tanks with seawater or sand. At the base of the gravity platform, guide columns for drilling, and storage tanks for produced oil with a capacity of up to 500-600 thousand m³, pipelines are placed. The presence of storage makes it possible not to stop oil production even in bad weather when tankers cannot approach the platform.

The Molikpaq platform was originally installed on the Canadian shelf in the Beaufort Sea, however, was purchased by Sakhalin Energy Investment Ltd. to work under the Sakhalin 2 project at the Piltun-Astokhskoye field. The climatic conditions of the Canadian and Sakhalin shelf are different, so the platform has undergone modernization. The platform was upgraded at the Korean factory Samsung. Green in Figure. 4.4 shows what the platform was completed in Canada, and in yellow what was added at the Korean plant, as well as in Russia. As can be seen from Figure 4.4, the following modules were added: a module for waterflooding, a technological module, energy, gas, oil modules and others. Figure 4.5 reflects the general model of the Molikpaq platform before it arrived in Russia, the main differences are that there are no wave deflectors and the caissons differ.

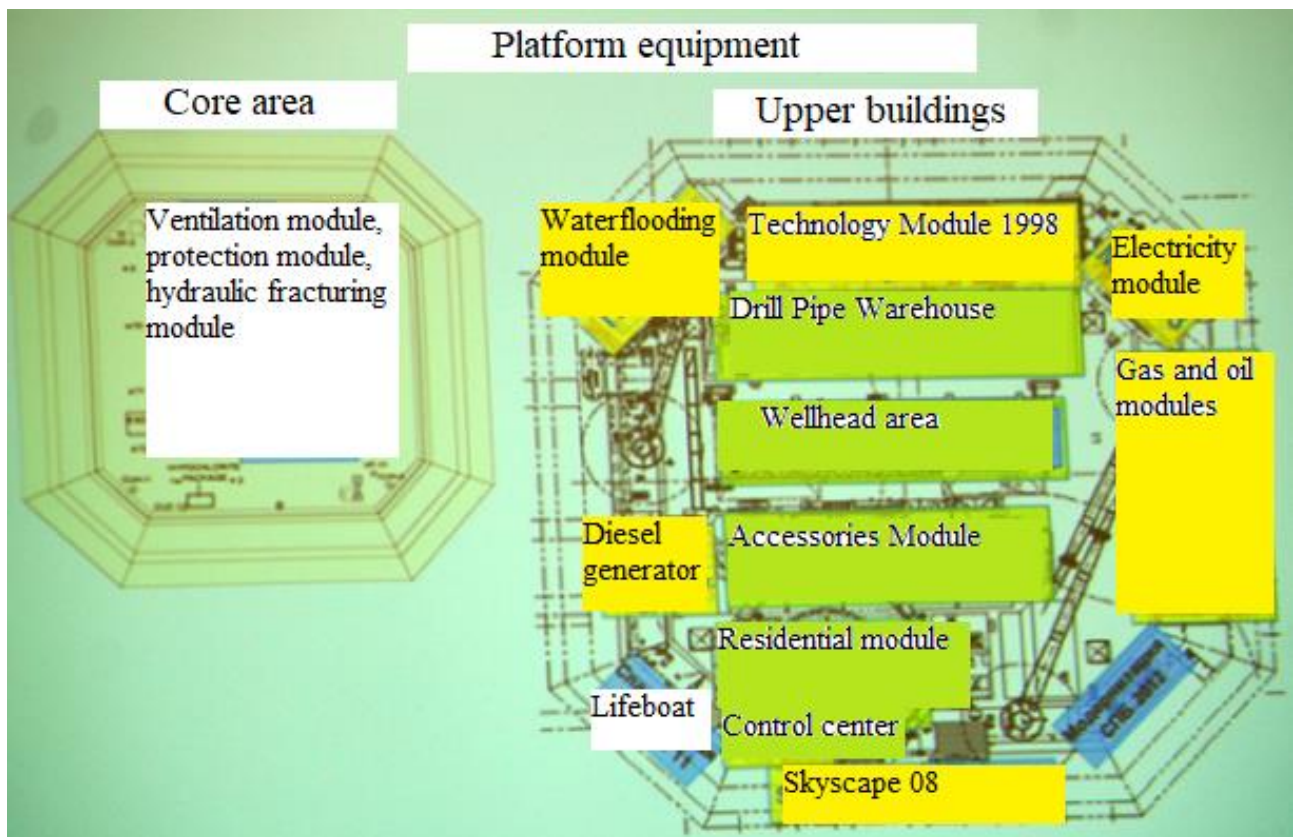


Figure 4.4 Equipment of the Molikpaq platform [23]

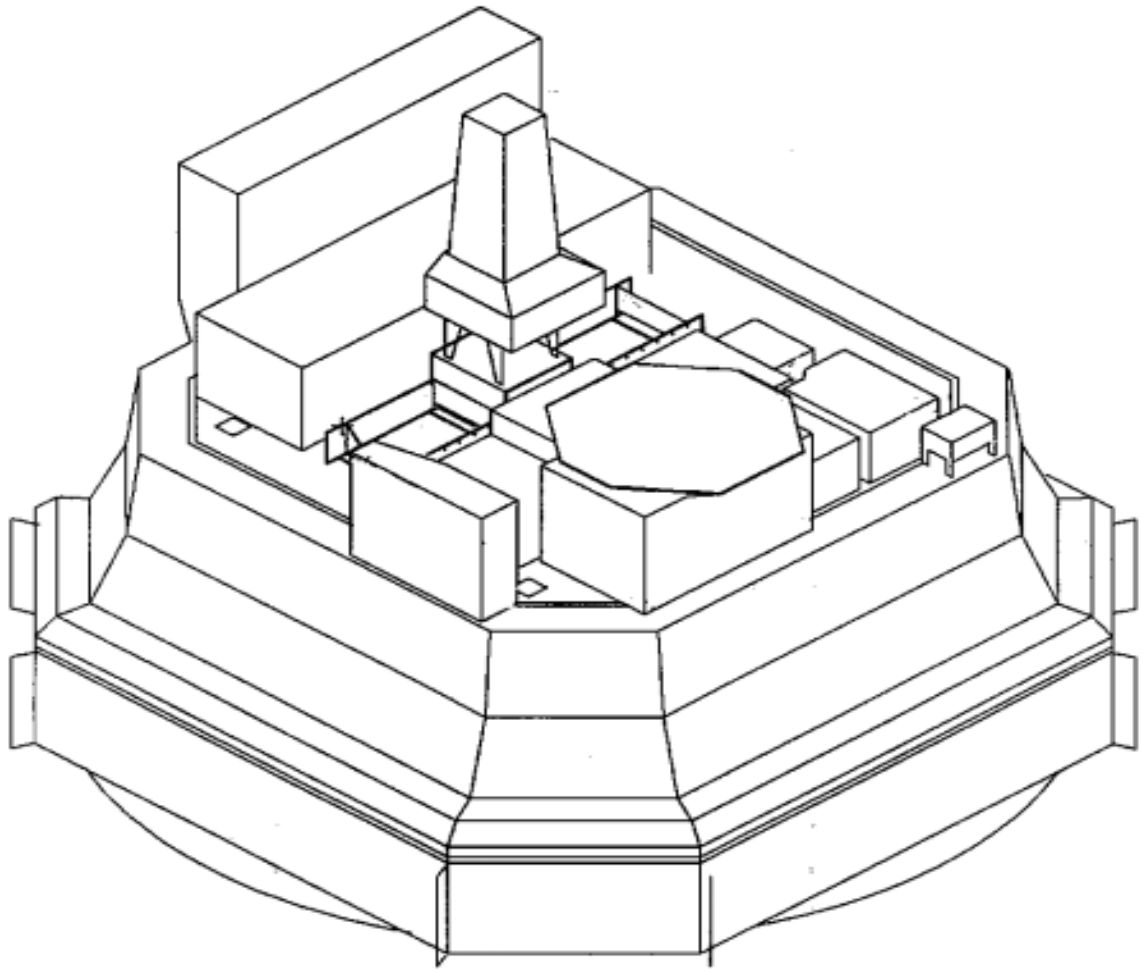


Figure 4.5 Model of the Molikpaq platform before modernization [24]

Before upgrading the platform, it was necessary to conduct tests to establish the value of the ultimate load on the walls of the platform, to protect the caisson from waves, ice and wind. The test results showed that the added wave deflectors provided sufficient protection for existing modules on the northern edge of the one-sided octagonal platform. Modified deflectors reduced the load on the other sides within the existing module capabilities. The deflector was installed on the north side. The platform was one of the most advanced and most innovative after the modernization. Although it was also necessary to strengthen some of the internal partitions of the caisson in order to distribute the expected wave loads on the deflector, its design made it possible to prefabricate most of the deflector elements at the shipyard. Such a deflector design

would not have been developed without the use of simulation. Figure 4.6 presents the Molikpaq platform with the wind and wave deflector [24].



Figure 4.6 Photo of the Molikpaq platform after modernization [24]

The base of the platform is 111m x 111m, and the upper structures are 73 x 73m, the height of the tower is 101 meters, the total mass of the platform with all modules is 54 thousand tons.

This modification has 32 drilling slots. According to the data for 2019, the total field included 25 wells: 17 oil-producing wells, seven wells for the reservoir pressure maintenance system (RPM), as well as one for drilling waste. Over the entire life of the platform, more than 40 million tons of oil will be produced. [23].

Measurement of ice loads on the Molikpaq ice-resistant platform, which for five years (1984-1989) was used as a drilling platform in the Beaufort Sea, became a source of relevant information on the nature and extent of impacts on large marine structures with annual and perennial ice. The outer shell of the caisson had an inclined profile at 8° and 23° from the vertical. In order to measure ice loads, the platform was equipped

with three different measuring systems: pressure sensors in the form of MEDOF contact panels, strain gauges, extensometers and accelerometers (Figure 4.7).

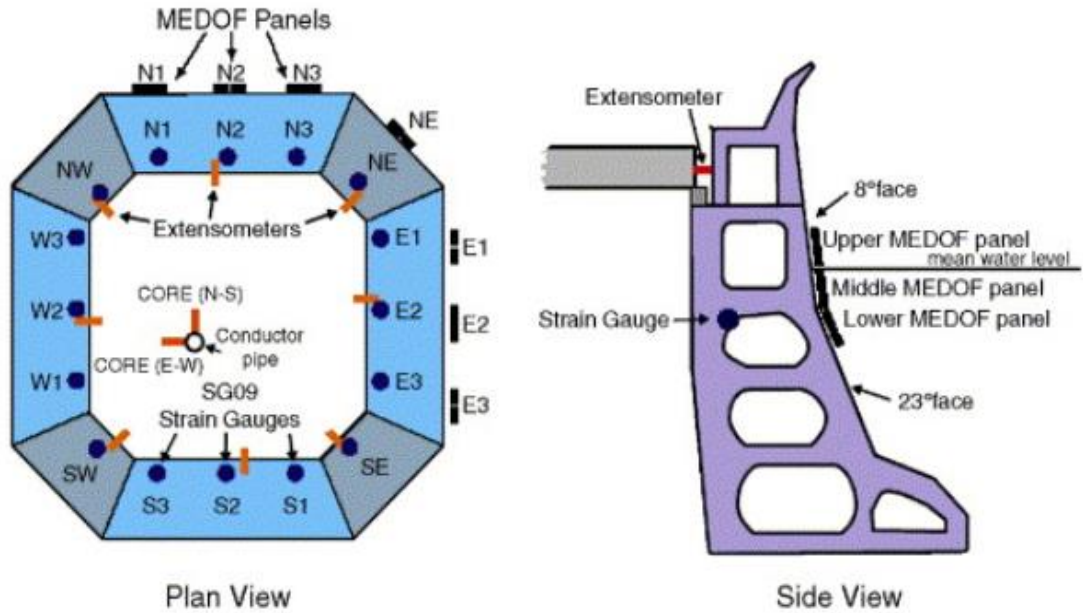


Figure 4.7 Ice load measurement instrumentation on the Molikpaq [25]

4.4.2 Platform "PA-B"

Figure 4.8 shows the Piltun-Astokhskaya-B offshore platform for oil and gas. This platform was installed in the Sea of Okhotsk in the Piltun-Astokhskoye field in late summer 2005 as part of the Sakhalin 2 project. The platform is located twelve kilometers from the coastline and stands at a depth of 32 meters [23].



Figure 4.8 Photo of the Piltun-Astokhskaya-B platform [23]

Piltun-Astokhskaya-B is a gravity-based platform that is installed at the bottom of the Sakhalin shelf and stands on four reinforced concrete supports. The platform carries out year-round oil and gas production, primary oil preparation, as well as storage since a reservoir is located in one of the supports. The southeast support is used as a platform for wells, the northeast support for the placement of risers of the offshore oil and gas pipeline. In the upper modules are a separation unit, a residential unit, a unit for storing reagents, a drilling unit and others. The working areas are carefully fenced with iron fences that protect the working space from the wind. Also, these fences reduce the air temperature in winter, which allows working comfortably in harsh winters.

It should be noted that these are not blind barriers. That is done so that the working area is well ventilated. All equipment is equipped with ice protection.

PA-B is the largest platform among all installed in the framework of this project. Its mass is 119,000 thousand tons, and the total height reaches 120 meters, which is comparable to a thirty-floor building. It should be noted that the height of the supports is 56 meters, and the upper buildings are 53 meters. The platform is 94 meters long and 91.5 meters wide. The upper structures of the platform, as well as part of the Molikpak platform, were built at the Samsung factory in South Korea. The concrete base of the platform was designed and built by Aker Kvaerner Technology and Kvatrodzhemini in the Far East.

To date, 28 wells are located in the PA-B well stock. Eighteen are used for oil-producing, 8 for water injection and 2 for waste absorbing.

By 2019, more than 16 million tons of oil was produced on this platform. The average daily production amounted to 4.39 thousand tons of oil and 1.33 million m³ of associated gas.

Chapter 5. Analysis of equipment applicability and proposed improvements

5.1. Flow meter

On the Piltun-Astokhskaya-B platform, a module for primary oil treatment and refining is installed. The structure of this module includes an ultrasonic liquid flow meter. Table 5.1 shows its performance characteristics [23].

Table 5.1 Performance characteristics of the ultrasonic flowmeter "300-082-FT-003"

1 GENERAL					60 GENERAL				
2 Tag No		300-082-FT -003			61 Area Classification		ZONE 1 IIB T3		
3 Service		P8202A/BIEXPT CRUDE			62 Ingress Protection		IP 65		
4 Line size-line Num-schedule		10"-PL82336-91500X-EP			63				
5 Piping Class Line ID (Inch)		900#	9.062		64				
6 PEFS drg number		3000-T-82-08-D-8420-01			65 Basis of Selection		NA		
7					66 Design Code		NA		
8 PROCESS DATA					67 ULTRASONIC METER ELECTRONICS				
9 Medium Phase		OIL			68 Mounting-Integral or Remote		INTEGRAL		
10 Weight % Solids					69 Power Supply From		230 VAC	UPS	
11 Operating Conditions		Min	Norm	Max	70 Output Signal Active Passive		4-20mA	PASSIVE	
12 Flow Akg/h		14200	410700	452025	71 HART Fieldbus		HART		
13 Pressure (upstream) bar-g		90.4	90.4	90.4	72 Electrical Connection Type		SCREW TERMINALS		
14 Temperature °C		50	50	50	73 Cable Entries		M20 x 1.5mm ISO		
15 Density kg/m³		861	861	861	74 Integral Indicator - Scale		INTEGRAL	DIGITAL	
16 Viscosity cP		2.1	2.1	2.1	75 IP Code		IP 67		
17 Max Velocity m/s		0.1	3.2	3.5	76 Certification - Electronics		CENELEC EEx de		
18 Medium Composition					77 Certification - Power Supply				
19					78 Casing Material		316 SS		
20 Mol Weight					79 Calibrated Range Min Max		0	700	m³/h
21 Type of Flow					80 Engineering Range Min Max		350	3500	m³/h
22 Max Allow. Press.Drop		0	mbar		81 Accuracy		+/- 0.5 % of MV		
23 Ratio of Specific Heat (cp/cv)					82 Low Flow Cut-off		AJUSTABLE 1 to 20 %		
24 Compressibility Factor					83 Crippled Mode Detection		Self Diagnosis Function		
25 Corrosive Agents		Yes Dissolved CO2			84 Burn-out Direction		HIGH		
26 Toxic Agents		Yes H2S			85 2nd Output Signal		NOT REQUIRED		
27					86 Digital Outputs		NOT REQUIRED		
28 Reference Conditions Press Temp					87 Calibrated Range 2nd Output		NOT REQUIRED		
29 Design Pressure Max Min		130	bar-g	-1	bar-g	88 Accuracy		NA	
30 Design Temperat. Max Min		90	°C	-39	°C	89 Model Number		UFC030K/D/EEx	
31 ULTRASONIC METER ELEMENT					90 ACCESSORIES				
32 Measuring Method		TIME OF FLIGHT			91 Special Vendor Cable		NO		
33 Measuring Tube-Flange Material		316L SS			92 Special Cable Length		NA m		
34 Measuring Tube Internal Diameter		230.2 mm			93 Integral Calibration Facility		NA		
35 No of Beams(B) Transverse(T)		2(4 Sensor)	YES		94 Transducer Alignment install. Kit		NA		
36					95 Flow Conditioner - Material / Size		NA		
37					96 Flow Conditioner - Model Number		NA		
38					97				
39 Meter Size		10 in			98				
40 Inlet Flange Size Rating Facing		10"	900#	HUB	99				
41 Outlet Flange Size Rating Facing		10"	900#	HUB	100				
42 Process Connections		HP HUBBED			101				
43 Face to Face Dimensions		1200 mm			102				
44					103 SPECIAL REQUIREMENTS				
45 Transducer Type					103 NACE Requirements		MR 01 75		
46 Transducer Material		316L SS			104 Certification Approval number		PTB No 3 ATEX 2021X		
47					105				
48					106 Material Cert.		Req'd to EN 10204 3.1B		
49					107 Special Req for Service				
50 Calculated Press. Drop @ Full Flow		0	mbar		108				
51					109				
52 Model Number		UFM 530HP/K/D/EEX			110 Paint Finish		See General Notes Sht 3		
					111 Weight		350 kg		

This flow meter has a mass of 350 kg. "300-082-FT-003" is made of 316L SS stainless steel. This is austenitic high-strength steel, which is resistant to corrosion, can operate in a wide range of operating temperatures and pressures. The main advantage is the addition of molybdenum. The Russian analogue of such steel is 08X17H13M2.

Within the framework of this thesis, it is proposed to replace the liquid acoustic flowmeter installed on the PA-B platform with a liquid differential pressure flowmeter, see Chapter 6.1 for a discussion of economic merits. This is a conventional flowmeter with sharp edges, which is shown in Figure 5.1.

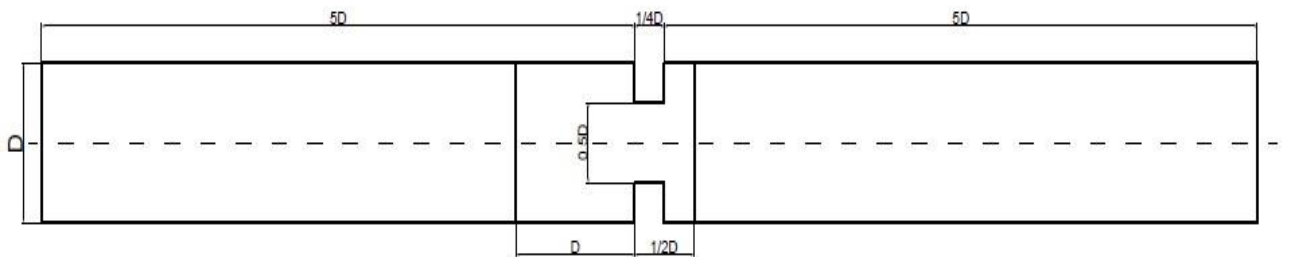


Figure 5.1 Drawing for sharp-edged orifice

However, if the acoustic flowmeter will be replaced with this one, then the economic effect will be little noticeable, so it is necessary to optimize this design. Computer simulations were performed using OpenFOAM software packages.

5.1.1 Introduction to Computer Simulation

CFD is part of continuum mechanics. CFD includes physical, numerical, and mathematical methods for calculating flow characteristics. There are many programs for calculating the flow characteristics of a liquid, gas, etc., for example, Phoenix, Star-CD, Autodesk Simulation CFD, OpenFOAM, and others.

CFD methodology:

Pre-processing: First of all, it is necessary to define own goal after that build a virtual geometrical model for CFD simulation by using special CADs or something like this. In order to define the boundaries of an object usually meshing is applied. For a mesh creation, it is important to select an appropriate meshing strategy. Also, the criteria for

modelling as a fluid movement equation should be defined. In the case of this simulation, the Navier-Stokes equations were used:

$$\text{Continuity equation: } \frac{\partial u}{\partial x} + \frac{\partial v}{\partial y} + \frac{\partial w}{\partial z} = 0 \quad (5.1)$$

$$\text{For } x, \quad \rho \frac{Du}{Dt} == -\frac{\partial P}{\partial x} + \rho g_x + \mu \nabla^2 u \quad (5.2)$$

$$\text{For } y, \quad \rho \frac{Dv}{Dt} == -\frac{\partial P}{\partial y} + \rho g_y + \mu \nabla^2 v \quad (5.3)$$

$$\text{For } z, \quad \rho \frac{Dw}{Dt} == -\frac{\partial P}{\partial z} + \rho g_z + \mu \nabla^2 w \quad (5.4)$$

Solving: At this part the simulation starts, in which the equations of mass, energy and moments are solved. These equations are given as initial boundary conditions. There are several types of approaches to solving equations, such as the finite element method, finite volume, finite difference, and spectral method. Governing equations should be solved. Discretization is a part of solving the stage.

Post-processing: At this stage, the results are obtained. There are a lot of programs for visualization, these programs provide great opportunity to clearly understand own post-processing results.

In this thesis, OpenFOAM was used.

5.1.2 OpenFOAM

OpenFOAM is a program designed for the numerical simulation of continuum mechanics. Initially, the code for this program was developed in the UK. As a result of development, this platform allows to perform complex calculations and solve many problems associated with the mechanics of continuous media. As stated in Wikipedia, the range of tasks includes heat conduction problems, strength calculations, hydrodynamics of Newtonian and non-Newtonian viscous fluids (in this case, incompressible), determination of hydrodynamic characteristics for multiphase flow, and so on. One of the main features of this program is the ability to parallelize the

calculation to run the simulation on several processors, this allows you to significantly optimize the speed of the simulations. The main programming language in this program is Object-Oriented Programming (OOP) C ++. In connection with the use of this language, the reading of mathematical and tensor operators is simplified. It is easy enough to write the differential equation in a script. This platform has several branches, one of them on the Windows operating system, however, the most successful Linux-based software package has proven itself.

5.1.3 Discharge coefficient

The discharge coefficient equals the ratio of actual flow rate (Q_{exp}) to theoretical ($Q_{theoretical}$) [26]:

$$C_d = \frac{Q_{exp}}{Q_{theoretical}} \quad (5.5)$$

There is no pressure loss, it is unphysical, because of the frictional effects. In order to solve it and make a balance, discharge coefficient was implemented. C_d could be expressed from the flow rate equation:

$$Q = S_2 * C_d \sqrt{\frac{2\Delta P}{\rho(1 - \beta^4)}} \quad (5.6)$$

Where S_2 is a cross-section area of the orifice. The flow rate is equal to the flow rate passing through the section per unit time. Also, the velocity can be expressed as follows:

$$v_{average} = C_d \sqrt{\frac{2\Delta P}{\rho(1 - \beta^4)}} \rightarrow C_d = v_{average} * \sqrt{\frac{\rho(1 - \beta^4)}{2\Delta P}} \quad (5.7)$$

Also, it is well known that C_d coefficient depends on Reynolds number and there is the equation with empiric coefficients [27]:

$$C_d = 0.5959 + 0.0312 * \beta^{2.1} - 0.184 * \beta^8 + \frac{91.75 * \beta^{2.5}}{Re^{0.75}} \quad (5.8)$$

This equation may be applied for $0.25 \leq \beta \leq 0.75$ and $10000 \leq Re \leq 10000000$.

In this thesis, Eq. (5.7) was used as base for discharge coefficient calculation.

5.1.4 Basic laws applicable to the diaphragm

The flowmeter is a device for measuring the flow of liquid, steam or gas. In the oil and gas industry, the flow rate of liquid, steam or gas, i.e., the amount of substance flowing through the pipeline per unit time, is measured by flowmeters. The most widely used are differential flowmeters, which measure the pressure by the differential. The pressure is created in the pipeline by a constriction device installed inside the pipeline.

The concept of the upgraded flowmeter is shown in Figure 5.2.

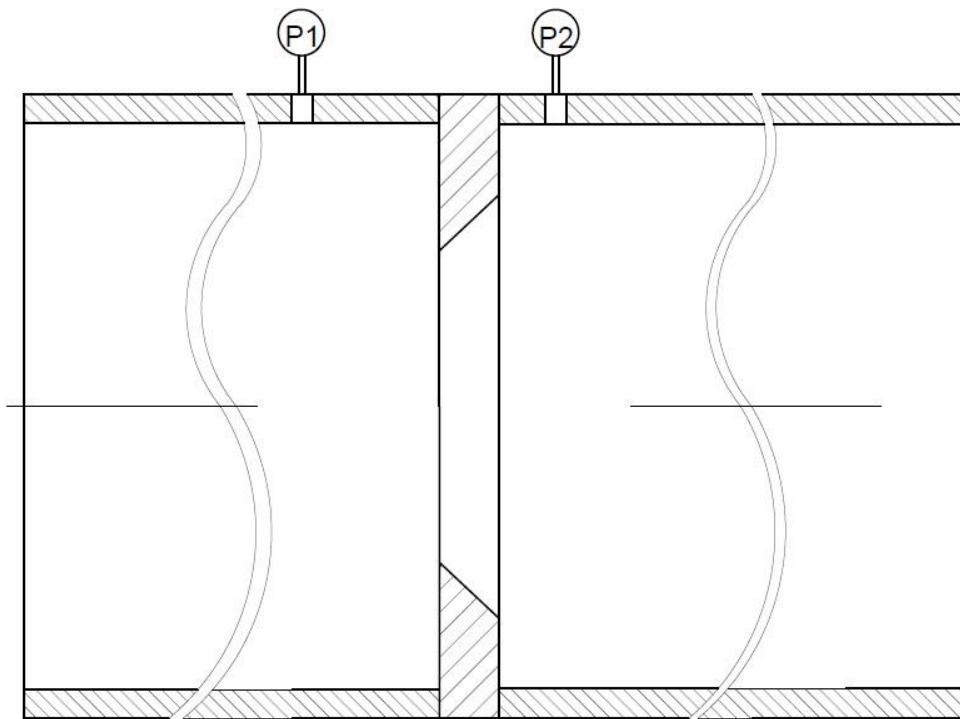


Figure 5.2 Orifice with back bevelled edges

The principle of orifice flowmeter is based on Bernoulli equation:

$$\frac{P_1}{\rho * g} + \frac{v_1^2}{2g} + z_1 = \frac{P_2}{\rho * g} + \frac{v_2^2}{2g} + z_2 \quad (5.9)$$

Where $\frac{P_1}{\rho * g}$ is the Piezometric height, $\frac{v_1^2}{2g}$ is the speed height, z - the height at which the fluid element is being considered, g – gravitational acceleration, ρ is the fluid density.

Due to orifice horizontality, $z_1=z_2$ and $h = \frac{\Delta P}{\rho g}$; after that the velocity behind orifice is expressed as:

$$v_2 = \sqrt{2gh + v_1^2} \quad (5.10)$$

It's possible to write v_2 as:

$$v_2 = \frac{S_1}{S_2} * v_1 = \left(\frac{d}{D}\right)^2 v_1 \quad (5.11)$$

Where $\frac{d}{D} = \beta$, it's a ratio between the orifice diameter and the pipe diameter, S is cross-sections of the pipe and the orifice.

The most common are flowmeters with narrowing devices. They measure fluid pressure before and after the tapering device. In this case, a partial transition of the potential pressure energy to the kinetic energy of the velocity occurs, due to which the pressure in front of the narrowing point will be greater than behind the narrowed section. Typically, with the help of such flowmeters, the flow rate in pipelines with a diameter of 50-1600 mm is measured. When measuring flows with a low pressure, the differential pressure across the diaphragm may not be enough to organize the measurement. In such cases, it is possible to install two diaphragms with different diameters and select the pressure difference before the first and after the second. Diaphragms take first place among narrowing devices in terms of cost, ease of manufacture and installation. The diaphragm with back bevelled edges will be considered in the framework of this thesis.

5.1.5 Computer simulation of fluid outflow through a sharp-edged diaphragm

In order to start modelling the modernized diaphragm, it is necessary to check the correctness of the computer model. First, the grid should be created; this is done for

the calculation by the method of finite-difference elements. The next step is to verify grid convergence.

With an increase in the number of cells in the grid, the relative error should decrease less and less. After this check, the key value should be compared (expiration coefficient, speed and pressure in the diaphragm) with the values published and approved by scientists. That is why, to test the model, it must first perform a hydrodynamic computer simulation for a diaphragm with sharp edges. A numerical and experimental study on such a diaphragm was conducted by two Chinese scientists in 1996 [28]. Figure 5.3 shows a mesh for a diaphragm with sharp edges. As can be seen, the grid is crushed to the center of the narrowing apparatus, this is done in order to increase the accuracy of numerical modeling.

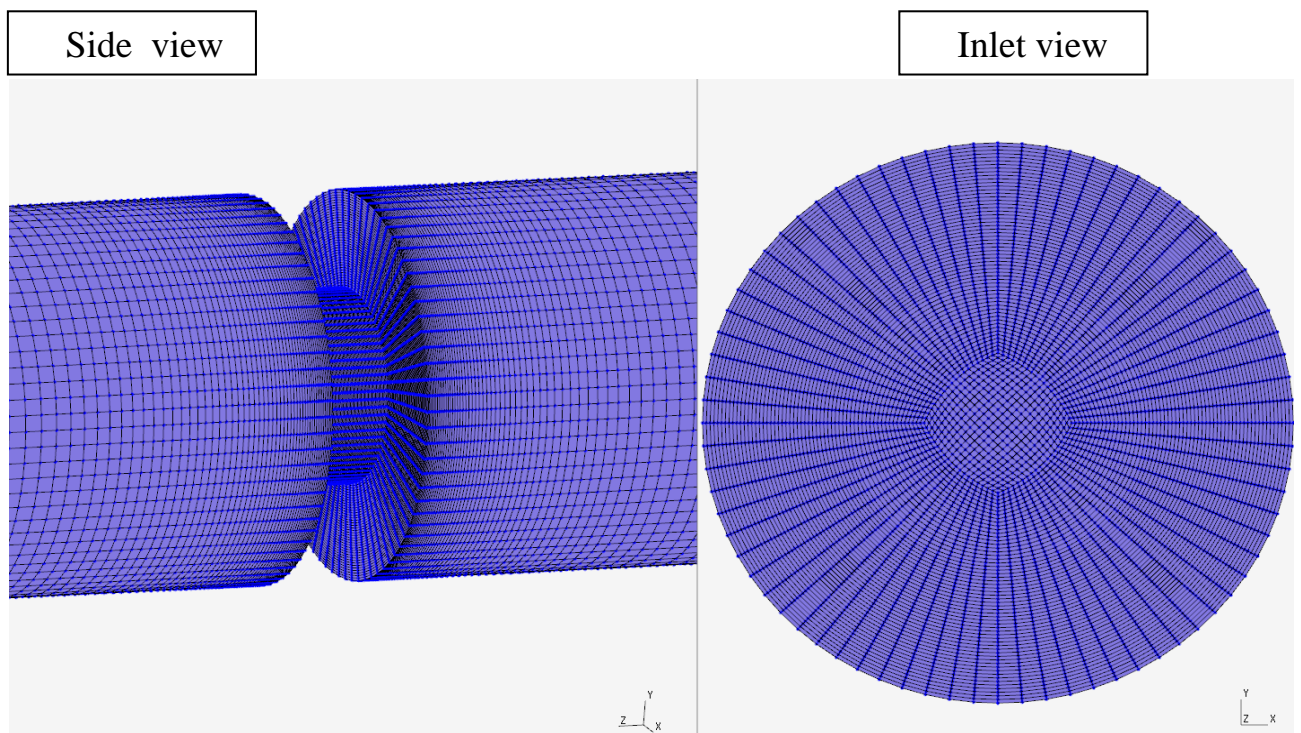


Figure 5.3 Mesh for the case of sharp-edged orifice simulations

Before proceeding to the main stage of modelling, it is necessary to choose the optimal number of cells so that the model does not overload the processors in the computer, but at the same time has high accuracy. The values of the main parameters for checking for convergence are given in Table. 5.2.

Table 5.2 Convergence study for meshes of the sharp-edged orifice

	Number of cells	Cd	Relative error %
Mesh 1	650000	0,695	0
Mesh 2 (was used for all cases)	1052000	0,705	1,418
Mesh 3	1299000	0,709	0,564
Mesh 4	1700000	0,712	0,421

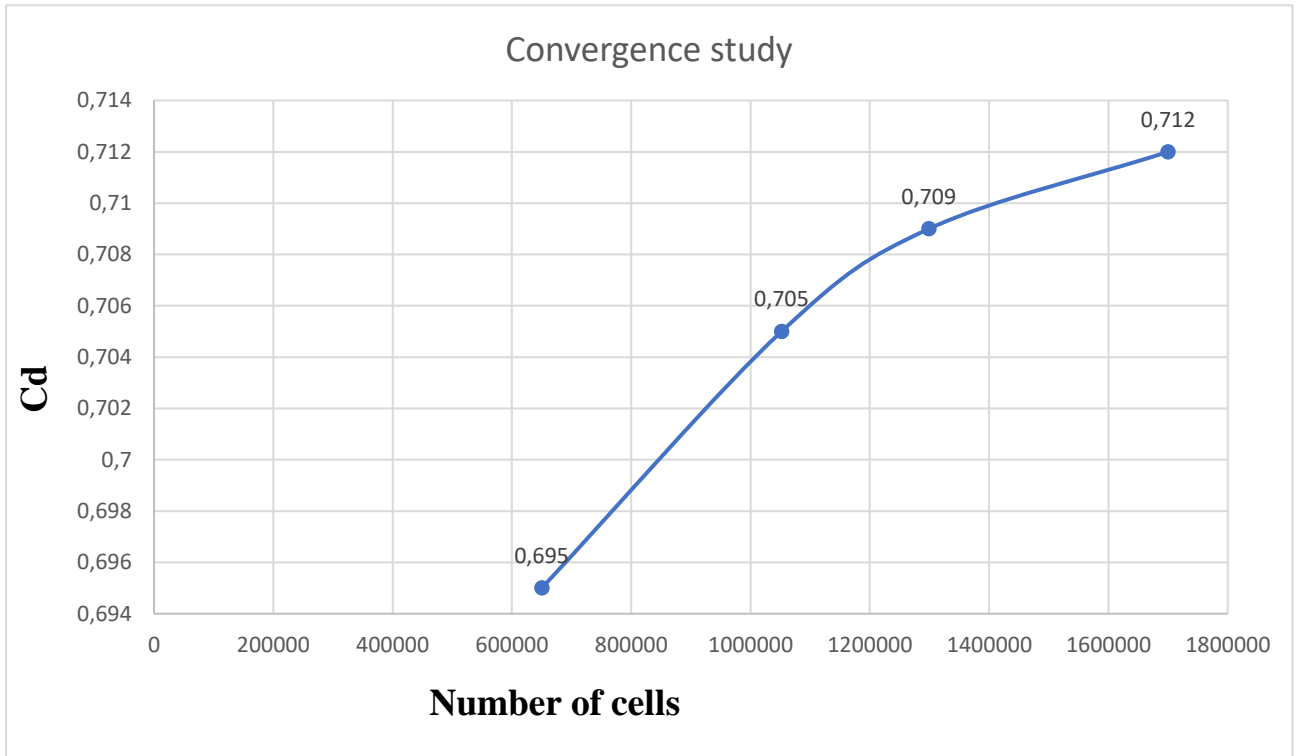


Figure 5.4 The dependence between C_d and different number of cells in the meshes

Next, the main numerical experiments with different Reynolds numbers were carried out, and the results were compared with those published previously. The results are presented in Figure 5.5.

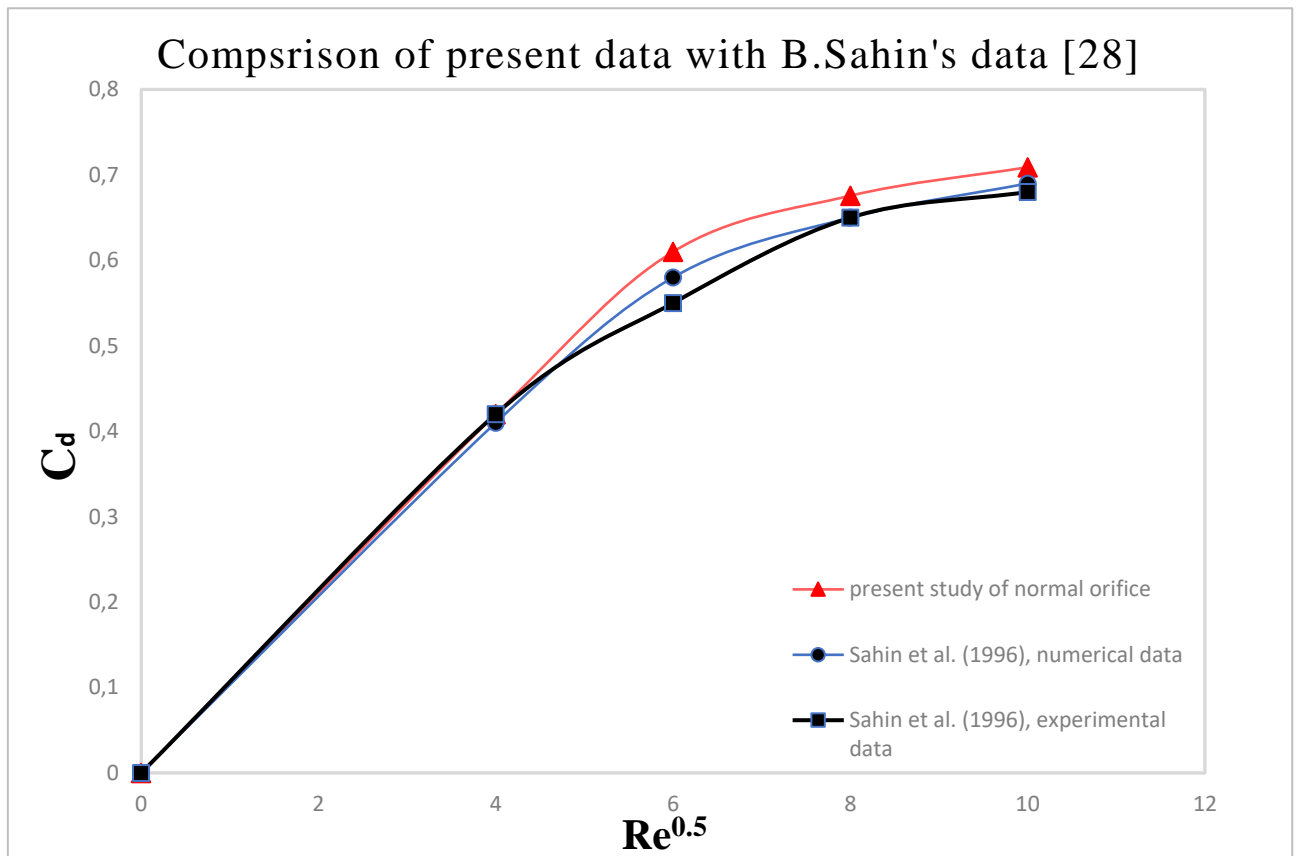


Figure 5.5 Numerical and experimental data in comparison with own results

The discharge coefficient is a dimensionless quantity that describes the behavior of the flow passing through the constriction (diaphragm). This coefficient describes the pressure loss behind the diaphragm.

5.1.6 Computer simulation of fluid flow through a diaphragm with beveled edges

After conducting the validation study of the orifice with back bevelled edges is carried out. In this part of the chapter, twelve simulations of laminar flow and one simulation of turbulent flow is performed, four simulations for each t^* and one additional simulation of turbulent flow in order to compare these results of laminar flow with turbulent flow in the pipe.

Inputs:

1. $t^* = 1/4, 1/8, 1/12$
2. $Re = 16, 36, 64, 100$ and turbulent (sharp-edged) $Re = 2500, 4900, 10000, 40000, 160000$
3. Length of the pipe $L = 10.5D$

4. Diameter of the pipe $D=D$
5. The bevel angle ϕ is constant and equal to 45°

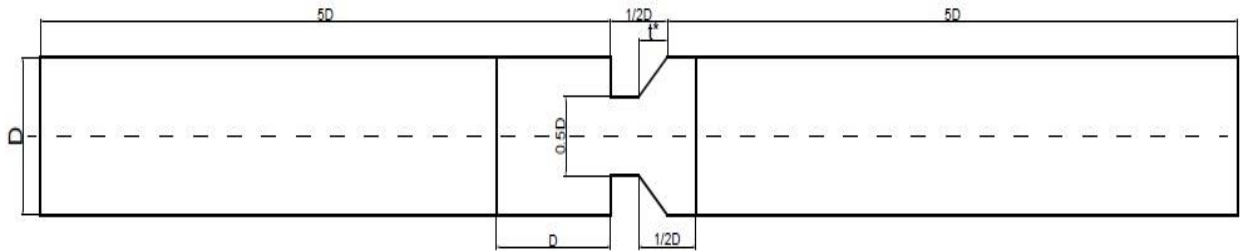


Figure 5.6 Drawing of the orifice with bevelled edges

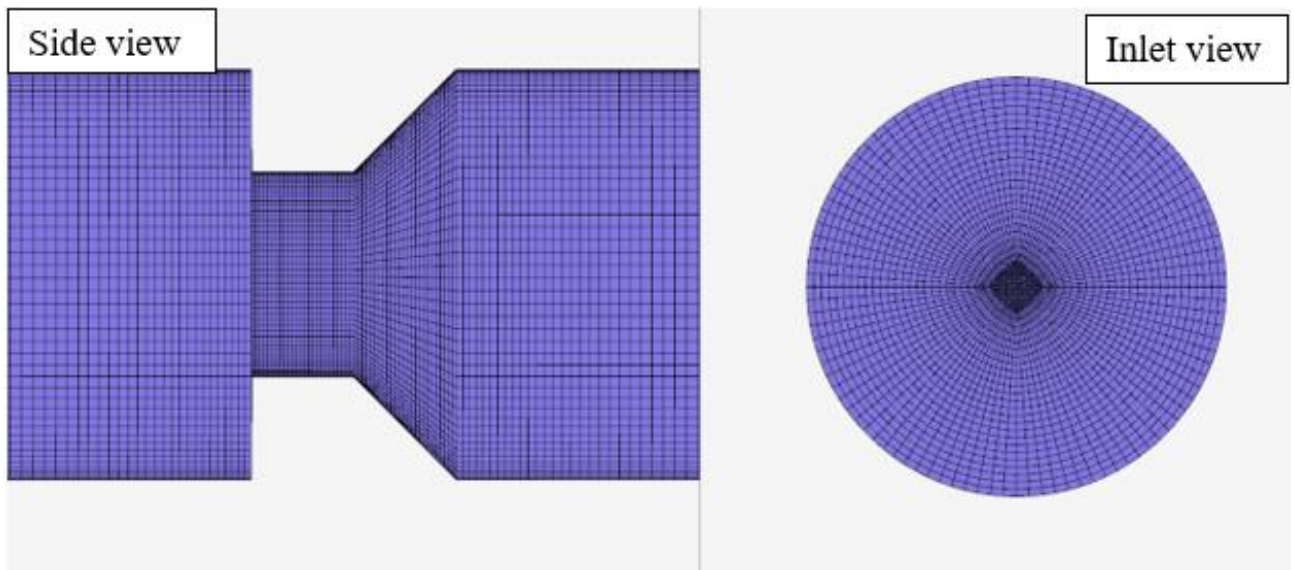


Figure 5.7 Mesh of the orifice with bevelled edges

Above is the geometry of a pipe with a different type of orifice. In this study, only t^* will be changed; the bevel angle will be constant. The main objective of this study is to compare the distribution of vortices after the sharp-edged orifice and illustrated in Figures 5.6 and 5.7.

As seen in Figure 5.8, the mesh is regular inside and the grid is divided with progression to the orifice and divided with regression after the orifice along the longitudinal axis. The orifice is fractioned sufficiently for more accurate data on velocity, pressure and vortices.

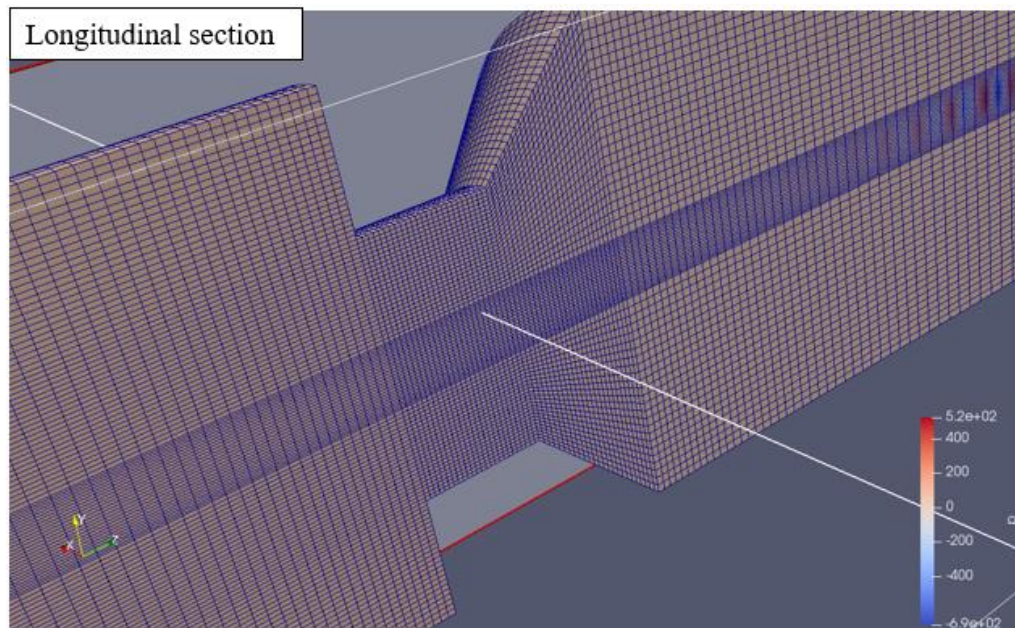


Figure 5.8 Internal body of the bevelled orifice mesh

As can be seen in Figure 4.12., after the value of 0.82, the graph line becomes gentler, this indicates that when grinding the mesh, the relative error almost does not change.

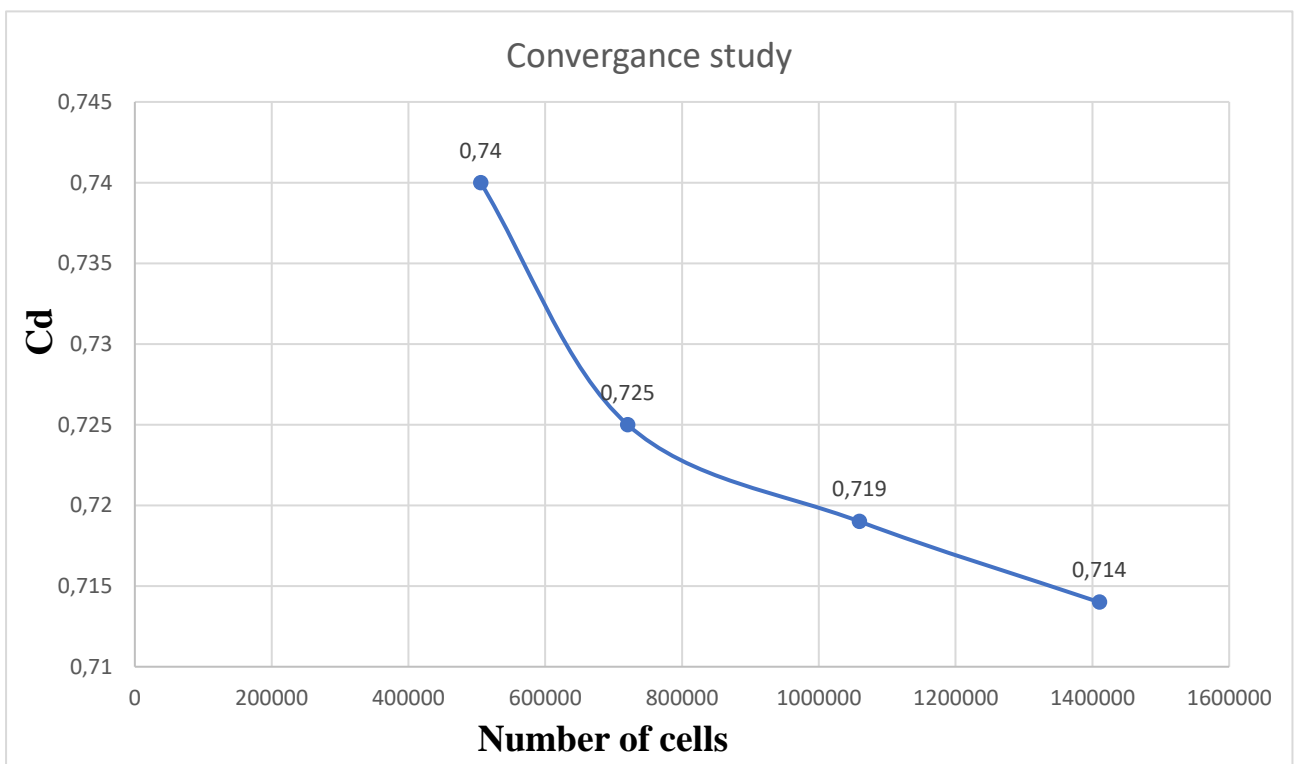


Figure 5.9 The dependence between C_d and different number of cells in the meshes

As Table 5.3 illustrates, the most appropriate mesh is Mesh №3 from optimal and accurate point of view. This mesh was selected for all simulations in this part.

Table 5.3 Convergence study for meshes of the sharp-edged orifice

	Number of cells	Cd	Relative error %
Mesh 1	505600	0,74	0
Mesh 2	720510	0,725	1,726
Mesh 3	1059600	0,719	0,828
Mesh 4	1410200	0,714	0,696

Table 5.4 Different characteristics of the orifice with back bevelled edges

Re	Pressure drop (MPa)	C _d
2500	15.39	0.698
4900	15.54	0.695
10000	15.67	0.692
40000	16.08	0.683
160000	16.45	0.675

5.1.7 Processing the received values. Differential pressure and coefficients of flow, distribution of pressures and speeds

The discharge coefficient depends on the differential pressure in the flow meter. The Tables 5.4 and 5.5 presents data on the pressure drop, the coefficient of flow at different Reynolds numbers.

Table 5.5 Different characteristics of the sharp-edged orifice

	Re	C _d	Pressure drop (MPa)
t [*] =1/4D	16	0.429	4.64
	36	0.632	1.87
	64	0.696	1.545
	100	0.731	1.4
t [*] =1/8D	16	0.415	4.34
	36	0.597	2.1
	64	0.660	1.17
	100	0.702	1.52
t [*] =1/12D	16	0.404	4.59
	36	0.584	2.19
	64	0.649	1.79
	100	0.692	1.56

Figure 5.10 shows the dependence of the efflux coefficient on different diaphragm geometry for different Reynolds numbers. Analyzing Figure 5.10, we can conclude that the smallest differential pressure in the diaphragm is $t^* = 1 / 4D$.

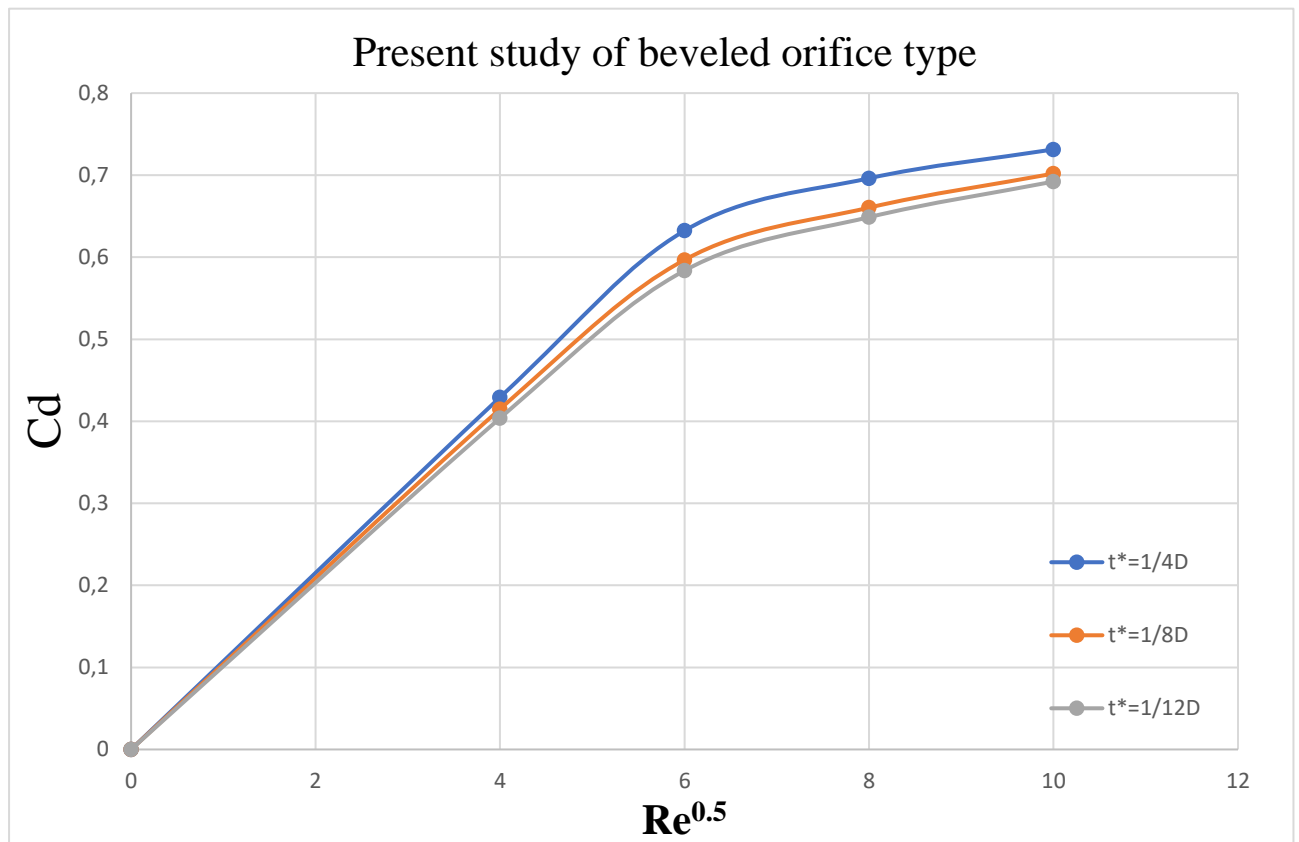


Figure 5.10 Present study of C_d in bevelled orifice type

Figure 5.11 shows a comparison of the upgraded flowmeter and the one used previously.

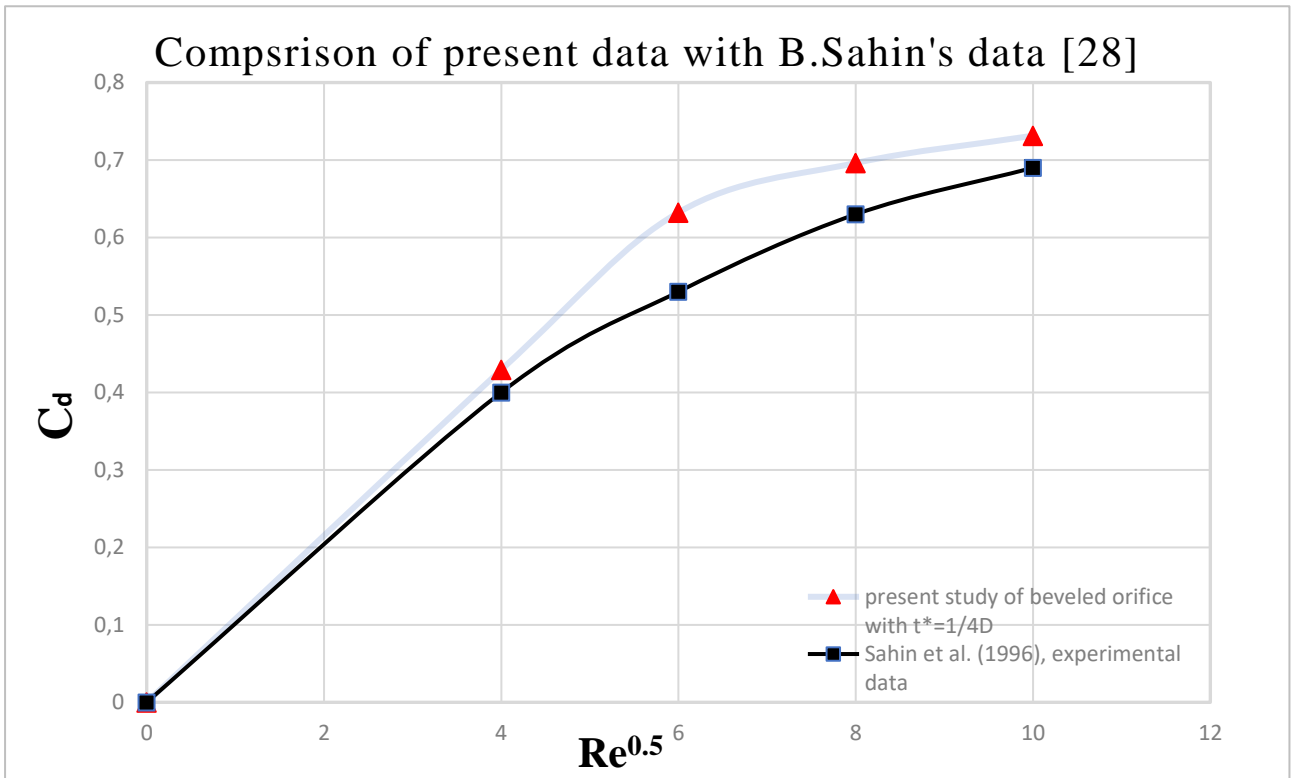


Figure 5.11 Experimental data in comparison with own results

The pressure and velocity distributions for a flowmeter with better geometry are shown below for clarity (see Figure 5.12, 5.13 and 5.14).

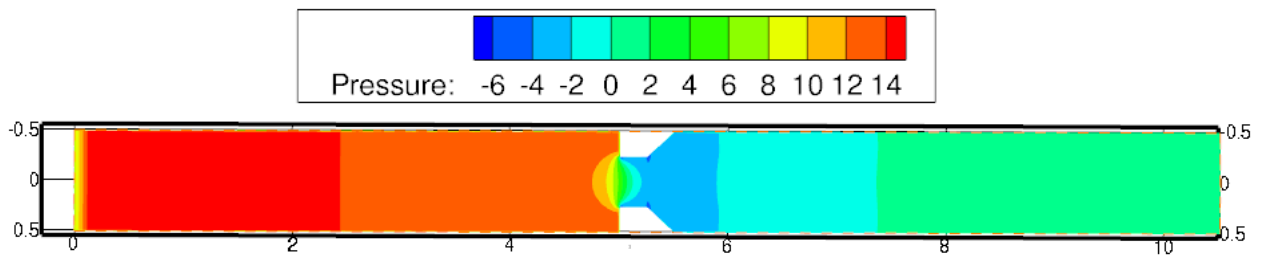


Figure 5.12 Pressure distribution through orifice with $t^*=1/4D$ (Pressure [m^2/s^2])

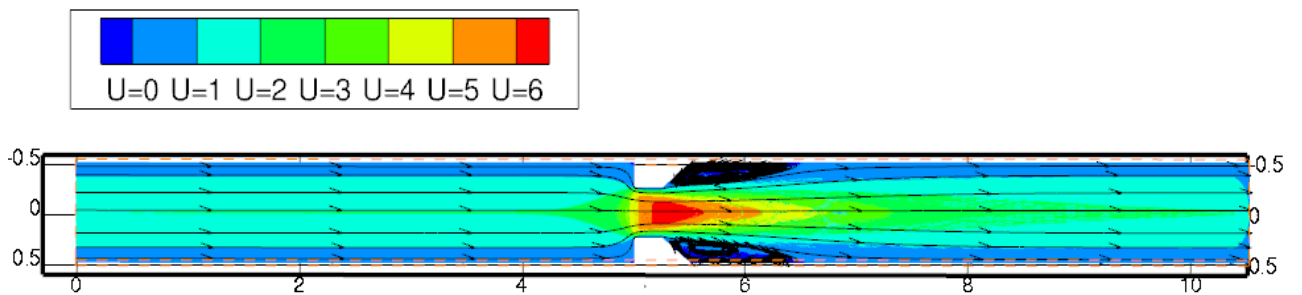


Figure 5.13 Velocity distribution through orifice with $t^*=1/4D$ and $Re=36(U [m/s])$

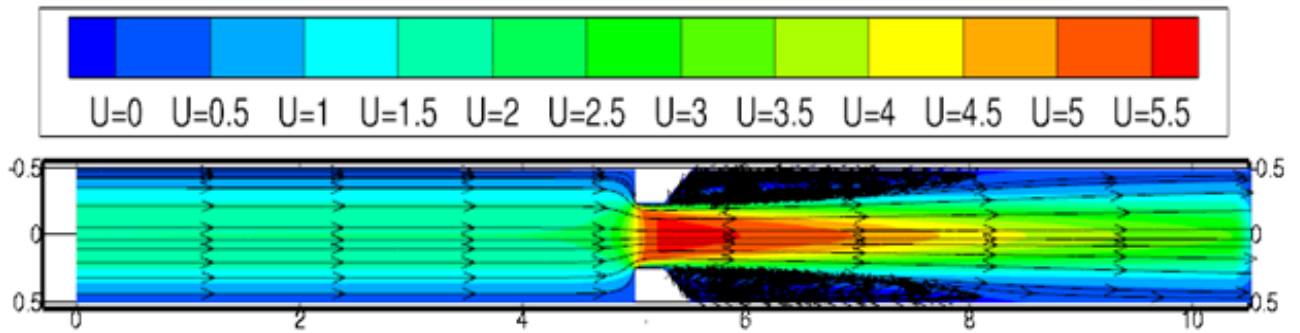


Figure 5.14 Velocity distribution through orifice with $t^*=1/4D$ and $Re=100$ (U [m/s])

Differential pressure flow meters are flow measuring devices. The principle of operation of flowmeters is based on measuring the potential energy of the flow (the static pressure of a substance flowing through a narrowing device in a pipeline).

When fluid flows through a diaphragm with sharp edges, the speed in the narrowed area increases compared to the flow rate before the narrowing. An increase in the velocity, and hence kinetic energy, causes a decrease in the potential energy of the flow in the narrowed section. In this case, the static pressure in the narrowed section will be less than in the section in front of the narrowing device. The only difference between these two flowmeters is that due to the beveled edges, the fluid flow slows down. If we compare two cases with the same Reynolds numbers, but with different t^* , the length of the zone with increased speed is less in the case of high t^* . The narrowing of the flow begins in front of the diaphragm. At a certain distance behind the diaphragm, the flow reaches its minimum size (like a flame from a turbine), expanding further to the full cross-section of the pipeline. Pressure beyond the diaphragm is not fully restored. In the corners of the interface between the diaphragm and the pipe wall, a zone is formed in which, due to the pressure difference, the reverse vortex movement of the liquid occurs - the secondary flow.

In conclusion, this flowmeter is almost as accurate as the acoustic meter used at Piltun-Astokhskaya-B. Also, the cost of this flow meter is much lower than the cost of its acoustic competitor; in addition, the service life of such a flow meter is much longer.

Compared to an ultrasonic flow meter, there is one drawback that should be mentioned. Pressure losses due to a tapering device force one to design and install a more powerful pump and, accordingly, spend more electricity. The appropriateness can only be estimated.

The main script used for computer modelling can be found in Appendix 1.

5.2. ESP

5.2.1 General information

The main goal of this section is to introduce import substitution of the pumping unit on the continental shelf. At present, the economy of the Russian Federation is going through difficult times, which is also reflected in the oil and gas industry. There are many ways to deal with the crisis and foreign sanctions. One of the main ones is own development technologies with their subsequent localization of production and implementation. The potential of the Russian continental shelf is enormous, especially in the Arctic. However, in order to successfully explore the Arctic, domestic companies are forced to work closely with foreign ones. In order to get rid of such dependence, it is necessary to develop technology to such an extent that there is no need for technology import. The ESP unit was taken as an example. In the framework of this thesis, it will be proved that at the moment in Russia there are developments and finished samples of centrifugal sediments, which can replace foreign analogues used in the conditions of the Piltun-Astokhskoye field. For this, a foreign pump will be presented, manual selection of a domestic analogue will be carried out, after which the economic feasibility of this project will be proved.

"Sakhalin Energy Investment Ltd." works closely with the Schlumberger company, which carries out the launch, installation, and maintenance of submersible centrifugal pumps.

Today, there are a huge number of domestic manufacturers of ESPs:

- "Almaz"
- "Borets"

- "Novomet"
- "Rimera Alnas"
- "BENZ"
- "Izhnefteplast"
- "New technologies"
- "RINPO"
- JSC "LEPSE"
- LLC "TatProm-Holding"

These companies produce centrifugal pumps for different operating conditions, for this, there are various modifications, for example: with a change in the shape of the blades, a corrosion-resistant, wear-resistant pump, and pumps with a two-wheeled impeller also belong to the modifications.

Currently, the largest producers of ESPs abroad are:

- "REDA" - USA
- "Centrilift"- USA
- "ESP" - USA
- "ODI" - USA

At the Piltun-Astokhskoye field, REDA pumps are used. The main advantage of American installations in comparison with domestic ones is the resistance of the cable and submersible motor insulation coating to high temperatures, this is justified at the Prirazlomnoye field, but not at Piltun-Astokhsky:

- The cable line consists of a KELTB LP extension cable ($t = 121^{\circ} - 232^{\circ}\text{C}$) + REDALEAD cable ($t = 203^{\circ} - 232^{\circ}\text{C}$). The KELTB LP extension cord and REDALEAD cable have a waterproof lead barrier that prevents the ingress of gas and

chemically active substances, thereby providing exceptional mode when working in hot, gassed and more aggressive wells.

- Submersible engine has a thermal range (121° - 150°C), that is, it can work in conditions when the temperature of the reservoir fluid rises to 150 ° C at a speed of 1 m/s.
- High efficiency of the gas separator.
- Better pump modes.
- More reliable hydro protection.
- High-quality oil poured into the cavity of the engine and tread.
- The use of depth pressure and temperature sensors such as PSI or DMT, which allow the company to determine the pressure above the pump inlet and the temperature of the reservoir fluid at a depth of the ESP suspension. A sensor mounted on the basis of an electric motor can record pressure from 0 to 340 atmospheres, temperature from 0 to 232 degrees Celsius.

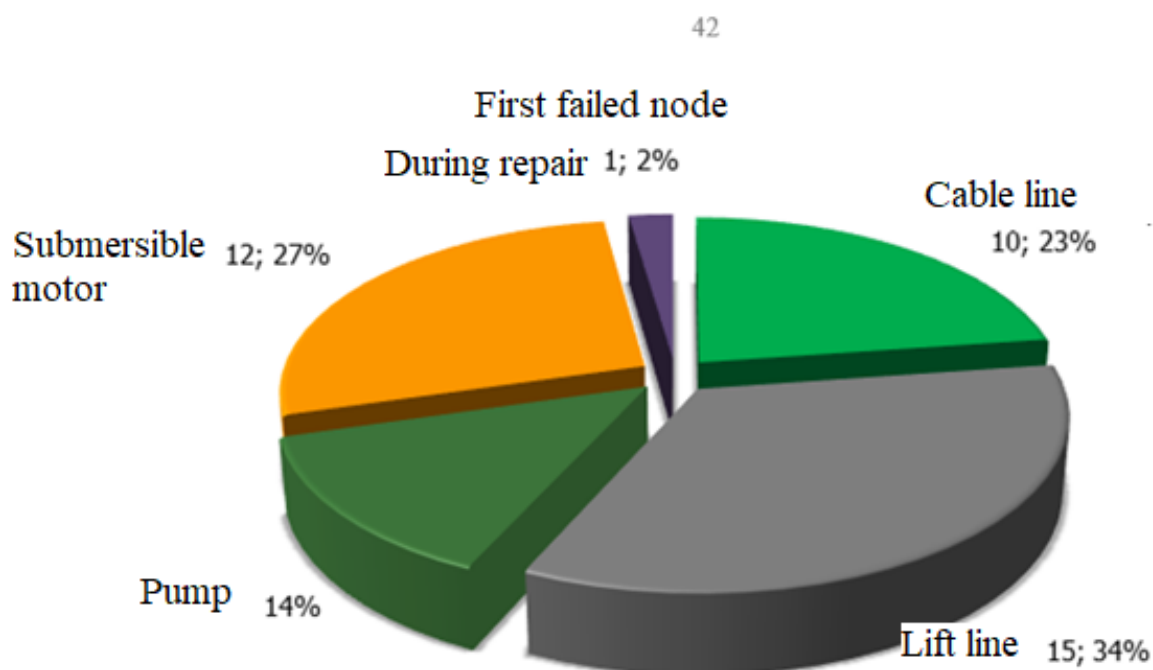
The main drawback of US-made ESPs is their high cost of 80-250 thousand US dollars, and the cost of repairing the pump is an order of magnitude higher than the cost of Russian ESPs.

The economic effect of the use of REDA installations consisted of:

1. reducing the number of repairs due to reliability, a wider range of the working area, which makes it possible to operate them in more severe conditions;
2. additional oil and gas production by eliminating well downtime while waiting for repairs.

However, over the past few years, the reliability of domestic pumps has increased significantly. This is evidenced by the experience of "RUSVIETPETRO", which uses both foreign and domestic units at the Khosedayu site. It should be noted that most

often the first failure is not the pump, but the submersible motor or cable line. This is shown in Figure 5.15.



First failed node	Amount	Operating time, days
Cable line	10	756
Lift line	15	566
Pump	6	757
Submersible motor	12	976
Repair	1	2106
Total	44	

Figure 5.15 Statistics of the first failures of the company "RUSVETPETRO" [30]

5.2.2 Manual selection of ESP

In order to replace the foreign pump with a domestic analogue, it is necessary to select a submersible electric pump, a submersible electric motor and a gas separator. Based on the data presented in Table 5.6 the standard size of the ESP installation will be determined, and all components will be selected.

Table 5.6 Initial data for manual selection of ESP [31]

№	Parameter	Value
1	Water density ρ_w , kg/ m ³	1015
2	Oil density ρ_o , kg/ m ³	850
3	Gas density ρ_g , kg/ m ³	1
4	Well flow rate Q , m ³ /day	530
5	Dynamic level H_{din} , m	1200
6	Depth of the reservoir H , m	1852
7	Formation pressure p_f , MPa	19
8	Saturation pressure p_{sat} , MPa	17
9	Buffer pressure p_{buf} , MPa	2,2
10	Annular pressure p_{an} , MPa	2,2
11	annular pressure T_f , °C	70
12	Temperature gradient G_m , °C/m	0,04
13	Water cut of formation XXII	0,25
14	Gas factor G , m ³ /m ³	85
15	Oil viscosity coefficient ν , m ² /s	0,85*10 ⁻⁶
16	Productivity coefficient K_{prod} , m ³ /MPa·day	185
17	Volumetric oil ratio B	0,85
18	Mechanical impurities, g/liter	0,1
19	Hydrogen sulfide and carbon dioxide	0,1
20	Diameter of production casing d_{prod} , mm	245x9

- 1) To determine the density of the mixture in the interval “bottom - pump inlet” in a simplified form, it is necessary to calculate the bottom hole pressure and volume fraction of free gas.

$$P_{bot} = P_f - \frac{Q}{K_{prod}} = 19 - \frac{530}{185} = 16,14 \text{ MPa} \quad (5.12)$$

$$\Gamma = \frac{P_{buf}G}{P_{bot}} = \frac{2,2 * 85}{16,14} = 11,59 \frac{m^3}{m^3} \quad (5.13)$$

$$\text{Percentage: } \frac{\Gamma}{100 - \Gamma} = \frac{11,59}{100 - 11,59} = 0,13 \quad (5.14)$$

The density of the mixture:

$$\begin{aligned} \rho_{mix} &= [\rho_w b + \rho_o(1 - b)](1 - \Gamma) + \rho_g \Gamma \\ &= [1015 * 0,25 + 850(0,75)](1 - 0,13) + 1 * 0,13 \\ &= 775,52 \text{ kg/m}^3 \end{aligned} \quad (5.15)$$

- 2) It is not necessary to calculate the depth of the dynamic level since this value is specified in the source data. Calculate the pressure at the pump inlet:

$$P_{in} = (1 - \Gamma)P_{sat} = (1 - 0,13) \cdot 17 = 14,79 \text{ MPa} \quad (5.16)$$

- 3) Calculating the depth of the pump suspension:

$$\begin{aligned} L &= H_{din} + \frac{P_{in}}{10 * \rho_{mix}g} = 1200 + \frac{14,79 \cdot 10^6}{10 * 775,52 \cdot 9,81} \\ &= 1394,4 \text{ m.} \end{aligned} \quad (5.17)$$

- 4) Calculating the temperature of the liquid at the pump inlet:

$$T = T_{for} - (H - L)G_m = 75 - (1852 - 1394,4) \cdot 0,04 = 56,7^\circ\text{C} \quad (5.18)$$

- 5) Determining the volumetric coefficient of the liquid at a pressure at the inlet to the pump:

$$\begin{aligned} B^* &= b + (1 - b)(1 + (B - 1) \sqrt{\frac{P_{in}}{P_{sat}}}) = \\ &= 0,25 + (1 - 0,25)(1 + (0,85 - 1) \sqrt{\frac{14,79}{17}}) = 0,89 \end{aligned} \quad (5.19)$$

- 6) Fluid flow rate at the pump inlet:

$$Q_{in} = QB^* = 530 * 0,89 = 471,7 \text{ m}^3/\text{day} \quad (5.20)$$

7) Calculating the volumetric amount of free gas at the inlet to the pump:

$$G_{in} = G \left(1 - \frac{P_{in}}{P_{sat}}\right) = 85 \cdot \left(1 - \frac{14,79}{17}\right) = 11,05 \quad (5.21)$$

8) Determining the gas content in the liquid at the inlet to the pump:

$$\beta_{in} = \frac{1}{\frac{(1 + in)B^*}{in} + 1} = \frac{1}{\frac{(1 + 14,79) \cdot 0,89}{11,05} + 1} = 0,44 \quad (5.22)$$

9) Gas flow rate at the pump inlet:

$$Q_{Gin} = \frac{Q_{in}\beta_{in}}{1 - \beta_{in}} = \frac{471,7 \cdot 0,44}{1 - 0,44} = 370,62 \text{ m}^3/\text{day} \quad (5.23)$$

10) The reduced gas velocity is calculated in the casing section at the pump inlet:

$$C = \frac{Q_{Gin}}{f_{well}} = \frac{370,62}{86400 \cdot 0,04} = 0,11 \text{ m/s} \quad (5.24)$$

where f_{well} – well cross-sectional area at the pump intake (5.25)

$$f_{well} = \frac{\pi(d_{prod} - 2s)^2}{4} = \frac{3,14 \cdot (245 - 2 \cdot 9)^2 \cdot 10^{-6}}{4} = 0,04 \text{ m}^2$$

11) True gas content at the pump inlet:

$$\varphi = \frac{\beta_{in}}{1 + \frac{C_n}{C}\beta_{in}} = \frac{0,44}{1 + \frac{0,02}{0,11} \cdot 0,44} = 0,41 \quad (5.26)$$

12) Gas power at the “face - pump inlet” section:

$$P_{g1} = P_{sat} \left(\frac{1}{1 - 0,4\varphi} - 1\right) = 17 \cdot \left(\frac{1}{1 - 0,4 \cdot 0,41} - 1\right) = 3,33 \text{ MPa} \quad (5.27)$$

13) The power of gas in the section "pumping the pump - wellhead":

$$P_{g2} = P_{sat} \left(\frac{1}{1 - 0,4\varphi_{buf}} - 1\right) \quad (5.28)$$

However, to calculate this power, it is necessary to calculate such parameters as: φ , β , B^* , G at buffer pressure. The calculation should be carried out.

$$G_{buf} = G \left(1 - \frac{P_{buf}}{P_{sat}}\right) = 85 \cdot \left(1 - \frac{2,2}{17}\right) = 74 \quad (5.29)$$

$$B_{buf}^* = b + (1 - b)(1 + (B - 1) \sqrt{\frac{P_{buf}}{P_{sat}}}) = \quad (5.30)$$

$$= 0,25 + (1 - 0,25)(1 + (0,85 - 1) \sqrt{\frac{2,2}{17}}) = 0,96$$

$$\beta_{buf} = \frac{1}{\frac{(1 + P_{buf})B_{buf}^*}{G_{buf}} + 1} = \frac{1}{\frac{(1 + 2,2) \cdot 0,96}{74} + 1} = 0,96 \quad (5.31)$$

$$\varphi_{buf} = \frac{\beta_{buf}}{1 + \frac{C_n}{C} \beta_{buf}} = \frac{0,96}{1 + \frac{0,02}{0,11} \cdot 0,96} = 0,81 \quad (5.32)$$

Now, by the formula (5.28), the power can be calculated:

$$P_{g2} = 17 \cdot \left(\frac{1}{1 - 0,4 \cdot 0,81} - 1\right) = 8,15 \text{ MPa} \quad (5.33)$$

14) Pressure required by the pump:

$$P = \rho_{mix} g H_{din} - P_{buf} - P_{g1} - P_{g2} = \quad (5.34)$$

$$= 775,52 \cdot 9,81 \cdot 1200 - (2,2 - 3,33 - 8,15) \cdot 10^6 = 18,1 \text{ MPa}$$

15) Based on the data obtained, the pump ESP5A-600-1350 is selected from the equipment catalog of the “BORETS” manufacturing company [32]. The values of flow are determined, pressure and power at the optimum mode, as well as at zero flow using the graphical characteristics of the pump shown in Figure 5.16.

The optimal pump should contain 273 stages and have the head of 1350 m.

At zero flow rate:

- Power consumption - 300 W
- Head - 1638m
- Efficiency - 0%

At the optimum mode (Q = 600 m³/day):

- Power consumption - 495 WT
- Head - 1350 m
- Efficiency - 68%

Characteristics of the ESP-600 Pump
Speed $n = 2910$ rpm. The number of steps $m = 1$.

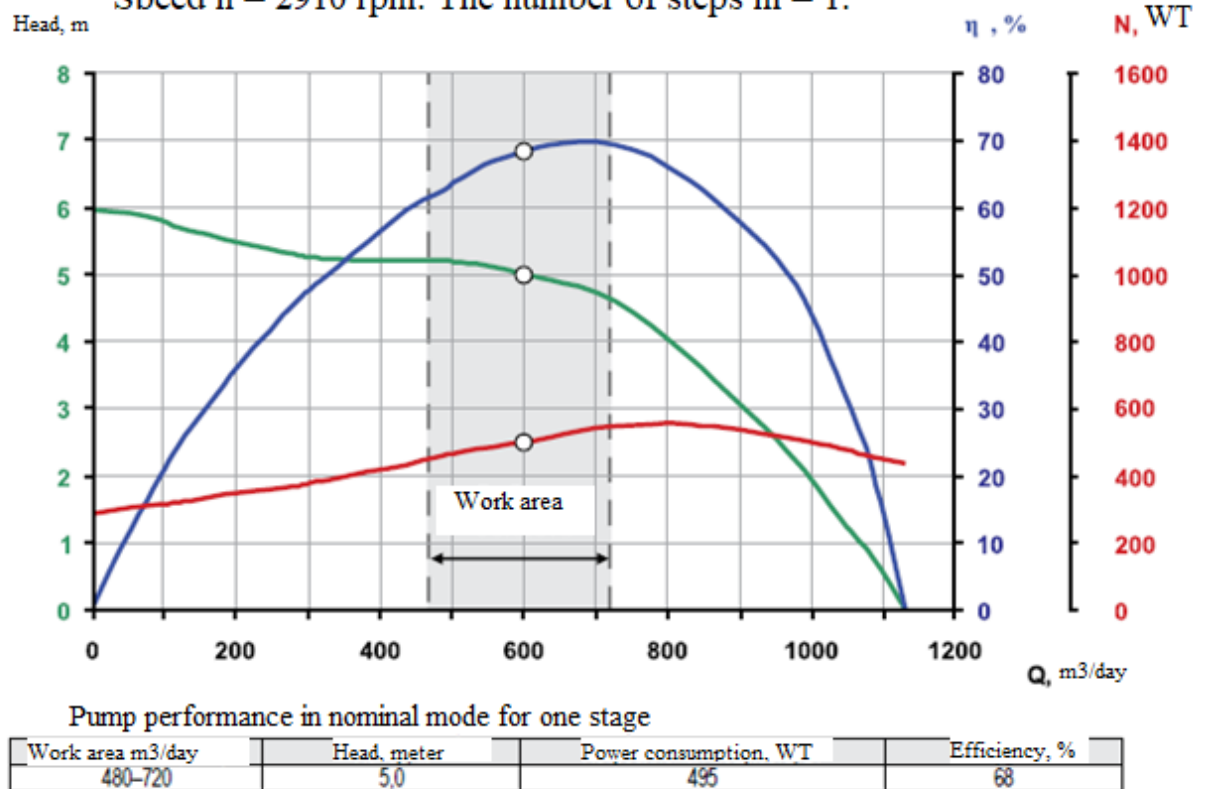


Figure 5.16 Characteristics of the ESP-600-1350 [32]

- 16) The coefficient of change in the pump flow when working on oil-gas mixture relative to the water characteristics:

$$K_{Qv} = 1 - 4,95 \nu^{0,85} \cdot Q_{oB}^{-0,57} = \quad (5.35)$$

$$1 - 4,95 \cdot (0,8 \cdot 10^{-5})^{0,85} \cdot \left(\frac{600}{86400}\right)^{-0,57} = 0,996$$

- 17) The coefficient of change in the efficiency of the pump due to the viscosity influence:

$$K_{\eta v} = 1 - 1,95 \frac{\nu^{0,4}}{Q_{oB}^{0,27}} = 1 - 1,95 \cdot \frac{(0,8 \cdot 10^{-6})^{0,4}}{(600/86400)^{0,27}} = 0,97 \quad (5.36)$$

- 18) Pump gas separation coefficient:

$$K_c = \frac{1}{1 + (0,11 \frac{Q_{in}}{f_{well}})} = \frac{1}{1 + (0,11 \cdot \frac{471,7}{86400 \cdot 0,032})} = 0,982 \quad (5.38)$$

Where f_{well} – The area of the ring formed by the inner wall of the casing and the pump casing (5.37)

$$f_{well} = \frac{\pi}{4} ((d_{prod} - 2s)^2 - d_{pump}^2)$$

$$= \frac{3,14}{4} ((245 - 2 \cdot 9)^2 - 103^2) \cdot 10^{-6} = 0,032 \text{ m}^2$$

19) Relative fluid rate at the inlet to pump:

$$q = \frac{Q_{in}}{Q_{oB}} = \frac{471,7}{600} = 0,78 \quad (5.39)$$

20) Relative flow rate at the inlet to the pump at the corresponding point of the pump water characteristic:

$$q_{in} = \frac{Q_{in}}{Q_{oB} K_{Qv}} = \frac{474,7}{600 \cdot 0,996} = 0,79 \quad (5.40)$$

21) The gas content at the pump inlet, taking into account gas separation:

$$\beta_{in1} = \beta_{in} (1 - K_c) = 0,44 \cdot (1 - 0,982) = 7,92 \cdot 10^{-3} \quad (5.41)$$

22) The coefficient of change of the pump head due to the influence of viscosity:

$$K_{Hv} = \left| 1 - (1,07 v^{0,6} \frac{q_{in}}{Q_{oB}^{0,57}}) \right| \quad (5.42)$$

$$= \left| 1 - (1,07 \cdot (0,85 \cdot 10^{-6})^{0,6} \cdot \frac{474,7}{(600/86400)^{0,57}}) \right| = 0,97$$

23) The coefficient of pump head changing, taking into account the influence of gas:

$$K = \frac{1 - \beta_{in1}}{(0,85 - 0,31 q_{in})^A} = 0,951 \quad (5.43)$$

$A = 0,02$, empirical coefficient [29].

24) Pump head on water at optimum mode:

$$H = \frac{0,685P}{\rho g K K_{Hv}} = \frac{12,4 \cdot 10^6}{1000 \cdot 9,81 \cdot 0,951 \cdot 0,979} = 1357,5 \text{ m} \quad (5.44)$$

25) Required pump stages:

$$Z = \frac{H}{h_{st}} = \frac{1357,5}{5} = 271 \quad (5.45)$$

26) Pump efficiency taking into account the viscosity influence, free gas and operating mode:

$$\eta = K_{\eta v} K_c \eta_{oB} = 0,97 \cdot 0,982 \cdot 0,68 = 0,65 \quad (5.46)$$

27) Pump power:

$$N = \frac{PQ_{in}}{\eta} = \frac{18,1 \cdot 10^6 \cdot 474,7}{86400 \cdot 0,65} = 152,99 \text{ kWT} \quad (5.47)$$

28) Power of a submersible electric motor, taking the approximate efficiency of a SEM with an external diameter of 117 mm:

$$N_{SEM} = \frac{N}{\eta_{SEM}} = \frac{152,99 \cdot 10^3}{0,845} = 186,4 \text{ kWT} \quad (5.48)$$

29) Check the pump for heavy fluid:

$$P_{kill} = \rho_{kill} g L + P_{buf} + P_{bot} - P_f = 1200 \cdot 9,81 \cdot 1400 + (2,2 + 16,14 - 19) \cdot 10^6 = 16,08 \text{ MPa} \quad (5.49)$$

Where ρ_{kill} is a kill fluid density

30) Pump head during well completion:

$$H_{kill} = \frac{P_{kill}}{\rho_{kill} g} = \frac{16,08 \cdot 10^6}{1200 \cdot 9,81} = 1365,95 \text{ m} \quad (5.50)$$

31) Pump power during well completion:

$$N_{kill} = P_{kill} \frac{Q}{\eta} = 16,08 \cdot 10^6 \cdot \frac{500}{86400 \cdot 0,65} = 143,16 \text{ kWT} \quad (5.51)$$

32) Power consumed by SEM during well completion:

$$N_{SEMkill} = \frac{N_{kill}}{\eta_{SEM}} = \frac{143,16 \cdot 10^3}{0,85} = 169,42 \text{ kWT} \quad (5.52)$$

Based on the power consumed by the SEM during the well completion, as well as the power of the SEM during the production of formation fluid, we select the next submersible electric motor EDBS200-117V5.

5.2.3 Technical comparison of used and proposed pumps

Table 5.7 Submersible Pump Analysis

	ESP5A-600-1350 50 Hz	REDA GN4000 50Hz
Power, 1 stage (WT)	495	588
Head, 1 stage (m)	5	6,3
Efficiency (%)	68	67
Number of stages	271	220
Assembly weight (kg)	1230	1034
Pump diameter (mm)	103	130
SEM power (kWT)	200	210 (562 Series Motor)
Assembly Length (m)	27	16,6

Based on the Table. 5.7., it is possible to conclude that the submersible pumps are equal to each other. However, the domestic pump consumes less energy, has a larger effective annular space. The disadvantages of the domestic pump include a significant weight and a large number of stages. It should be taken into account that the impeller installed in the REDA pump has a more complex geometry and profile, which significantly increases the layout cost, and also reduces MTBF (Mean time between failures).

5.3 Calculation of ice load on the "platform substructures ("PA-B"), analysis of existing methods

Chapter 2 mentioned such a method of destruction of an ice mass as the effect of a bending moment. It is necessary to design an inclined surface in order to create bending stress, then the ice, due to its mass will move up or down the inclined surface. At the moment, when the ice moves from the surface of the water to such a substructure, a force arises, which forms a bending moment. This principle is clearly shown in Figure 5.17.

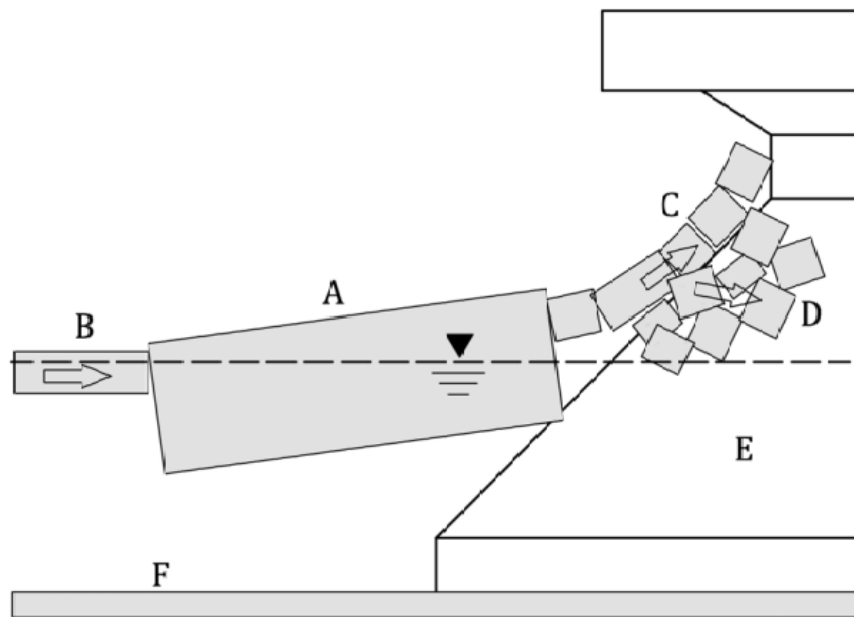


Figure 5.17 The inclined barrier that destroys the ice mass [12], where A is the ice mass, B is the direction of the mass movement, C is the ice fragments on the barrier, D is the ice fragments that flow around the structure after crushing, E is the conical type barrier, F is sea bottom

The PA-B platform uses a metal belt (see Figure 2.5), which destroys ice, but this belt undergoes higher loads than a cone-shaped plane, so a concept with three conical supports was proposed. These supports differ in the angle of inclination. The horizontal force acting on the structure will be calculated, after which the best calculation method and the substructure concept will be selected as a priority. Calculation Methods:

1. 3D model of Crosdale for conical structures [33];
2. SP 38.13330.2012. Loads and impacts on hydraulic structures. Ice impact on a conical structure [34].

In Figures 5.18, 5.19 and 5.20, the concepts of concrete substructure for "PA-B" are presented.

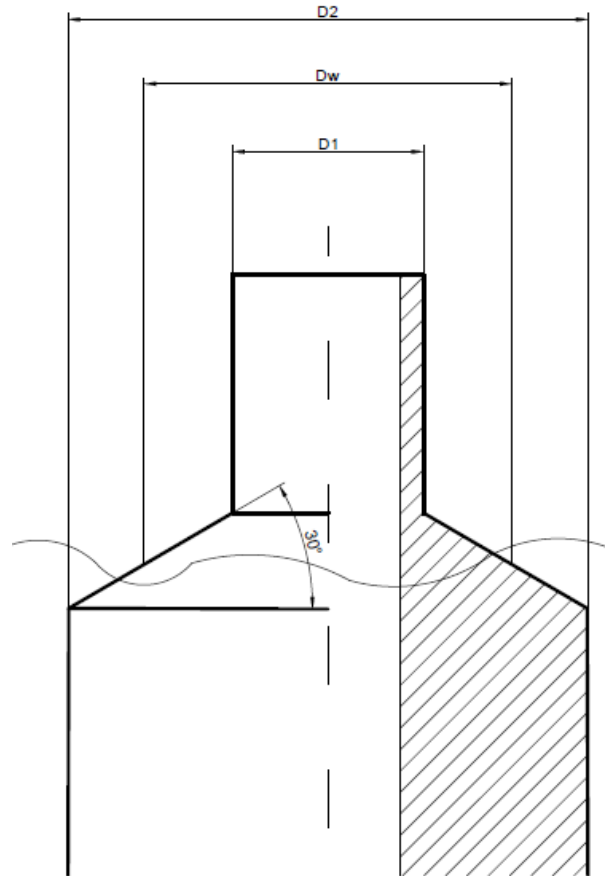


Figure 5.18 The substructure with an angle of inclination of 30° from the horizontal, where D_1 is the diameter of the upper part of the support, D_2 is the diameter of the lower part of the support, D_w is the diameter of the support at the point of contact with the water surface

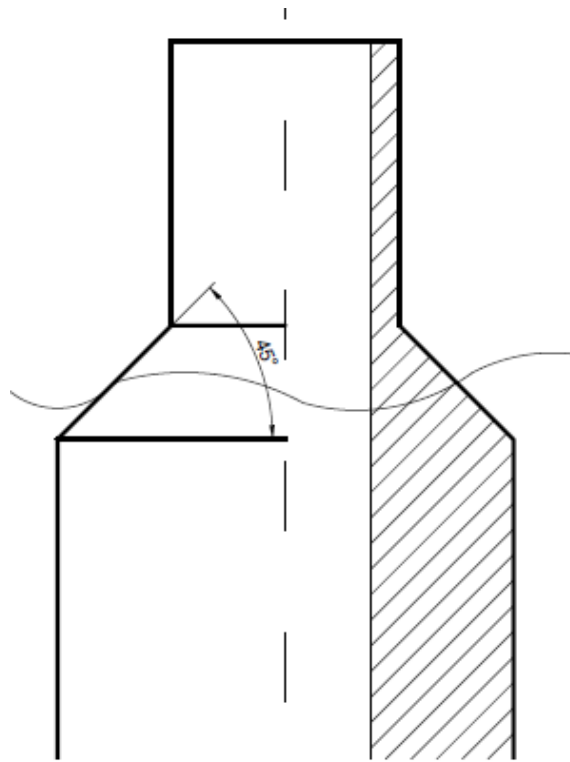


Figure 5.19 The substructure with an angle of inclination from the horizontal of 45°

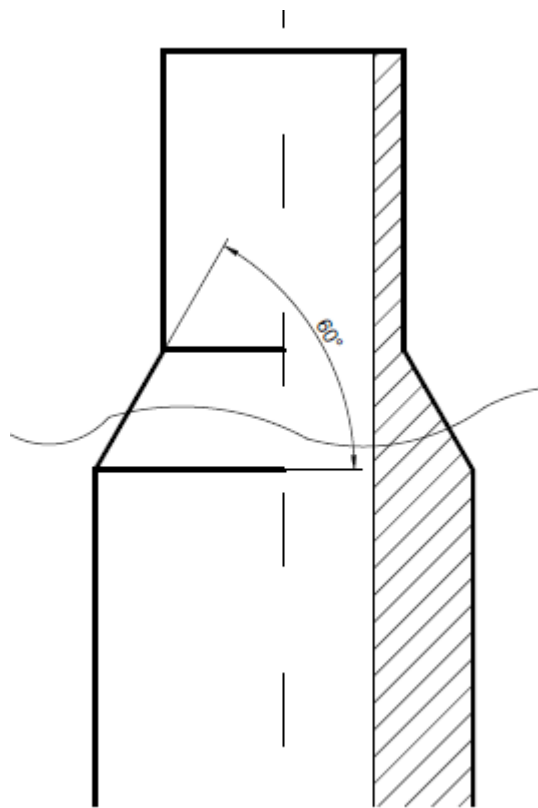


Figure 5.20 The substructure with an angle of inclination from the horizontal of 60°

5.3.1 Calculation of horizontal ice load according to the 3D model of Crosdale

$$F_H = C_1 * D_w * R_f * \left(\frac{\rho_w * g * h_{max}^5}{E} \right)^{0.25} * \left(1 + \frac{\frac{\pi^2}{4}}{\frac{l}{D_w}} \right) + C_2 * z * h_{max} * \rho_{ice} * g * D_w \quad (5.53)$$

$$l = \frac{E * h_{max}^3}{12 * \rho_w * g * (1 - \mu^2)} \quad (5.54)$$

$$C_1 = 0.68 * \frac{\sin \alpha + \mu * \cos \alpha}{\cos \alpha - \mu * \sin \alpha} \quad (5.55)$$

$$C_2 = (\sin \alpha + \mu * \cos \alpha) * \left(\frac{\sin \alpha + \mu * \cos \alpha}{\cos \alpha - \mu * \sin \alpha} + \frac{\cos \alpha}{\sin \alpha} \right) \quad (5.56)$$

Table 5.8 Initial and calculated values for three conical structures

Parameter	Units	Values
Initial data		
ρ_w density of water	[kg/m ³]	1025
ρ_{ice} density of ice	[kg/m ³]	900
R_f flexural strength of ice	[MPa]	1.52 [34]
z height of ice debris accumulation above the surface of the water	[m]	5[35]
g gravitational constant	[m/s ²]	9.81
α cone angle	[degree]	60; 45; 30
μ Poisson's ratio	[-]	0.3
D_w waterline surface diameter	[m]	28.6 [35]
h_{max} maximum ice thickness noted in this area	[m]	1.9 [4]
E Young's modulus for ice	GPa	3 [33]
Calculated data		
l characteristic length of the ice massif	[m]	21.49
C_1 characteristic coefficient	[-]	2.8764; 1.2629; 0.721
C_2 characteristic coefficient	[-]	4.8844; 2.6264; 2.1235

$\sin \alpha$	[-]	0.866; 0.707; 0.5
$\cos \alpha$	[-]	0.5; 0.707; 0.867
F_H horizontal ice load	[MN]	45.76; 21.25; 13.62

As reflected in the Table. 5.8, the maximum horizontal force acting on the substructure of a conical shape occurs when the angle of inclination of the conical surface from the horizontal is 60 °. However, it should be borne in mind that part of the load goes into the vertical. Using this calculation method, it is not possible to evaluate the vertical axial load.

5.3.2 Calculation of horizontal ice load according to SP 38.13330.2012

The vertical and horizontal load from the action of a moving ice massif on separate conical support or conical ice cutter of a semicircular shape (Figure 5.21) in the absence of freezing with ice must be determined by the formulas:

$$F_H = [k_{h,1} * k_{v,f} * R_f * h_{\max}^2 + 10^{-6} * k_{h,2} * \rho_w * g * h_{\max} * D_w^2 + 10^{-6} * k_{h,3} * \rho_w * g * h_{\max} * (D_w^2 - D_1^2)] * k_{h,4} \quad (5.57)$$

$$F_V = k_{v,1} * F_H + 10^{-6} k_{v,2} * \rho_w * g * h_{\max} * (D_w^2 - D_1^2) \quad (5.58)$$

Table 5.9 Initial and calculated values for three conical structures

Initial data		
$k_{h,1}; k_{h,2}$	[-]	1.6; 0.31 [34]
β cone angle	[degree]	60; 45; 30
$k_{h,3}$ characteristic coefficient	[-]	0.46; 0.33; 0.27 [34]
$k_{h,4}$ characteristic coefficient	[-]	2.6; 1.5; 0.9
R_f flexural strength of ice	[MPa]	1.52 [34]
$k_{v,1}$ characteristic coefficient	[-]	0.5; 0.95; 1.6
$k_{v,2}$ characteristic coefficient	[-]	0.026; 0.037; 0.042
D_1 diameter of the upper part of the support	[m]	24 [35]
Calculated data		
F_H horizontal ice load	[MN]	63.77; 35.89; 22.08

F_v vertical ice load	[MN]	32; 34.27; 35.52
-------------------------	------	------------------

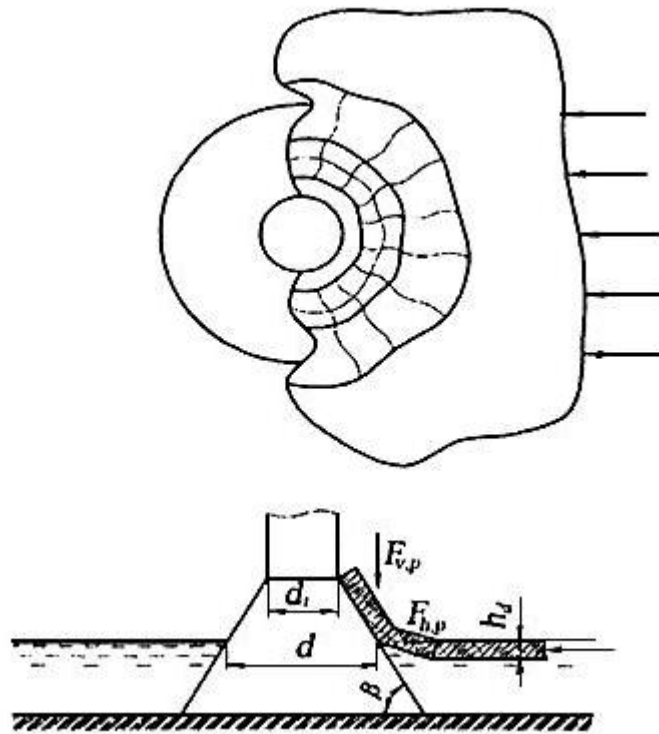


Figure 5.21 Scheme of application of loads from the ice mass to the substructure with a conical surface [34]

As can be seen in the Table. 5.9, the horizontal load from the ice massif has the same tendency to decrease with a decrease in the angle of inclination, as in the first method. The vertical load, in contrast, increases with a decrease in the angle of inclination of the surface. However, the total force is less precisely at an angle of 30 degrees.

Both methods for calculating ice loads acting on a structure are based on various approaches. It is difficult enough to draw an unambiguous conclusion about the superiority of a particular method over another.

In addition to the two proposed methods of calculation, there are several more domestic and foreign approaches to calculation. For example, ISO 19906: 2010 (E) [12]. Many researchers and even companies use this technique to calculate the loads on a conical structure. However, this is a mistake. In this standard, there is a formula for global ice load, it includes the component “d”, which indicates the width of the support structure

along with the ice contact. Since in the case of a conical surface, it is practically impossible to establish the width of the contact of ice with the surface, the diameter of the upper part of the support, or the diameter along the waterline, is used. Due to such assumptions, the value obtained after the calculation according to this formula is greatly underestimated, and therefore, it is not worth using this standard for such calculations.

The Crosdale method involves the interaction of an ice massif with a structure while piling ice debris on an inclined surface. The load on the inclined structure is not reduced due to the unconsolidated ice mass. According to the methodology, an unconsolidated ice mass will create a higher pile of ice debris on the surface than even ice of the same thickness. It leads to an increase in the axial load.

The method of SP 38.13330.2012 involves dividing the ice massif into layers with different temperatures. It affects the value of the strength of ice for uniaxial compression. Also, this technique takes into account the type of crystalline structure of ice, which can be granular or fibrous. The technique allows engineers to take into account the drift speed of the ice massif in the direction of the structure, in contrast to foreign counterparts. The only minus of this technique is that the accumulation of ice debris on the surface of the structure is not taken into account in any way. However, it should be noted that due to its taper, the surface is almost not piled with blocks and ice fragments, since they roll down from the inclined surface around the periphery under their own weight into water, reducing the global bearing load.

The horizontal load values differ by no more than 40%. Based on the foregoing, the optimal solution would be to use the second calculation method and a conical surface with a slope of 30 degrees. For any new platforms in the area, the above considerations should be taken into account.

Chapter 6. Feasibility study and environmental safety measures in the Piltun area

6.1. Feasibility study on the choice of flow meter and ESP replacement

Table 6.1 Analysis of the economic feasibility of replacing the used flow meter

Parameter	Differential pressure meter	Acoustic flow meter
Accuracy	95%	97%
Life time	25-30 years [36]	5-7 years [36]
Cost	450000 rub [36]	700000 rub [36]
Annual Maintenance Cost	15000 rub [36]	120000 rub [36]
The cost of restoring lost pressure in the oil pipeline	122640 rub в год	0
Costs per year	154003 rub	236666 rub
Total for the next 25 years of the project	3850075 rub	5916650 rub

Based on table 6.1, it follows that a differential pressure flow meter is more preferred in comparison with an acoustic. Firstly, a submersible pump of another modification will be installed in the well, which has a larger head, which means a longer resource for increasing production. Secondly, by choosing the proposed concept, it will be possible to reduce operating and capital costs by almost 2 million rubles.

Table 6.2 Analysis of the economic feasibility of replacing the used ESP

Parameter	ESP5A-600-1350 50 Hz	REDA GN4000 50Hz
Submersible pump and SEM cost	8400000 rub	17500000 rub
Annual Maintenance Cost	6000000 rub	8500000 rub
Cost of electricity consumed per year	876000 rub	919800 rub
Average life to failure in the Sakhalin shelf	1,5 years	2 years
Costs per year	12,48 millions rub	18,17 millions rub
Total for the next 25 years of the project	312 millions rub	454,25 millions rub

Based on the table above, domestic ESP is preferable from an economic point of view. However, it is difficult to estimate the time between failures and maintainability of the unit. Since this indicator can affect the final economic feasibility, a competitive map will be built based on the criteria that will be assigned points.

Table 6.3 Competitiveness map

Criteria for evaluation	Criterion weight	Points		Competitiveness	
		P _B	P _R	K _B	K _R
Technical criteria for evaluating resource efficiency					
1. Improving user productivity	0,07	3	4	0,21	0,28
2. Ease of use	0,11	4	4	0,44	0,44
3. Энергоэкономичность	0,14	5	3	0,7	0,42
4. Reliability	0,15	2	3	0,3	0,45
5. Safety	0,08	3	3	0,24	0,24
Criteria for the economic component of the project, as well as import substitution					
6. Competitiveness	0,05	5	3	0,25	0,15
7. Penetration rate on the Russian market	0,09	3	1	0,27	0,09
8. Cost	0,05	4	2	0,2	0,1
9. Estimated Lifetime	0,07	3	4	0,21	0,28
10. Import substitution	0,19	4	0	0,76	0
Total	1	36	27	3,58	2,45

Where P_B is the points given by experts for the pump of the "BORETS" company, and P_R - of the "REDA" company, the rating was set on a five-point scale from 1 to 5, where one is the weakest and five is the strongest. Experts also determined the weights of the indicators and the criteria themselves; the total weight should be 1. Further analysis of the competitiveness of KB and KR was determined by the formula:

$$K = \sum W_i * B_i \quad (6.1)$$

where K is the competitiveness of the ESP, W_i is the weight of the indicator (in fractions of a unit), B_i is the score of the i-th indicator.

In conclusion, the domestic pump received a total score of 3.58. This is 46% better than that of the foreign counterpart, therefore, it is worth giving preference to the domestic ESP according to the totality of estimates.

6.2. Environmental precautions in the Piltun area

The depth of the sea at the platform installation site is just over 30 m. The minimum distance from the platform to the coast of Sakhalin is 13 km. The nearest settlements are the villages of Tungor and Chayvo, located 80 km to the north-west and 55 km to the south-west of the platform, respectively. On the coast in a zone 1 km wide from the border of the sea there are no beaches, gardens, holiday homes. The considered region of the Sea of Okhotsk belongs to the territorial sea of the Russian Federation, adjoins the Okha and Nogliki districts of the Sakhalin Region and is a water body used for fisheries.

The characteristics of hydrochemical conditions and pollution of sea waters are presented based on materials of local environmental monitoring. It was carried out in autumn 2016 in the area of the PA-A platform in order to timely identify possible effects and predict the development of processes that affect the quality of sea waters, bottom sediments and the state of biological objects.

At all 11 stations located at a distance of 250, 1,000, and 10,000 m from the platform, seawater was sampled in the surface horizon to analyze standard hydrochemical indicators and pollutants: suspended solids, the total content of petroleum hydrocarbons, surfactants, phenols. Regular monitoring of the state of bottom sediments in the area of the PA-A platform should be carried out as part of the relevant programs of local environmental monitoring and industrial environmental control. It is necessary to control the total content of petroleum hydrocarbons, polycyclic aromatic hydrocarbons (PAHs), alkyl hydrocarbons (n-alkanes), metals, phenols.

When it comes to the development of an offshore field, the phrase “environmental safety” should be at the head of everything. However, even observing all environmental protection rules and including them in the field development project, the negative

impact cannot be completely ruled out. Firstly, any hydrocarbon production process is associated with a violation of the integrity of the subsoil, which can lead to terrible consequences. Secondly, there are a lot of environmental impacts. These impacts are not directly related to the violation of the integrity of the subsoil when drilling wells.

Exposure may be single or continuous. A single exposure is the spill of oil from an oil tanker into water. Such an impact could be avoided without violating safety precautions, paying attention to weather conditions and proper qualification of the crew of the vessel and platform. Some impacts are impossible to avoid. For example, the most severe storm or earthquake in history, as a result of this is a violation of the integrity of the structure with possible oil spills. Permanent impacts include emissions of pollutants into the atmosphere: chimneys and exhaust pipes of technological and power plants, ventilation mouths, breathing pipes and valves, gas cutting of metals. Even helicopters taking off or landing have a negative impact on the environment. Some of these emissions can also be avoided, for example, by not flaring associated gas in a flare, but using it for transportation to land or for own purposes to generate electricity in a gas turbine.

Measures necessary to reduce the harmful effects on the environment:

1. the use of sealed and resealable containers for sludge;
2. the use of technical means to prevent the bottling of drilling waste or its components in the process of accumulation and preparation of the injected pack;
3. the use of vessels with certificates of compliance with environmental safety techniques;
4. compliance with the rules of operation of ship installations during mooring and parking, as well as a possible reduction in the time of loading/unloading of vessels
5. continuous monitoring of the state of the air using gas analyzers.

Activities necessary to ensure acoustic and vibration safety:

1. installation of basic equipment on foundations that exclude resonance phenomena;

2. compliance with the technological process and equipment operating rules provided for by normative and technical documentation;

3. use of personal protective equipment if necessary.

Measures to protect the wildlife of the Okhotsk region:

1. In order to compensate for the damage to the fauna that is not preventable by preventive measures, artificial reproduction and release of valuable fish species into the water area adjacent to the work area is assumed;

2. reduction of industrial noise, which has a harmful effect on marine mammals;

3. the choice of the routes of ships and helicopters, with the advent of marine mammals, there should be a clear set of rules of conduct for the crew, regulations for the work and maneuvering of vessels;

4. helicopter routes should be laid at the height of at least 500 meters to reduce noise impact on mammals, and helicopter and ship routes should take into account the distribution of grey whales in the Sea of Okhotsk in order to minimize contact with them;

5. The exception is the case of poaching among workers.

Below (Figure 6.1) is a chart (bow-tie diagram) that shows a risk analysis for one key event. In this case, an oil spill or gas leak. The first column on the left shows the possible causes of the critical event. The second column displays protective measures to prevent the situation with spills and leaks. On the right side, in the fourth column, a part of the possible consequences is mentioned, in the third column - the measures applied in case of the occurrence of a particular consequence.

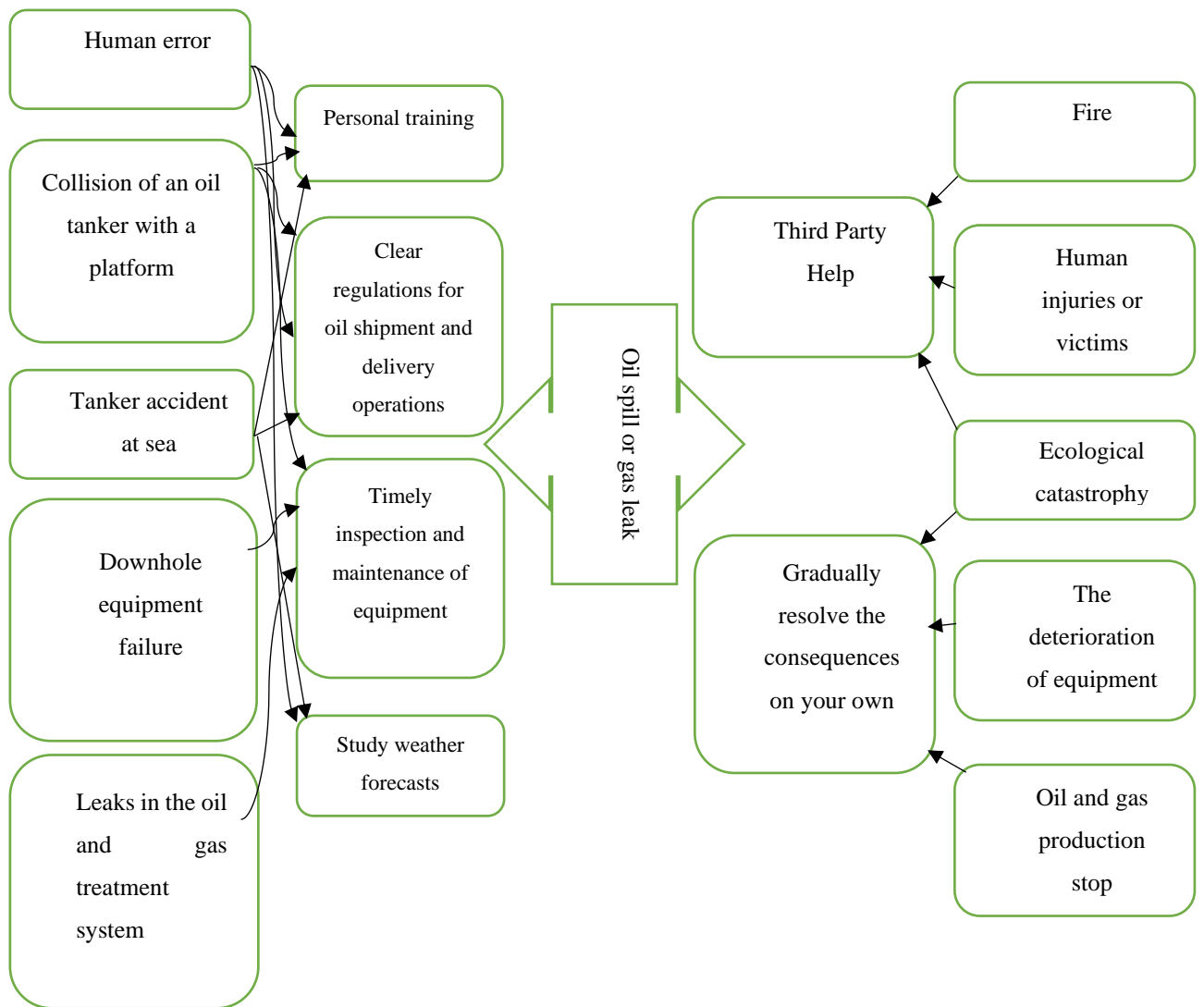


Figure 6.1 Bow-tie diagram for environmental protection

Thus, while developing the concept of field development, it is necessary to analyze and model all kinds of accidents and malfunctions, their causes, consequences and control measures.

Conclusion

As part of this thesis, solutions were proposed that contribute to the development of the Piltun-Astokhskoye field, taking into account the quality of the equipment, its manufacturability and reliability. These include replacing the acoustic flowmeter with a differential pressure flowmeter, followed by modernization, as well as replacing the foreign submersible electric centrifugal installation with a domestic one. In addition to the above, measures were proposed to protect the wildlife and the environment of the Piltun region. The risk analysis diagram was developed and compiled using a specific example.

In order to replace and upgrade the flowmeter, it was necessary to carry out the corresponding calculations on the OpenFOAM software packages. After processing the results of computer simulation, it was proved that from the technological and economic points of view it makes sense to use the proposed modernized flow meter, since with relatively similar measurement accuracy to those used in the field, the proposed flow meter has several advantages from an economic point of view.

This thesis includes a manual selection of a submersible installation with subsequent analysis and a criterion map within the framework of the project on import substitution and production localization. After selection and analysis, it was found that the domestic pump is not only inferior to its foreign counterpart but also has many technical advantages, for example, efficient energy consumption, which leads to significant cost savings, in addition to the above, lower capital investments are needed to use such an aggregate.

References

1. Unified system of information on the situation in the oceans: [website]. URL: http://rus.ferhri.ru/okhotsk/Meteo/Meteo_Wind_Strong.htm
2. Geography of Russia: information system: [website]. URL: <https://geographyofrussia.com/morya-rossii-oxotskoe-more/>
3. Unified system of information on the situation in the oceans // Forecast of meteorological conditions for the Sea of Okhotsk: [website]. URL: <http://hmc.meteorf.ru/sea/ohotsk/gfs/menu.php>
4. Truskov, P. Metocean, Ice and Seismic Conditions Offshore Northeastern Sakhalin Island. 1999, DOI: 10.4043/10816-MS.
5. Climate Data Archive: [site]. URL: <http://climatebase.ru/station/32053/>
6. Poplavskaya L.N., Oskorbin L.S. Seismic activity of the earth's crust of the shelf zones of the Sea of Okhotsk // Seismic zoning of the Kuril Islands, Amur Region and Primorye. Vladivostok, 1977. 120 p.
7. Soloviev S. L., Solovieva O. N. Relations between the energy class and magnitude // Izv. USSR Academy of Sciences. Physics of the Earth. 1967. No 2. 3-23 p.
8. Dubina, V.A., Plotnikov V.V. & Vakulskaya N.M. Spatial variability of ice drift on the northeastern shelf of Sakhalin Island // Izv. TINRO, 2015.272–235 p.
9. Friedman, B. (1997). The mineral ice. Retrieved from URL: <https://www.minerals.net/mineral/ice.aspx>
10. Derugin, K. & Stepanuk, I. Marine hydrometry. 1974, Moscow.
11. Jeffery, N. & Nunke, E. Validating Simulations of Sea Brine Dynamic with Field Observations. Los Alamos National Lab., 2014, LA-UR-14-26085.
12. ISO 19906:2019(E). Petroleum and natural gas industries — Arctic offshore structures. Second edition.
13. Politko, V.A. The impact of ice fields on single and multi-bearing hydraulic structures with a vertical supporting part. 2018, Moscow.
14. Fu Aohan, Stepanov A. B. Modern methods and means of measuring the flow of oil and oil products. Tomsk Polytechnic University, Tomsk.
15. Kremlin P.P. Flowmeters and counters of the amount of substances: Reference: Book. 1 / P.P. Kremlin. - 5th ed. reslave. and add. - SPb. : Polytechnic, 2015 .-- 409 p.
16. Ivshin V.P., Perukhin M.Yu. Modern automation in process control systems: a textbook. Infra-m. Moscow, 2014.402 p.

17. UFM. Ultrasonic Flowmeter Technology. Retrieved from URL: https://www.flowmeters.com/product-list.php?page=ultrasonic-technology/pg1-cid100.html=/asc_action=SetCurrCat/category_id=100
18. Koblov E.G. Zonal and local forecast of oil and gas potential of sedimentary basins of the Sea of Okhotsk / E. G. Koblov, V.V. Kharakhinov // Geology and development of oil and gas deposits of Sakhalin and the shelf. Moscow, 1997.26-56 p.
19. Confidential document of «Sakhalin Energy Investment Ltd. 1»
20. Shlyakhova, A., Jones, M. K., Kasumov, T. V., & Morgan, D. Piltun 'Sub-Arctic' Offshore Integrated Oil and Gas Development (Russian). Society of Petroleum Engineers. 2010, January 1. doi:10.2118/135948-RU
21. Evdokimov V.G., Bychkovskaya L.V. Addition to the technical project for the construction and operation of underground structures not related to mining, in order to place drilling waste and other liquids in the Astokhsky section of the Piltun-Astokhskoye oil and gas condensate field. Volume I. Moscow, 2017.267 s.
22. Statistics of the company Rystad energy in 2019: data on the Piltun-Astokhskoye field. URL:<https://www.rystadenergy.com/products/EnP-Solutions/ucube/>
23. Statistics of «Sakhalin Energy Investment Ltd.» in 2018: data on the PA-A field. URL:<http://www.sakhalinenergy.ru/ru/media/library/>
24. Davies, M. H., Readshaw, J. S., Sullivan, M. A., & Wells, H. C. Model Testing in Support of Molikpaq Deployment at Sakhalin Island. Offshore Technology Conference. 1999, doi:10.4043/10817-ms
25. Frederking R., Sudom D. Maximum ice force on the Molikpaq during the April 12, 1986 event. Elsevier. Volume 46, issue 3, December 2006. Pages 147-166.
26. Cengel, Y., Cimbala, J. Fluid Mechanics: Fundamentals and Applications. (4th ed.) 2017, Singapore: Mc Graw Hill Education.
27. Miller R., Kneisel O. A comparison between orifice and flow nozzle laboratory data and published coefficients. // Journal of Fluids Engineering, Transactions of the American Society of Mechanical Engineers, 96, 1974, pages 139-149.
28. Sahin B., Ceyhan H. Numerical and experimental analysis of laminar flow through square-edged Orifice with variable thickness. Transactions of the Institute of Measurement and Control, 1996, Vol 18(4), 166-174.
29. Ivanovsky V.N., Darishchev V.I. & Sabirov A.A. Well pumping units for oil production. et al. — M .: State Publishing House "Oil and Gas" of the Russian State University of Oil and Gas named after I.M., Gubkina, 2002. 824 p.

30. Confidential document of the company RusVietPetro, 2017.
31. Vasiliev V.V. Analysis of methods for intensifying oil inflow in the shelf conditions at the PiltunAstokhskoye field (Sakhalin Region), WRC, Tomsk, 2019.
32. Catalog of equipment of the production company "Borets", 2012.
33. Croasdale, K. R., Cammaert, A. B. An Improved Method for the Calculation of Ice Loads on Sloping Structures in First Year Ice. Proceedings of the International Russian Arctic Offshore (RAO). 1993, Conference, St. Petersburg, Russia, pp. 161-168.
34. Loads and impacts on hydraulic structures [Electronic resource]: ice impact on a conical structure, SP 38.13330.2012. [URL]: <http://docs.cntd.ru/document/1200095522>
35. Kotlyar E. A. Application of new technological solutions to improve the efficiency of the Piltun-Astokhskaya-B platform, dis., Moscow, 2018.
36. Johnny B. Comparison of Selected Differential Producing, Ultrasonic, and Magnetic Flow Meters, Master theses. Utah State University, 2014.

Appendix 1

ControlDict

```
/*-----*- C++ -*-----*\
|=====|
|\ \ / F i e l d | OpenFOAM: The Open Source CFD Toolbox |
| \ \ / O p e r a t i o n | Version: 3.0.1 |
| \ \ / A n d | Web: www.OpenFOAM.org |
| \ \ / M a n i p u l a t i o n |
\*-----*/
```

FoamFile

```
{
    version 2.0;
    format ascii;
    class dictionary;
    location "system";
    object controlDict;
}
// ***** //
```

```
libs (
    "libOpenFOAM.so"
    "libsimpleSwakFunctionObjects.so"
    "libswakFunctionObjects.so"
    "libgroovyBC.so"
);
```

```
application pimpleFoam;
startFrom latestTime;
startTime 0;
```

```

stopAt      endTime;
endTime     20;
deltaT      0.001;
writeControl adjustableRunTime;
writeInterval 0.01;
purgeWrite  20;
writeFormat  ascii;
writePrecision 6;
writeCompression off;
timeFormat   general;
timePrecision 6;
runTimeModifiable no;
adjustTimeStep yes;
maxCo        0.8;
maxDeltaT    1;
functions
{
  residuals
  {
    type      residuals;
    functionObjectLibs ("libutilityFunctionObjects.so");
    enabled    true;
    writeControl timeStep;
    writeInterval 1;

    fields
    (
      p
      U
      //k

```

```

        //omega
    );
}
forceCoeffs1
{
    type    forceCoeffs;
    functionObjectLibs ( "libforces.so" );
    outputControl timeStep;
    outputInterval 1;

    patches ( "pipe" );
    pName    p;
    UName    U;
    rhoName  rhoInf; // Indicates incompressible
    log      true;
    rhoInf   1;      // Redundant for incompressible
    liftDir  (0 0 1);
    dragDir  (1 0 0);
    CofR     (1 0 0); // Axle midpoint on ground
    pitchAxis (0 1 0);
    magUInf  1;
    lRef     1;
    Aref     3.14/4;
}
}
//
*****
***** //
Smooth.geo
Nc=20;

```

Nc1=40;
Nb=10;
D=1;
R=D/2;
Rc1=1.1;
Rc=1;
Rb=1;
a=R/4;
a1=a+0.125;
beta=2;
b=R/beta;
b1=b+0.125;
c=R;
e=R/2;
L1=5;
dd=D/4;
ddd=dd/2;
L2=L1+dd;
L3=5;
w= 0.1;
L3=L1+ddd;

Point(1) = {0, 0, 0, 1.0};
Point(2) = {a, 0, 0, 1.0};
Point(3) = {b, 0, 0, 1.0};
Point(4) = {0, a, 0, 1.0};
Point(5) = {0, b, 0, 1.0};
Point(6) = {-a, 0, 0, 1.0};
Point(7) = {-b, 0, 0, 1.0};
Point(8) = {0, -a, 0, 1.0};

Point(9) = {0, -b, 0, 1.0};

Point(19) = {e*0.3914213562, -e*0.3914213562, 0, 1.0};

Point(20) = {-e*0.3914213562, e*0.3914213562, 0, 1.0};

Point(21) = {e*0.3914213562, e*0.3914213562, 0, 1.0};

Point(22) = {-e*0.3914213562, -e*0.3914213562, 0, 1.0};

Point(23) = {0, c, 0, 1.0};

Point(24) = {0, -c, 0, 1.0};

Point(25) = {c, 0, 0, 1.0};

Point(26) = {-c, 0, 0, 1.0};

// centre

Circle(1) = {4, 22, 2};

Circle(2) = {2, 20, 8};

Circle(3) = {8, 21, 6};

Circle(4) = {6, 19, 4};

//big circle

Circle(5) = {24, 1, 26};

Circle(6) = {23, 1, 26};

Circle(7) = {25, 1, 23};

Circle(8) = {24, 1, 25};

//litle circle

Circle(13) = {7, 1, 5};

Circle(14) = {5, 1, 3};

Circle(15) = {3, 1, 9};

Circle(16) = {7, 1, 9};

```

//lines from centre to little circle
Line(17) = {6, 7};
Line(18) = {4, 5};
Line(19) = {2, 3};
Line(20) = {8, 9};
//lines from center to little circle
//lines from little circle to big circle
Line(21) = {7, 26};
Line(22) = {5, 23};
Line(23) = {3, 25};
Line(24) = {9, 24};

//Surfaces

//centre
Line Loop(1) = {3, 4, 1, 2};
//+
Plane Surface(1) = {1};
//centre lines
Transfinite Line {1,2,3,4} = Nc Using Progression Rc;
Transfinite Surface {1};
Recombine Surface {1};

//+
Line Loop(2) = {17, 13, -18, -4};
//+
Plane Surface(2) = {2};
//+
Line Loop(3) = {1, 19, -14, -18};
//+

```

```

Plane Surface(3) = {3};
//+
Line Loop(4) = {19, 15, -20, -2};
//+
Plane Surface(4) = {4};
//+
Line Loop(5) = {20, -16, -17, -3};
//+
Plane Surface(5) = {5};
//lines from centre to little circlePlane Surface(1) = {1};
//centre lines
Transfinite Line {1,2,3,4} = Nc Using Progression Rc;
Transfinite Surface {1};
Recombine Surface {1};

Transfinite Line {17,18,19,20} = Nc Using Progression Rc;
//lines of little circle
Transfinite Line {13,14,15,16} = Nc Using Progression Rc;
Transfinite Surface {2,3,4,5};
Recombine Surface {2,3,4,5};

//big circle

//+
Line Loop(6) = {21, -6, -22, -13};
//+
Plane Surface(6) = {6};
//+
Line Loop(7) = {23, 7, -22, 14};
//+

```

```

Plane Surface(7) = {7};
//+
Line Loop(8) = {24, 8, -23, 15};
//+
Plane Surface(8) = {8};
//+
Line Loop(9) = {5, -21, 16, 24};
//+
Plane Surface(9) = {9};
//lines from little circle to big
Transfinite Line {21,22,23,24} = Nc1; //Using Progression Rc1;
//lines of big circle
Transfinite Line {5,6,7,8} = Nc Using Progression Rc;
Transfinite Surface {6,7,8,9};
Recombine Surface {6,7,8,9};
//second surface
Point(31) = {0, 0, L2, 1.0};
Point(32) = {a, 0, L2, 1.0};
Point(33) = {b1, 0, L2, 1.0};
Point(34) = {0, a, L2, 1.0};
Point(35) = {0, b1, L2, 1.0};
Point(36) = {-a, 0, L2, 1.0};
Point(37) = {-b1, 0, L2, 1.0};
Point(38) = {0, -a, L2, 1.0};
Point(39) = {0, -b1, L2, 1.0};

Point(40) = {e*0.3914213562, -e*0.3914213562, L2, 1.0};
Point(41) = {-e*0.3914213562, e*0.3914213562, L2, 1.0};
Point(42) = {e*0.3914213562, e*0.3914213562, L2, 1.0};
Point(43) = {-e*0.3914213562, -e*0.3914213562, L2, 1.0};

```

```

Point(44) = {0, c, L2, 1.0};
Point(45) = {0, -c, L2, 1.0};
Point(46) = {c, 0, L2, 1.0};
Point(47) = {-c, 0, L2, 1.0};
//Center
Circle(25) = {36, 40, 34};
Circle(26) = {32, 43, 34};
Circle(27) = {38, 41, 32};
Circle(28) = {38, 42, 36};
//little circle
Circle(29) = {37, 31, 35};
Circle(30) = {33, 31, 35};
Circle(31) = {33, 31, 39};
Circle(32) = {37, 31, 39};
//big circle
Circle(33) = {47, 31, 44};
Circle(34) = {44, 31, 46};
Circle(35) = {46, 31, 45};
Circle(36) = {45, 31, 47};
//lines from center to little circle
Line(37) = {36, 37};
Line(38) = {34, 35};
Line(39) = {32, 33};
Line(40) = {38, 39};
//lines from little circle to big circle
Line(41) = {35, 44};
Line(42) = {37, 47};
Line(43) = {33, 46};
Line(44) = {39, 45};

```

```

//surfaces
//center
//+
Line Loop(10) = {27, 26, -25, -28};
//+
Plane Surface(10) = {10};
Transfinite Line {28, 25, -26, -27} = Nc Using Progression Rc;
Transfinite Surface {10};
Recombine Surface {10};
//little circle
//+
Line Loop(11) = {40, -31, -39, -27};
//+
Plane Surface(11) = {11};
//+
Line Loop(12) = {39, 30, -38, -26};
//+
Plane Surface(12) = {12};
//+
Line Loop(13) = {37, 29, -38, -25};
//+
Plane Surface(13) = {13};
//+
Line Loop(14) = {37, 32, -40, 28};
//+
Plane Surface(14) = {14};
//lines from centre to little circle
Transfinite Line {37,38,39,40} = Nc Using Progression Rc;
//lines of little circle

```

```

Transfinite Line {29,30,31,32} = Nc Using Progression Rc;
Transfinite Surface {11,12,13,14};
Recombine Surface {11,12,13,14};
//big circle
//+
Line Loop(15) = {44, -35, -43, 31};
//+
Plane Surface(15) = {15};
//+
Line Loop(16) = {43, -34, -41, -30};
//+
Plane Surface(16) = {16};
//+
Line Loop(17) = {42, 33, -41, -29};
//+
Plane Surface(17) = {17};
//+
Line Loop(18) = {42, -36, -44, -32};
//+
Plane Surface(18) = {18};
Transfinite Line {41,42,43,44} = Nc1; //Using Progression Rc1;
Transfinite Line {33,34,35,36} = Nc Using Progression Rc;
Transfinite Surface {15,16,17,18};
Recombine Surface {15,16,17,18};
n = 89; // number of intervals
r = 2-1.0501; // progression
a = (r - 1) / (r^n - 1);
one[0] = 1;
layer[0] = a;
For i In {1:n-1}

```

```

    one[i] = 1;
    layer[i] = layer[i-1] + a * r^i;
EndFor
newEntitise[] =
Extrude { 0,0,5}
{
Surface{ 1,2,3,4,5,6,7,8,9};
Layers{one[], layer[]};
Recombine;
};
newEntitise[] =
Extrude { 0,0,5.125}
{
Surface{ 1,2,3,4,5};
Layers{one[], layer[]};
Recombine;
};
//Np=40;
//Extrusion little circle
//Extrude {0, 0, L1} {Surface{ 1,2,3,4,5}; Layers{Np}; Recombine;}
//extrusion big circle
//Extrude {0, 0, L1} {Surface{6,7,8,9}; Layers{Np}; Recombine;}
n1 = 89; // number of intervals
r1 = 1.0501; // progression
a = (r1 - 1) / (r1^n1 - 1);
one[0] = 1;
layer[0] = a;
For i In { 1:n1-1}
    one[i] = 1;
    layer[i] = layer[i-1] + a * r1^i;

```

```

EndFor
newEntitise[] =
Extrude { 0,0,5}
{
Surface{10,11,12,13,14,15,16,17,18};
Layers{one[], layer[]};
Recombine;
};
Npp=80;
Extrude {0, 0, -ddd} {Surface{10}; Layers{Npp}; Recombine;}
Extrude {0, -ddd, -ddd} {Point{35}; Layers{Npp}; Recombine;}
Extrude {-ddd, 0, -ddd} {Point{33}; Layers{Npp}; Recombine;}
Extrude {ddd, 0, -ddd} {Point{37}; Layers{Npp}; Recombine;}
Extrude {0, ddd, -ddd} {Point{39}; Layers{Npp}; Recombine;}
SetFactory("OpenCASCADE");
//Extrude {., 0., -ddd} {Surface{11}; Layers{Npp}; Recombine;}
//Extrude {0., 0., -ddd} {Surface{10,11,12,13,14}; Layers{Npp}; Recombine;}
//Extrude {0., 0., -ddd} {Surface{10,11,12,13,14}; Layers{Npp};
Recombine;}//Extrude {0, 0, L3} {Surface{10,11,12,13,14}; Layers{Np};
Recombine;}
//extrusion big circle2
//Extrude {0, 0, L3} {Surface{15,16,17,18}; Layers{Np}; Recombine;}
//
//+
Physical Surface("inlet") = {7, 6, 9, 8, 3, 2, 5, 4, 1};
Physical Surface("outlet") = {396, 418, 440, 374, 286, 352, 330, 308, 264, 462};
Physical Surface("pipe") = {387, 409, 453, 431, 16, 17, 18, 15, 491, 508, 521, 474,
176, 198, 242, 220, 167, 189, 229, 211};
//Physical Surface("outlet") = {477, 455, 521, 499, 433, 367, 389, 411, 345, 443};
//Physical Surface("pipe") = {490, 512, 446, 468, 17, 18, 15, 16, 323, 310, 293, 276,
242, 220, 198, 176, 229, 167, 189, 211};

```

```

Physical Volume("pipee") = {15, 24, 22, 23, 19, 18, 17, 16, 20, 21, 13, 14, 10, 12, 11,
9, 6, 2, 5, 1, 4, 3, 7, 8};

//Physical Volume("cone") = {559, 563, 567, 571, 308, 330, 352, 286, 572, 12, 14, 13,
11};Physical Volume("cone") = {573};//+

SetFactory("OpenCASCADE");

//startedges

Point(146) = {-0, 0, 5.125, 1.0};
Point(147) = {-0, -0.125, 5.125, 1.0};
Point(148) = {-0, 0.125, 5.125, 1.0};
Point(149) = {-0.125, 0, 5.125, 1.0};
Point(150) = {0.125, -0, 5.125, 1.0};
Point(101) = {e*0.3914213562, -e*0.3914213562, L3, 1.0};
Point(102) = {-e*0.3914213562, e*0.3914213562, L3, 1.0};
Point(103) = {e*0.3914213562, e*0.3914213562, L3, 1.0};
Point(104) = {-e*0.3914213562, -e*0.3914213562, L3, 1.0};
Point(105) = {b, 0, L3, 1.0};
Point(106) = {0, b, L3, 1.0};
Point(107) = {-b, 0, L3, 1.0};
Point(108) = {0, -b, L3, 1.0};

//center1

//Circle(500) = {149, 101, 148};
//Circle(501) = {150, 104, 148};
//Circle(502) = {147, 102, 150};
//Circle(503) = {147, 103, 149};

//midle circleORIFICE

//Circle(601) = {107, 146, 106};
//Circle(602) = {106, 146, 105};
//Circle(603) = {105, 146, 108};
//Circle(604) = {108, 146, 107};

```

```
//Line(701) = {71,106};
//+
SetFactory("OpenCASCADE");
//+
SetFactory("OpenCASCADE");
//+
SetFactory("OpenCASCADE");
//+
SetFactory("OpenCASCADE");
//+
//Cone(25) = {0, 0, 5.125, 0, 0, 0.125, 0.25, 0.375, 2*Pi};
//+
//Cone(26) = {0, 0, 5.125, 0, 0, 0.125, 0.25, 0.375, 2*Pi};
//+
SetFactory("OpenCASCADE");
//+
SetFactory("OpenCASCADE");
//+
SetFactory("OpenCASCADE");
//+
SetFactory("OpenCASCADE");
//+
SetFactory("OpenCASCADE");
//+
SetFactory("OpenCASCADE");
//+
SetFactory("Built-in");
//+
SetFactory("Built-in");
//+
```

```
Curve Loop(19) = {267, -290, 311, 333};  
//+  
Curve Loop(20) = {29, -30, 31, -32};  
//+  
Plane Surface(572) = {19, 20};  
//+  
SetFactory("OpenCASCADE");  
Cone(25) = {0, -0, 5.125, 0, 0, 0.125, 0.25, 0.375, 2*Pi};
```